

Department of Physics and Astronomy  
University of Heidelberg

Master Thesis in Physics  
submitted by

**Severin Morris Meister**

born in Stuttgart (Germany)

**2016**



# XUV Free-Electron Laser Experiments on Weakly Bound Dimers: Construction of a Water-Dimer Jet Source and Resonance-Enhanced ICD in Ne<sub>2</sub>

This Master Thesis has been carried out by Severin Morris Meister at the  
Max-Planck-Institute for Nuclear Physics in Heidelberg  
under the supervision of  
Priv.-Doz. Dr. Robert Moshhammer  
and  
Dr. Kirsten Schnorr



---

**Abstract:** The thesis at hand is dealing with two different experiments on dimers, water  $(\text{H}_2\text{O})_2$  and Neon dimers  $\text{Ne}_2$  specifically. The first part focuses on the design and construction of an in-vacuum water cluster source, which operates on the principle of supersonic gas expansion. A subsequent commissioning was done to characterize and optimize the performance of the source with respect to the demanded parameters, especially the water dimer yield. Upcoming experiments on proton transfer dynamics in water dimers will employ the developed cluster source.

In the second part, an experiment on the resonance-enhanced Interatomic Coulombic Decay (ICD) is presented. It was carried out at the Free-Electron Laser in Hamburg (FLASH), providing high intensities and photon energies in the extreme ultraviolet regime (XUV). By employing the wavelength tunability of FLASH2, we observed an enhancement of ICD, by scanning the  $\text{Ne}^+(2p)^{-1} \rightarrow \text{Ne}^+(2s)^{-1}$  resonance at 26.9 eV (46.1 nm). The resulting  $\text{Ne}^+ + \text{Ne}^+$  fragments were measured with a Reaction Microscope in coincidence.

**Zusammenfassung:** In dieser Arbeit werden zwei Experimente mit Bezug auf Wasser-  $(\text{H}_2\text{O})_2$  bzw. Neondimere ( $\text{Ne}_2$ ) vorgestellt. Der erste Teil konzentriert sich auf die Planung und Konstruktion einer in Vakuum Wasserclusterquelle. Diese erlaubt eine effiziente Erzeugung von Gasjets, basierend auf dem Prinzip der Überschallexpansion. Bei der folgenden Inbetriebnahme wurde die Düse charakterisiert und auf die Wasserdimerausbeute optimiert. Die Clusterquelle wird bei Experimenten zur Protonentransferdynamik und Abregungsmechanismen in Wasserdimeren zum Einsatz kommen.

Im zweiten Teil der Arbeit wird die resonante Erhöhung des Interatomic Coulombic Decay (ICD) in  $\text{Ne}_2$  experimentell nachgewiesen. Das Experiment wurde am Freielektronen-Laser in Hamburg (FLASH) durchgeführt. Dieser stellt hohe Photonenintensitäten und Photonenenergien im extrem ultravioletten Bereich (XUV) zur Verfügung. Unter Ausnutzung der durchstimmbaren Photonenwellenlänge von FLASH2, wurde eine Erhöhung des ICD im Bereich der  $\text{Ne}^+(2p)^{-1} \rightarrow \text{Ne}^+(2s)^{-1}$  Resonanz gefunden. Als Signatur des ICD Prozesses wurden die  $\text{Ne}^+ + \text{Ne}^+$  Fragmente mit einem Reaktionsmikroskop in Koinzidenz gemessen.



# Contents

<b>1</b>	<b>Introduction</b>	<b>10</b>
<b>2</b>	<b>Cluster Formation</b>	<b>13</b>
2.1	Supersonic Expansion . . . . .	17
2.1.1	Scaling Law . . . . .	18
2.1.2	Carrier and Seeding Gases . . . . .	21
2.2	Neon Dimer . . . . .	21
<b>3</b>	<b>Construction and Characterization of a Water Cluster Source</b>	<b>23</b>
3.1	Setup of the Waterjet . . . . .	23
3.2	Heating and Long-Term Test . . . . .	26
3.3	Time of Flight (TOF) Spectra . . . . .	32
3.3.1	Pure Water . . . . .	32
3.3.2	Neon Seeding . . . . .	35
3.3.3	Helium Seeding . . . . .	38
3.3.4	Argon Seeding . . . . .	39
3.3.5	Xenon Seeding . . . . .	41
3.4	Seeding Results Overview . . . . .	43
<b>4</b>	<b>Photon-Atom Interaction</b>	<b>44</b>
4.1	First-Order Dipole Transitions . . . . .	45
4.2	Two- and Multi-Photon Excitation . . . . .	48
<b>5</b>	<b>Interatomic Coulombic Decay (ICD)</b>	<b>50</b>
5.1	ICD in General . . . . .	50
5.2	Resonance-Enhanced ICD . . . . .	52
<b>6</b>	<b>Experimental Setup for the Neon Measurement</b>	<b>55</b>
6.1	Overview: Heidelberg Reaction Microscope at FLASH2 . . . . .	55
6.2	Free-Electron Laser - FLASH . . . . .	56
6.3	Reaction Microscope . . . . .	58

<b>7</b>	<b>Data Analysis - Resonance-Enhanced ICD</b>	<b>63</b>
7.1	Isolate Coulomb Explosions . . . . .	65
7.2	Kinetic Energy Release . . . . .	68
7.3	Scanning the Resonance . . . . .	70
7.4	Intensity Dependence . . . . .	71
7.4.1	Intensity Calibration . . . . .	71
7.4.2	Intensity Dependence of ICD . . . . .	73
<b>8</b>	<b>Summary</b>	<b>75</b>
8.1	Results of the Water Cluster Jet . . . . .	75
8.2	Results of the Neon Experiment . . . . .	76
8.3	Outlook . . . . .	77
<b>A</b>	<b>Appendix</b>	<b>78</b>
A.1	Supplement Characteristic Values for Scaling Laws . . . . .	78
A.2	TOF Spectra . . . . .	79
A.3	MCP Gain-Curve . . . . .	80
A.4	Mirror Reflectivity . . . . .	81
A.5	Design Drawings of the Water Cluster Jet . . . . .	82
	<b>Bibliography</b>	<b>92</b>





# 1 Introduction

Atomic and molecular clusters play a crucial role to bridge the gap between small quantum systems and bulk matter. The first is using approaches starting from the single particle picture. Common workhorses to obtain larger structures are linear combinations of single particle properties, such as electron wave functions. On the other end of the scale, one makes use of collective many-electron phenomena. Cluster physics is in between these two domains and tries to describe the transition from quantum level to macroscopic scale. The huge potential in exploiting the nanoscale regime was pointed out by Richard Feynman, almost 60 years ago in his lecture “There’s plenty room at the bottom” [1]. As foreseen by the outstanding physicist, research on nanoscale objects is still up-to-date and requires further investigation. Although the topic of cluster physics also comprises large compounds of atoms or molecules, the following considerations restrain to dimers. These are the most simple representatives, which allow to investigate fundamental processes on an atomic scale. The focus will be put on the dynamics within these small structures.

There is a natural time scale of molecular motion, which is the femtosecond ( $10^{-15}$  s) Ref. [2]. The relaxation mechanism this thesis is dealing with, takes place on this femtosecond timescale. Weakly bound systems can decay via the so-called “*Interatomic*” or “*Intermolecular Coulombic Decay (ICD)*”. ICD was first predicted by L.S. Cederbaum *et al.* in 1997 Ref. [3]. It is a general mechanism based on the electron correlation of weakly bound, neighboring atoms or molecules and can, under certain circumstances, dominate Auger decay. This is chiefly attributed to the comparatively short timescale ( $\approx$  fs) on which ICD takes place. ICD was first experimentally confirmed in 2003 in large Neon clusters [4].

Since then, ICD could be identified in many different systems<sup>1</sup>. Besides the fundamental knowledge gained on electron dynamics, the general appearance of the mechanism can also lead to connections with other disciplines, such as biology and medicine. A paper on DNA strand breaks, induced by low energy electrons ( $\approx$  3 eV–20 eV) [7], could provide such a connection. ICD in water clusters serves as

---

<sup>1</sup>water [5], noble gas [4], noble gas/alkali metal [6]

a source of electrons in the mentioned energy range and could, if extended to biologically relevant systems, trigger capital damage in malign tissue. The presented resonance-enhanced ICD may lead to an experimental scheme to control ICD.

Even though water is one of the most investigated molecules, there is little knowledge about the dynamics of structural rearrangements. Again, these dynamics take place on the femtosecond time scale, which got accessible during the last years.

A well-established technique to investigate molecule dynamics, is the pump-probe scheme Ref. [2]. A first laser pulse (pump) initiates a dynamic process (vibration, dissociation, rearrangement etc.) in the molecule, while a second, time-delayed pulse “probes” the system at later times. The probe pulse often leads to a fragmentation of the system. By measuring the momenta of the fragments, the structure at times of probe pulse incidence can be deduced. For a fixed delay between pump and probe pulse a single final configuration is obtained. If however, different delays are scanned, one gains information on the dynamics of the considered process.

This thesis concentrates on the target production for an experiment on the dynamics of proton transfer through a hydrogen bond. In order to show the proton dynamics, we chose the water dimer  $(\text{H}_2\text{O})_2$ , as it is the smallest system in pure water clusters where this process takes place.

A first pump pulse ionizes one water molecule  $\text{H}_2\text{O}^+ - \text{H}_2\text{O}$  and triggers the proton transfer. An intermediate complex  $\text{HO} - \text{H}_3\text{O}^+$  is formed and subsequently ionized by the delayed probe pulse to obtain  $\text{HO}^+ - \text{H}_3\text{O}^+$  (see figure 1.1). The delay-dependent yield of  $\text{HO}^+$  and  $\text{H}_3\text{O}^+$  can be used to determine the proton transfer time.

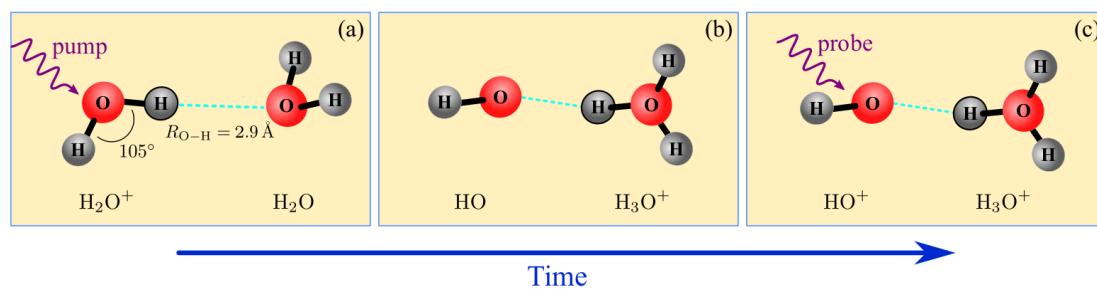


**Figure 1.1:** Pump-probe scheme of the proposed experiment: (a) the pump pulse ionizes one water molecule and triggers the proton transfer. (b) An intermediate complex  $\text{HO} - \text{H}_3\text{O}^+$  is formed and subsequently ionized (c) by the delayed probe pulse (figure from Ref. [8]).

The first part of this work is concentrating on the formation and production of water clusters and technical issues one encounters in building a cluster source. In the following commissioning, different carrier gases were used to optimize the water dimer yield.

The second part (section 4-7) will be about electron dynamics in weakly bound Neon dimers. After the theoretical part on light/atom interaction and the experimental setup, the acquired data is analyzed. Energy and intensity dependence of the resonance-enhanced ICD is considered in particular.

## 2 Cluster Formation

The term “Cluster” is generally used, if many entities act as a collective, or show properties which are different from the mere sum of its parts. In physics, one is referring to a limited amount of particles which are bound to each other. The concept of clusters found its way into several physical disciplines. There is particle physics [9], astrophysics [10] and cluster physics itself, which is dealing with compounds of atoms and/or molecules.

Clusters can be categorized to systematically relate properties. First, one can distinguish between pure clusters, i.e. composites of just one atom species, and mixed clusters. As the different atoms vary in size, the buildup can differ drastically from a homogeneous one. Moreover differences in the electronic structure can alter cluster properties e.g. heat capacity [11].

Another important characteristic is the number of entities which form the object. Size effects however, can change for different species, so there is no consistent labeling to group clusters according to their atomic count. To get a rough idea of the different regime, one can use the scales:

“micro”  $< 20$  parts, “small”  $< 100$  parts, and “large”  $> 100$  parts.

In addition, the type of bond between the constituents is a crucial characteristic for a cluster. The most important bonds are: metallic, ionic, covalent, Van-der-Waals and Hydrogen bond.

A prerequisite for stable clusters is that the binding energy is larger than the thermal energy  $k_B T$ . Therefore metallic and ionic clusters are more abundant in nature compared to e.g. Van-der-Waals bound ones (see table 2.1).

Bond type	ionic NaCl	covalent C (diamond)	metallic Lithium	Hydrogen bond in water	Van-der-Waals Neon
Binding energy [eV]	8.15	7.4	1.63	0.2	0.003

**Table 2.1:** *Exemplary binding energies. via [12, 13]*

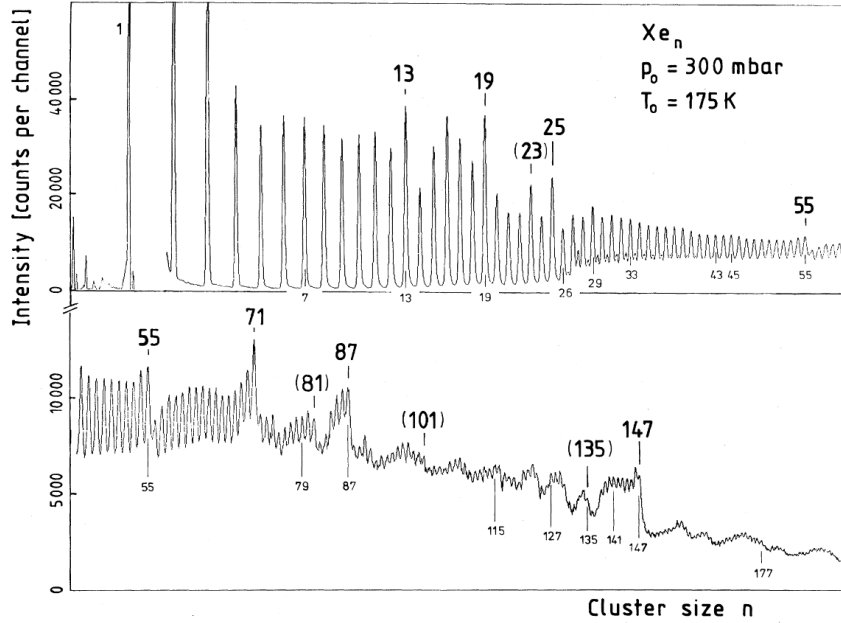


**Figure 2.1:** *Abundance spectrum of Xenon clusters. The drop after a certain count of constituents indicates a closed shell. Adding an additional atom to an empty shell is unfavorable. [15]*

For calculations in condensed matter physics, one usually assumes the material to be infinitely extended. This approximation allows to concentrate on bulk effects, rather than surface effects. However, this approximation is getting worse with decreasing size of the considered object, i.e. this has to be taken into account when dealing with clusters. In general, surface atoms are energetically less favored, because there are no binding partners at the edge of the object. During the statistical process of formation ([14], sec. 2.8), binding energy is minimized. In other words, the number of surface atoms is minimized. In first order, this is a geometrical issue and leads forcibly to spherically shaped objects where the ratio  $R$  of surface to bulk is minimal. This ratio is getting crucial for small objects. In macroscopic samples, surface atoms can be neglected, while for compounds of just a few atoms surface is dominating. If one assumes a sphere, the size dependent ratio  $R$  is given by:

$$R = \frac{A}{V} = \frac{4\pi r^2}{\frac{4}{3}\pi r^3} \propto \frac{1}{r}. \quad (2.1)$$

As the building blocks are rigid atoms, there are specific ways to arrange them.

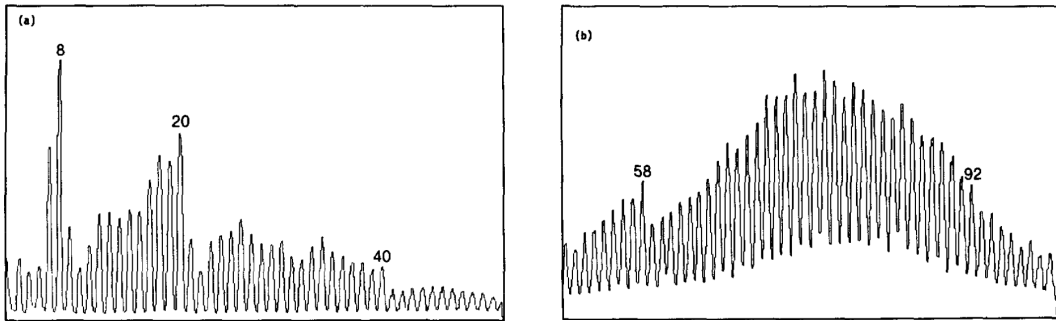


**Figure 2.2:** *Abundance spectrum of potassium clusters. The atomic counts for electronic shell closings are more abundant than for other cluster sizes [19]*

The icosahedral structure plays a prominent role for rare-gas clusters. In these clusters, electronic effects are suppressed and forces are non-directional [16]. The icosahedral shape causes tension between adjacent atoms and layers, because it has no long-range translational symmetry [17] as for example the fcc (“face centered cubic”) lattice. However, the gains in surface optimizations overcompensate the induced tensions for objects in the cluster regime. The smallest icosahedron comprises 13 atoms. One atom is found in the center, surrounded by the equally distributed remaining 12 atoms. (see figure 2.3)

Adding an additional atom to this structure is energetically unfavored. In analogy to electron shells in atoms, one uses the term “shell” for a certain count of atoms, which brings a notable stability with it. The next filled up shell is found for an atomic count of 55, followed by 147 and so on. This geometric packing was first depicted by Mackay, who also came up with a formula to calculate the total atomic count  $N$ , or “geometrical magic numbers”, within  $n$  icosahedral shells, [18]

$$N = \frac{10}{3}n^3 + 5n^2 + \frac{11}{3}n + 1. \quad (2.2)$$

The direct effect of this principle can be found in an abundance spectrum of rare gas clusters (figure 2.1). The more stable an object, the higher is its abundance. There is a drop in the spectrum after closing a shell, because the added atom is exposed and easily split off. The other peaks, which are not explained by equation 2.2, belong to atomic counts where subshells are filled.

Besides the geometrical effect of packing a cluster, there is also an electronic effect which comes into play. It is most pronounced for alkali metals, exhibiting a single valence s-electron. This electron can be considered as almost free, meaning it is assumed to be equally distributed over the entire cluster. In analogous manner

to the energy levels of an atom, the almost free electrons of the cluster, occupy certain energy states. The filling of shells obeys therefore the Pauli principle. If one assumes the most simple potential, a spherical square well, with principal quantum number  $n$  and angular momenta  $s, p, d, \dots$  the ordering of level is  $1s, 1p, 1d, 2s, 1f, 2p, 1g, 2d, 3s, 1h$  etc. This corresponds to shell closings at  $N = 2, 8, 18, 20, 34, 40, 58, 68, 70, 92, \dots$  [19, 20]

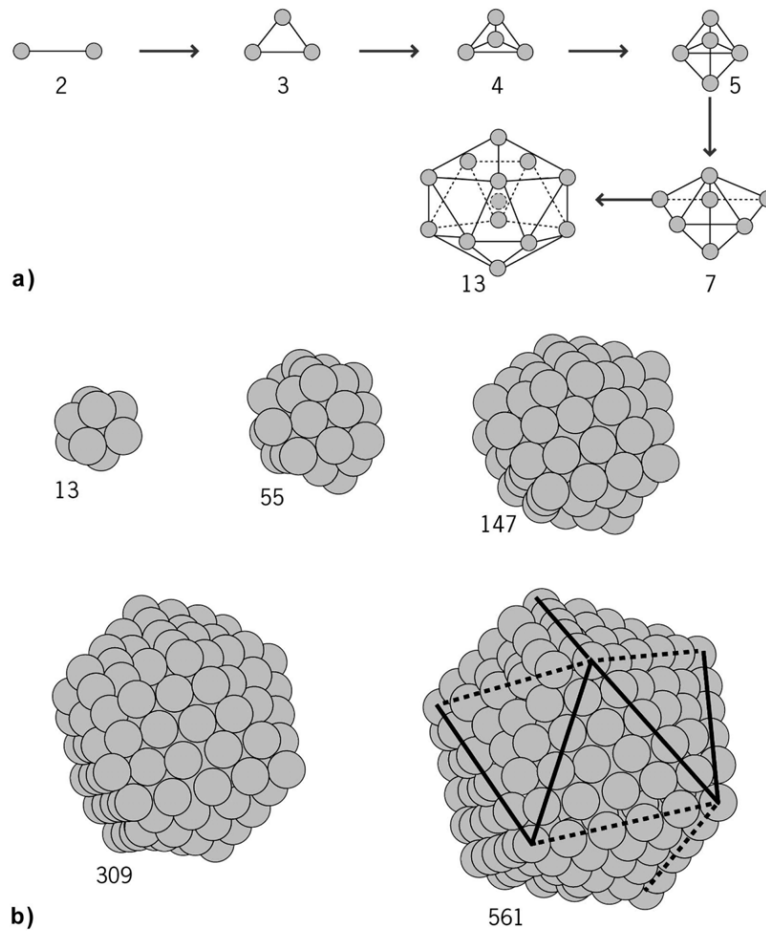


**Figure 2.3:** a) The stepwise buildup from a dimer to the icosahedral structure.  
 b) The first Mackay icosahedra, leading to the magic numbers. Taken from Ref. [17].



## 2.1 Supersonic Expansion

Noble gas clusters are bound via the Van-der-Waals force. The binding energies of about 20 meV  $\hat{=}$   $-40^\circ\text{C}$  are small compared to room temperature thermal energy. Therefore no noble gas clusters are formed at standard conditions<sup>1</sup>. Consequently one needs to cool down the target, in order to produce clusters.

In the presented experiments, supersonic gas expansion is used to achieve this cooling. The process sets in, if gas flows from a high pressure region, through a small nozzle, into a low pressure region. The process can be assumed to be isentropic, as friction and heat conduction can be neglected [22]. The entropy of the gas is constant and with it the density of states. The spatial density however, decreases during the expansion into the low pressure region and consequently the density in momentum space has to increase. This increase is equivalent to a decrease in temperature. The thermal energy is converted into directed kinetic energy along the expanding direction. The particles gain supersonic velocity and the emerging beam has low divergence.

The supersonic expansion starts at a certain threshold, if the ratio of stagnation pressure  $p_0$  and expansion chamber pressure  $p_a$  is large enough ([22] p.85):

$$\frac{p_0}{p_a} \geq \left( \frac{\kappa + 1}{2} \right)^{\frac{\kappa}{\kappa-1}} \quad (2.3)$$

Where  $\kappa$  is the ratio of the specific heats  $\kappa = \frac{C_p}{C_V}$  of the used gas. The indices  $p$  and  $V$  stand for constant pressure and constant volume respectively.

The following explanation of the supersonic expansion process is analog to ([22] p.105f), where even more details are given.

If the condition of large pressure ratios (eq.2.3) is fulfilled, the pressure at the nozzle exit becomes independent of the backing pressure and is given by

$$p_{\text{backing}} = p_0 \left( \frac{1}{2}(\kappa + 1) \right)^{\frac{\kappa}{\kappa-1}}. \quad (2.4)$$

As the pressure at the nozzle exit is higher than the ambient pressure, the gas is said to be “underexpanded”. As a result, the gas expands even further. Because the flow is supersonic, it can’t “sense” the downstream boundary conditions and overexpands to pressures lower than  $p_a$ . This region is called zone of silence, as velocities are the largest and interactions reduced. The jet gets compressed by shock waves at the jet boundary, which is called barrel shock. These shock waves decrease the cross sectional area of the expansion and the flow cone closes up. At

<sup>1</sup>Standard temperature and pressure (STP) [21]:  $T = 273.15\text{ K}$ ,  $p = 10^5\text{ Pa}$

the point where all reflected compression shock waves intersect, the “Mach disk” is formed. It marks, like the barrel shock, a region of large temperature and density gradients.

At larger distances than the Mach disk, pressure and gas density decrease drastically, so the gas dynamic treatment is no longer valid. The molecular regime of the background is entered, where single particle properties are used to describe the gas behavior.

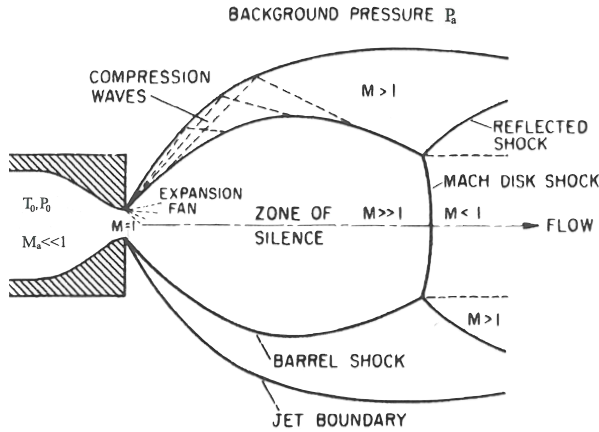


**Figure 2.4:** *Supersonic expansion* [23]

In order to create a cool gas jet with a narrow velocity distribution, one needs to extract the target molecules before the expansion zone breaks off. A so called “skimmer” is placed co-axial to the nozzle and extends into the zone of silence. In this manner, just the molecules with the desired properties find its way to the interaction region.

There is an experimental relation for the distance  $x_m$  of the Mach disk to the nozzle,

$$x_m = 0.67 d \sqrt{\frac{p_0}{p_a}}, \quad (2.5)$$

with  $d$  representing the nozzle diameter. It has been confirmed in a wide range of pressure ratios [24].

To get an idea of the process dimension, we use typical values of a measurement:  $d = 30 \mu\text{m}$ ,  $p_0 = 1000 \text{ mbar}$  and  $p_a = 3 \times 10^{-4} \text{ mbar}$ . In this constellation the Mach disk is located at:  $x_m = 3.7 \text{ cm}$ . In Ref. [24] Tejeda *et al.* give a rough estimation for the Mach disk diameter:  $D = 0.5 x_m$ .

### 2.1.1 Scaling Law

There is no rigorous theory to describe the process of clustering. Hagena *et al.* introduced though a semi-empirical approach and a scaling law [25]. This includes expansion conditions, simple kinetic considerations and many experimental

validations. The heart of the description is the dimensionless scaling parameter  $\Gamma$ . It contains both expansion related quantities denoted by the index 0 and gas associated characteristics, indexed by 'ch':

$$\Gamma^* = \frac{n_0 d^q T_0^\alpha}{r_{\text{ch}}^\alpha T_{\text{ch}}^\alpha} = \frac{p_0 d^q T_0^{\alpha-1}}{k_B r_{\text{ch}}^{q-3} T_{\text{ch}}^\alpha} \quad (0 < q \leq 1) \quad (2.6)$$

Where  $q$  is an empirically determined value and  $\alpha = \frac{1}{2} (q \frac{f-2}{2} - f)$  with  $f$  being the energetically active degrees of freedom. The variable  $d$  is the nozzle diameter. The characteristic temperature is denoted by  $T_{\text{ch}} = \epsilon/k_B$ , using the intermolecular well depth  $\epsilon$  <sup>2</sup> [22]. The characteristic size  $r_{\text{ch}}$  is determined via the atomic mass  $M$  and the density  $\rho$  of the solid:  $r_{\text{ch}} = \left(\frac{M}{\rho}\right)^{\frac{1}{3}}$ .

Employing the scaling parameter  $\Gamma^*$  from equation 2.6, Hagena also states an average clustersize  $\langle N \rangle$  by using another two free parameters  $D$  and  $a$ :

$$\langle N \rangle = D \left( \frac{\Gamma^*}{1000} \right)^a \quad (2.7)$$

The relations 2.6 and 2.7 were first introduced for rare gas clusters and later extended to metal vapors ([22] sec. 3.9.2). The value of  $\Gamma^*$  gives information on the degree of clustering. In general, one can assume, that for  $\Gamma^* < 200$  there is no clustering, while clusters of more than a hundred constituents are found beyond  $\Gamma^* > 1000$ . [25].

For our considerations, the work of C. Boppert *et al.* on size distributions of water clusters is very helpful. Based on the introduced scaling law, they extracted the free parameters  $q$ ,  $D$  and  $a$  by fitting experimental data. However, these relations are set up and validated for clusters with  $\langle N \rangle > 10$ , so our conclusions on smaller clusters, especially on dimers, should be handled with care.

For water, the following parameters were determined or looked-up from Boppert *et al.* [26]:

---

<sup>2</sup>If under standard conditions (STP) solid, one uses instead:  $T_{\text{ch}} = \Delta h_0/k_B$ , where  $\Delta h_0$  is the sublimation enthalpy at 0 K

Parameters of Water			
obtained from Fit		inherent Properties	
D	11.60	DOF f	6
q	0.634	$r_{\text{ch}}$	3.19 Å
a	1.886	$T_{\text{ch}}$	5684 K

**Table 2.2:**  $D$ ,  $q$ , and  $a$  are introduced to define the scaling parameter  $\Gamma^*$  in eq. 2.6 and the average cluster size  $\langle N \rangle$  in eq. 2.7. Characteristic values are defined subsequent to eq. 2.6. Taken from Ref. [26]

In our experiment, we are evaporating water and measure when the sample is thermalized. Therefore, the stagnation properties  $p_0$  and  $T_0$  are directly connected via the vapor pressure relation. The Antoine equation approximates this relation for certain temperature ranges [27]:

$$\log_{10} p_0 = A - \frac{B}{T_0 + C} \quad p[\text{bar}], T[\text{K}] \quad (2.8)$$

Temperature [K]	A	B	C
273–303	5.40221	1838.675	-31.737
304–333	5.20389	1733.926	-39.485
334–363	5.0768	1659.793	-45.854
344–373	5.08354	1663.125	-45.622
379–573	3.55959	643.748	-198.043

**Table 2.3:** Antoine Parameters listed in the NIST webbook [27] determined in [28, 29]

Inserting the parameters of table 2.2 and 2.3 in the merged equations 2.6, 2.7 and 2.8, we can solve for the temperature  $T_0$  at chosen nozzle diameters  $d$ , to obtain a mean cluster size  $\langle N \rangle$ :

$$\langle N \rangle (T_0) = D \left( \frac{10^{A - \frac{B}{T_0 + C}} d^q T_0^{q-4} 100}{k_B r_{\text{ch}}^{q-3} T_{\text{ch}}^{q-3}} \right)^a \quad (2.9)$$

The chosen dimensions are close to experimental conditions in section 3.2. If using a larger nozzle, one needs to decrease the temperature, in order to keep the same average cluster size. On the other hand, if one employs the same nozzle, but wants to increase the cluster size, one has to heat.

$\langle N \rangle$	$\phi$ Nozzle d [ $\mu\text{m}$ ]	Temperature [K]
2	30	86.7 °C
2	50	76.1 °C
5	50	92.3 °C

**Table 2.4:** *Example relations for the water cluster equation 2.9*

### 2.1.2 Carrier and Seeding Gases

Clustering can be enhanced by admixing carrier gases to the target gas, water vapor in our case. In this operation one speaks of a seeded source. Usually noble gases are co-expanded with the target molecules and carry off the heat of condensation. In fact, the noble gas atoms stabilize the growing clusters, by cooling them down. At absent or insufficient cooling rates, clusters cool themselves by evaporating constituents.

There is an optimal partial pressure  $p_c$  for the carrier gas. For low  $p_c$ , the collision rate between the noble gas and the clusters is insufficient for cooling. For large partial pressures  $p_c$ , collisions between target molecules decrease, so the cluster growth is hindered [14].

## 2.2 Neon Dimer

Under standard conditions, noble gases show no tendency for clustering or binding, as kinetic energies are relatively large. They have closed electron shells, which corresponds to an energetically favored state. Van-der-Waals forces induce dipoles which generate a weak attraction between the atoms. The binding energy of a Neon dimer is  $E = 3.6 \text{ meV}$  [13]. In terms of temperature this is about 42 K, thus stable Neon dimers must be at least of this temperature.

In nature, atoms of the same element can have different atomic masses, these are called isotopes. They have the same proton count, but a differing number of

neutrons. For Neon there are three stable isotopes with different abundances (see table 2.5). Due to the low occurrence of some isotope combinations, just two types of dimers are relevant for our experiment,  $Ne^{20} - Ne^{20}$  and  $Ne^{20} - Ne^{22}$ .

Isotope	Mass [u]	relative Abundance
$Ne^{20}$	19.992 435	90.48 %
$Ne^{21}$	20.993 843	0.27 %
$Ne^{22}$	21.991 383	9.25 %
$Ne^{20} - Ne^{20}$	39.98487	81.87 %
$Ne^{20} - Ne^{21}$	40.986278	0.49 %
$Ne^{20} - Ne^{22}$	41.983818	16.74 %
$Ne^{22} - Ne^{21}$	42.985226	0.04 %
$Ne^{22} - Ne^{22}$	43.982766	0.85 %
$Ne^{21} - Ne^{21}$	41.987686	0.0007 %

**Table 2.5:** *Natural Abundance of Neon [30]*

## 3 Construction and Characterization of a Water Cluster Source

### 3.1 Setup of the Waterjet

In future experiments at FLASH, clusters consisting of water molecules and noble gas atoms will be at the center of interest. Moreover proton dynamics in water dimers will be investigated. To provide these kinds of targets, a home-built jet source was designed and tested in the course of this master thesis.

Pure noble gas jets are widely used and come along without sophisticated engineering. They are already in gas phase under standard conditions and can be used with a gas bottle. The required backing pressure can be adjusted with a pressure regulating valve and the gas expands in the vacuum through a micrometer sized nozzle ( $\approx 5 \mu\text{m} - 50 \mu\text{m}$ ). However, for producing a water vapor jet, one is facing additional challenges.

Before the expansion through the nozzle, the water has to be brought into gas phase. A previous approach was a so-called “bubbler” outside the vacuum. Water is heated up in a sealed vessel until evaporation starts. The steam is then guided in a pipe to the nozzle, where the expansion takes place. There are several benefits: As there are no spatial limitations on the water reservoir, refilling is simple and there is no danger of spilling liquid water into the jet chamber. There is however freezing and condensation, which turns out to be problematic during operation. The steam carrying tube has to be heated to prevent condensation. For safe use, one even needs a temperature gradient between bubbler and nozzle. This condition is difficult to ensure in practice. Condensed water easily clogs the small pinhole and delays the entire experiment.

To overcome these adversities, a different approach to produce a water vapor jet is presented in the following. The water reservoir was miniaturized to a minimum and moved inside the vacuum chamber. In a nutshell, the process of heating and evaporation was brought as close as possible to the nozzle. The vapor has almost no distance to cover, minimizing the possibility of condensation and clogging.

The entire jet is made of stainless steel. On the one hand, this gives mechanical

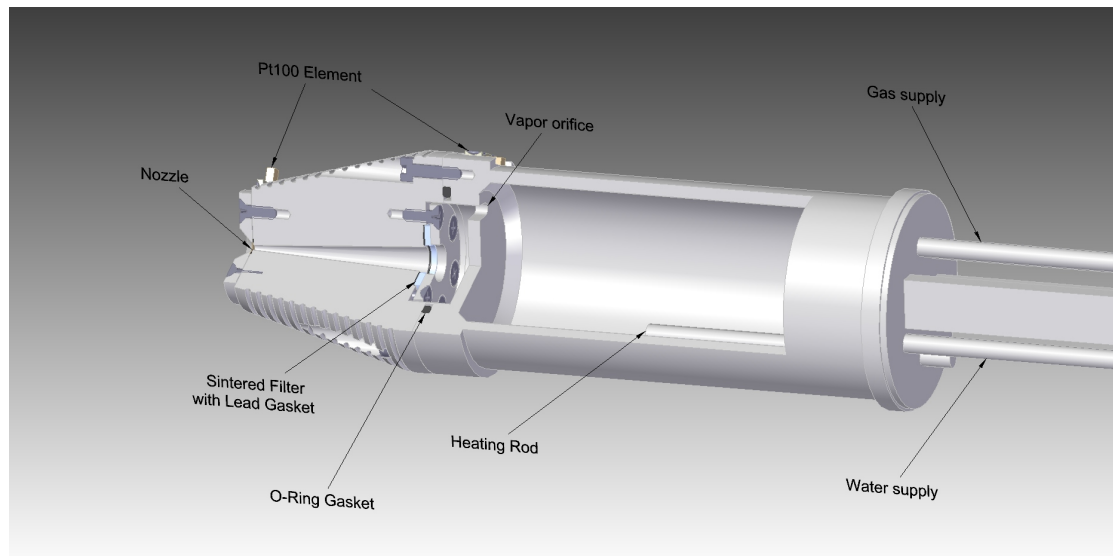


**Figure 3.1:** *Sketch of the water cluster source*

strength, needed for tiny screw threads and to withstand high pressures. On the other hand, stainless steel has a relatively small thermal conductivity. This is needed to keep a temperature gradient between reservoir and tip, again to prevent condensation. The two parts can be heated separately, such that the temperature profile can be regulated. The heatings are made of a special heating wire maintaining its properties up to several hundred degrees Celsius. The electric insulation around the wire is also temperature resistant up to 180 °C.

In order to speed up the heat-up phase, an additional heating rod is built into the reservoir. The heating rod is welded into the back lid of the reservoir, extending into the volume. (see figure 3.1)

The conical tip has a tapered hole, where the vapor is guided to the nozzle. The shape is chosen for several reasons. First the decreasing material thickness supports the temperature gradient. Secondly, if droplets form within the tip, they will slide away from the nozzle due to gravity. Additionally, the tip contains a sintered stainless steel filter at the beginning of the hole. With a chosen pore size of 5  $\mu\text{m}$  the filter stops even small particles from reaching and clogging the nozzle. The filter ring and the platinum nozzle are sealed up with a thin lead ring, instead of the frequently used Indium. Lead melts at 327.5 °C, which is far away from the applied temperatures and is soft enough to get squeezed by the pressure plate, to seal properly.

The entire tip can be detached to access the filter and its sealing. To keep the



system enclosed, an O-ring gasket is used between the reservoir and the tip.

Three Swagelok tubes at different heights are welded in the back lid of the reservoir. They are the only connections to the outside of the jet chamber, besides the wiring. Two of the 3 mm tubes are used for refilling the water reservoir, while the other is used for gas injection.

One of the refilling tubes is placed on the bottom of the reservoir and the other is just below the opening in the dividing wall. The idea is to pump in water at the lower orifice, while sucking on the upper one. If this upper orifice sucks in water, the reservoir is filled up to the maximum level. The filling process has to be repeated in given periods depending on the water volume in the beginning, the nozzle size and the applied temperature (see section 3.2). A continuous refilling scheme is impractical for experimenting, as steady conditions are needed.

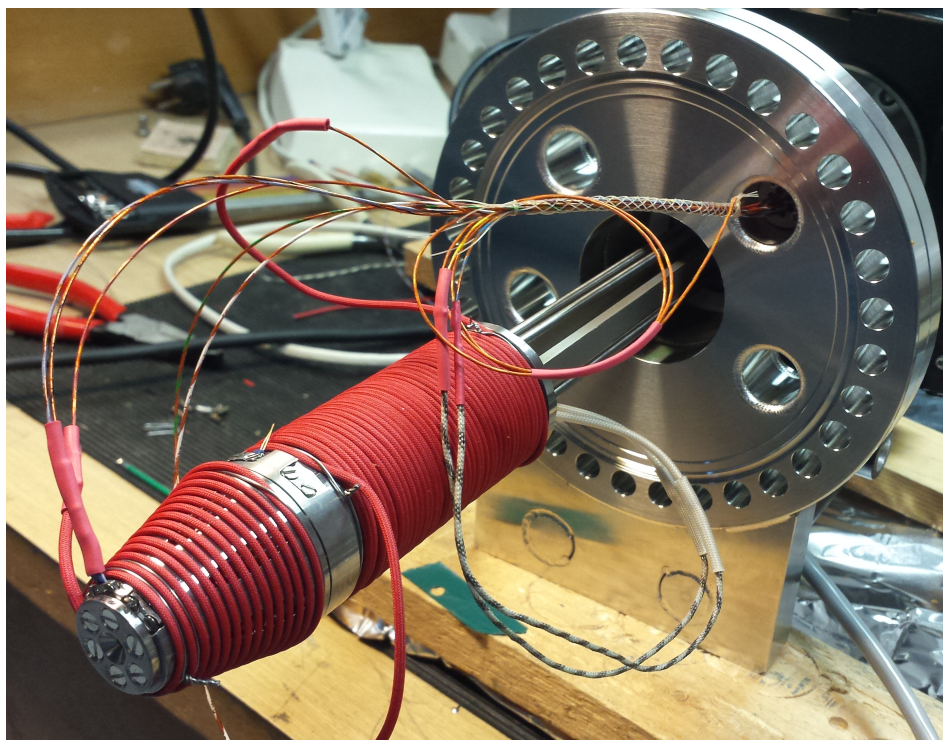


**Figure 3.2:** *Water jet mounted on XYZ-Manipulator: The red windings are the heating wires. The pressure plate marks the end of the tip, fixing the platinum nozzle. Two Pt100 elements are clamped onto the tip.*

The third tube is connected to a gas bottle. This allows to run the source in three different modes: A pure noble gas jet, a pure water vapor jet and a water vapor jet with admixed carrier gas. The latter mode permits to produce clusters consisting of noble gas atoms and water molecules.

The temperature measurement is done with Pt100 elements. This is a resistance thermometer, which employs the noble metal Platinum. In a given temperature range, its electric resistance  $R$  scales linearly with temperature  $T$ . The known  $T(R)$  dependence is used to deduce the temperature from the ohmic resistance. Two Pt100 elements are clamped at the very end of the tip, to monitor the crucial position of expansion. The supersonic expansion cools down the nozzle and freezing needs to be prevented. Another two elements are clamped at the outside of the reservoir, where the heating windings end. The second Pt-element at each position is a spare one.

The entire source is mounted on a XYZ-manipulator, which allows to align it with the skimmer in  $\mu\text{m}$  precision. In order to ensure the necessary rigidity, two steel beams are supporting the tubings. The wiring inside the jet chamber is connected to multiple-pin DN16 CF vacuum feed-throughs, mounted on the DN100 CF flange of the manipulator. Precisely chosen cable lengths enable to move the source without any restrictions, while sensitive regions like the skimmer are kept free.

## 3.2 Heating and Long-Term Test

The design of the presented water jet was started almost from scratch. There were only a few similar devices to gain some information on dimensioning and characterization (compare to [31]). One challenge was to estimate the flow rate and with that the time the reservoir lasts during an experiment. To get a rough idea, one can make use of the Hagen-Poiseuille-law. It is applicable for Newtonian fluids, like water vapor, to calculate the flow rate  $\dot{V}$  through a long pipe:

$$\dot{V} = \frac{\partial V}{\partial t} = \frac{\pi \Delta p \cdot r^4}{8 \eta \cdot l}, \quad (3.1)$$

where  $\eta$  is the dynamic viscosity,  $r$  the radius of the pinhole,  $l$  the length of the hole and  $\Delta p$  the pressure difference along the hole.

For our platinum nozzle, the diameter of the pinhole is comparable to the length of the hole, so the assumption of a long pipe is not given. As the law fails to a

large extend, we use the Bernoulli principle for an upper estimate of the flow rate:

$$\frac{\partial V_{\max}}{\partial t} = \pi r^2 \sqrt{2\Delta p/\rho}. \quad (3.2)$$

In a test run we used a  $r = 15 \mu\text{m}$  nozzle, which is about  $l = 0.1 \text{ mm}$  thick. The plateau temperature is  $T = 105^\circ\text{C}$  with a corresponding vapor pressure of  $p = 1200 \text{ hPa}$ . The pressure in the jet chamber was always  $< 10^{-3} \text{ hPa}$ , so in good approximation  $p = \Delta p$ . The dynamic viscosity of water vapor at this temperature is  $\eta = 12.26 \mu\text{Pa s}$ .

Furthermore, we can calculate the vapor density  $\rho_{120^\circ\text{C}}$  via the ideal gas law, using  $M_{\text{H}_2\text{O}} = 18.015 \text{ g/mol}$  and  $R = 8.314 \text{ J/(K mol)}$ , where  $V$  is the volume and  $m$  is the absolute mass:

$$pV = nRT, \quad (3.3)$$

$$pV = \frac{m}{M}RT, \quad (3.4)$$

$$\rho = \frac{m}{V} = \frac{pM}{RT}, \quad (3.5)$$

with the given values:  $\rho_{105^\circ\text{C}} = 0.688 \text{ kg/m}^3$ .

Inserting the result in equation 3.2 yields:

$$\dot{V}_{\max} \approx 0.417 \text{ ml/s} \quad (3.6)$$

To compare the calculated value with the measured, one needs to know the volume increase. From liquid water at  $20^\circ\text{C}$  to water vapor at  $105^\circ\text{C}$  it is:

$$\frac{\rho_{20^\circ\text{C},l}}{\rho_{105^\circ\text{C},g}} = \frac{998.2}{0.688} \approx 1451 \quad (3.7)$$

According to the calculation, a reservoir of  $20 \text{ ml}$  of water should last

$$t = \frac{20 \text{ ml}}{0.417 \text{ ml/s}} \cdot 1451 \approx 19 \text{ h} \quad (3.8)$$

In practice, the  $20 \text{ ml}$  last for  $38 \text{ h}$  (compare to the plateau region in figure 3.4). Here, the upper limit of the flow through the nozzle was estimated, so a result

which is off by factor two is not surprising. Nevertheless, this estimation helped for dimensioning in the designing phase.

Figure 3.3 shows a test run for different water fillings in the reservoir. The curve “Jet 1” refers to the pressure in the Jet chamber, where the first skimming takes place. Its trend gives the closest feedback on changes of the flow rate. In total, the gas jet is traversing another five jet stages. Their pressure trends mainly follow the dump pressure and will not be considered in the following.

The “dump” is in the very end of the vacuum setup, here the gas jet is dumped into a turbo molecular pump. If there is a decent pressure increase, one can assume that a supersonic expansion has taken place and a proper target jet has formed. Otherwise, the gas effuses out of the nozzle and is pumped away before the dump is reached.

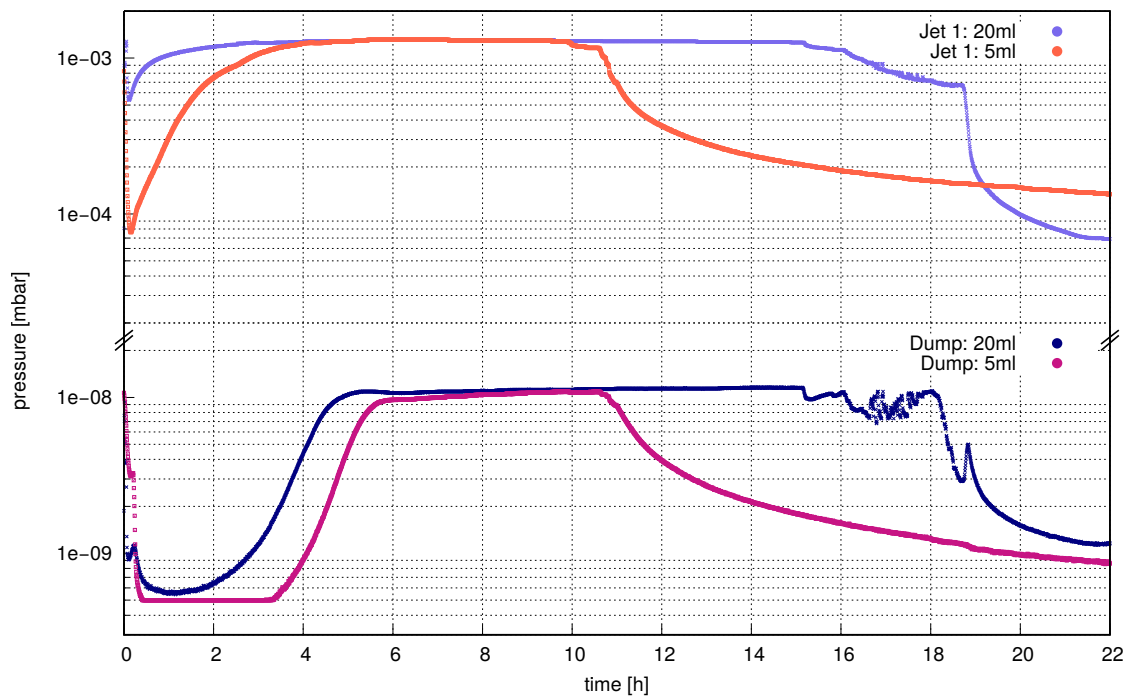


**Figure 3.3:** *Two runs with a 50  $\mu\text{m}$  nozzle, but different filling volumes. For the 20 ml run, a pre-heated source was used. As a result, the plateau was reached earlier, even though the larger water amount.*

In all cases, water at room temperature and under normal pressure was filled into the reservoir. Therefore, curves start from a relatively high level (e.g. figure 3.3). In the following pressures go down, as the water is not yet heated up, but the

pumps still work. If the thermalization of the water jet source is finished, a steady vapor flow rate sets in. This situation refers to a plateau region in pressure. The duration of this process is crucial for experimenting with the source, because one needs a stable target jet, by the time the FEL is turned on. Several parameters have an influence on this duration. If for instance, the steel reservoir and tip are already heated up before refilling, the plateau region is reached faster. This can be seen in figure 3.3, where the run with 20 ml was done with a pre-heated source and the 5 ml run started at room temperature. The dump plateau settles earlier, even though a larger water volume needs to be warmed up. In practice, a pre-heated source is difficult to handle though. The first ml of water entering the reservoir vaporize immediately. The prompt pressure increase pushes back the plugs of the syringes, which makes a controlled filling impossible.

The heatings were set to constant current mode throughout the entire experiment. Reservoir and tip of the source were kept on 0.4 A and 0.5 A, respectively. The different currents were used to maintain a temperature gradient from the back to the tip of the source, in order to prevent condensation. The heat-up period resembles a limited exponential growth with a single time constant. So it takes comparatively long to reach its limit. Changing the currents for the heat-up period and the steady state periods, can significantly shorten the time until the plateau region sets in. The runs in figures 3.3 and 3.4 are all done with the constant heat-up mode, where it takes 4 h–7 h. In figure 3.5, higher currents for tip 0.8 A and reservoir 0.6 A were chosen.

When a temperature of about 78 °C was reached, the steady state currents (0.4 A and 0.5 A) were set. In this scheme, the time to reach the plateau could be reduced to about 2 h. The conservative temperature to change the heating currents was deliberately chosen, because it was not known how strong the overshooting would be. It turned out however, to be no problem at all. Steady state temperatures could be closely approached, even with large currents, reducing the heat-up time further.

5 ml of water last for about 5 h, where the 20 ml in the second run only last for about 13 h (figure 3.4). This is surprising, because one assumes the runtime to scale linearly with water volume. Especially because the plateau pressures are the same, which indicates an equal flow rate.

Unfortunately, one has to assume that the reservoir was not totally empty for the 5 ml run. Measuring routines were just about to establish. The lower filling tube is not exactly on the bottom of the reservoir, so the filling level was wrongly tested. In the end of the plateau region, the reservoir runs out of water. Low fill levels

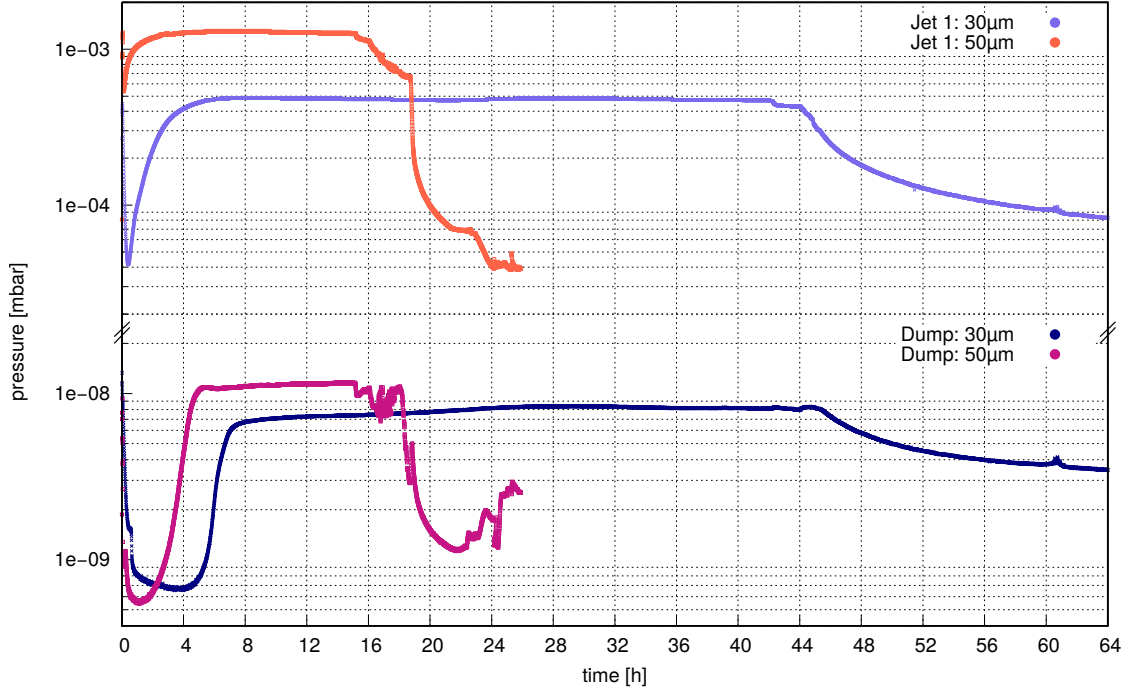


**Figure 3.4:** *Two runs, each with 20 ml water, but different nozzle diameters. For the 50  $\mu\text{m}$  measurement, a pre-heated source was used, so the plateau region settles faster. Currents: 0.4 A at the reservoir and 0.5 A at the tip, leading to ca. 120  $^{\circ}\text{C}$  in steady state.*

often involve a jitter in the pressure, before the reservoir is totally empty. An explanation for this effect might be the increasing surface to volume ratio of the water in the reservoir. The cooling during evaporation has a stronger impact for low filling levels, so pressure fluctuations might emerge more easily.

Figure 3.4 demonstrates the effect of different nozzle diameters on the flow rate. The higher throughput can be seen as larger pressures. There is a strong dependence on the nozzle orifice, as expected from equations 3.2 and 3.1. The 13 h plateau with a 50  $\mu\text{m}$  nozzle, is extended to about 38 h employing a 30  $\mu\text{m}$  nozzle. These values would suggest the following empirical nozzle radius dependence:

$$\frac{\partial V}{\partial t} \propto r^x \quad \rightarrow \quad \frac{\Delta t_2}{\Delta t_1} = \left( \frac{r_1}{r_2} \right)^x \quad (3.9)$$

$$x = \frac{\log(\Delta t_2/\Delta t_1)}{\log(r_1/r_2)} = \frac{\log(13 \text{ h}/38 \text{ h})}{\log(30 \mu\text{m}/50 \mu\text{m})} \approx 2.1 \quad (3.10)$$

However, this result should be handled with care, as just the plateau times were taken and the same evaporated volume was assumed. The curve for the 30  $\mu\text{m}$  nozzle flattens not as fast as in the 50  $\mu\text{m}$  case, so longer evaporation times should be assumed. This would lead to a stronger nozzle size dependence.

Figure 3.5 depicts a measurement with Argon as seeding gas. Seeding is a special feature of the presented jet source. One important parameter, is the water evaporation rate under additional pressure, by the Argon gas bottle. As described, increased heat currents were used during the heat-up period. Therefore the plateau region settled rather fast.

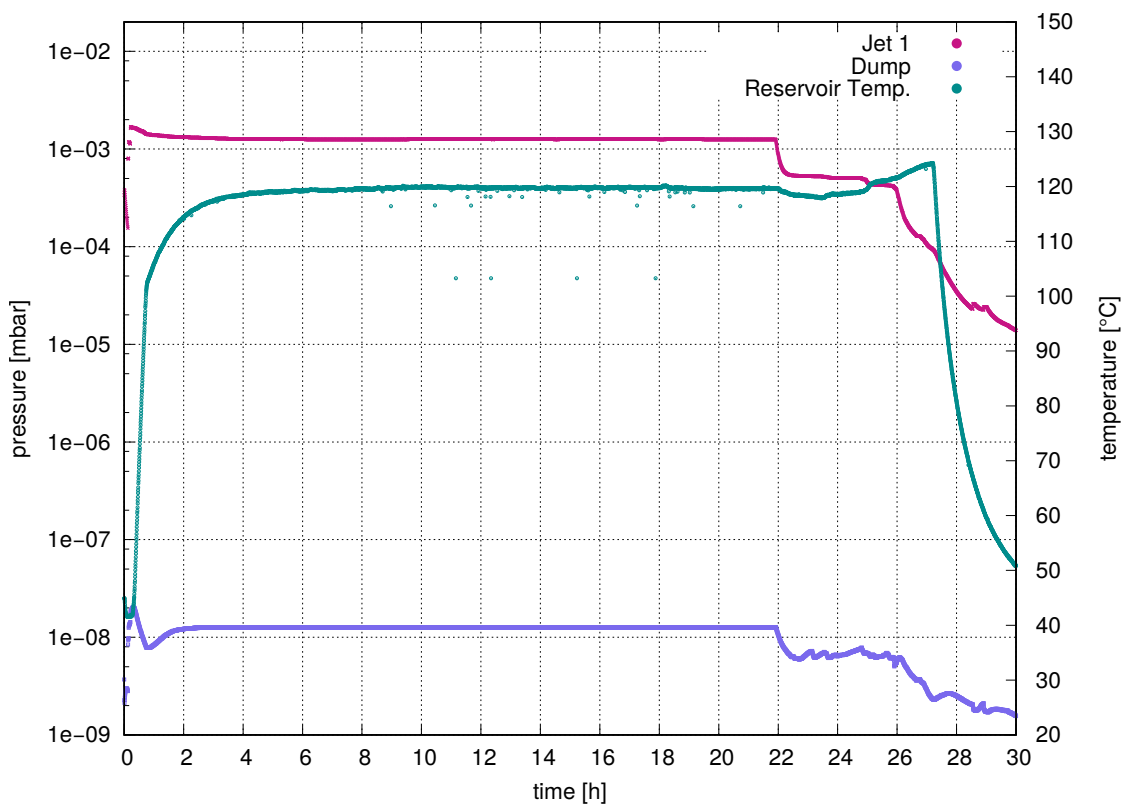


**Figure 3.5:** *Single run with 10 ml water and 3 bar Argon for seeding. Accelerated heat-up period with 0.6 A and 0.8 A for reservoir and tip, in steady state 0.4 A and 0.5 A. At 22 h the Argon supply was turned off and at 26.5 h heatings were switched off.*

The Argon supply was turned off at the 22 h mark, to find out the filling level in the reservoir. In the following, pressures dropped and settle for about 4 h on a different plateau. This suggest that there was still water left, creating the jet from

22 h–26 h. The subsequent pressure drop indicates an empty reservoir like in the previous runs. Afterwards, at about 26.5 h, the heatings were turned off.

Extrapolated from figure 3.4 with the 30  $\mu\text{m}$  nozzle, the 10 ml water should have lasted for 19 h. Without the 4 h of the ending plateau, one should have a 15 h plateau, if the Argon would have no effect. We find however a steady state region from 2 h–22 h. Therefore 3 bar Argon seeding gas on 105 °C hot water, extends the usable time by about a third.

## 3.3 Time of Flight (TOF) Spectra

### 3.3.1 Pure Water

Future experiments at FLASH will involve water dimers  $(\text{H}_2\text{O})_2$  and clusters composed of water and noble gases like Xenon and Neon. The presented jet source should provide these clusters with maximal yields. Therefore, besides the designing preconditions, one needs to know the optimal thermodynamic parameters (temperature, pressure, skimmer distance, nozzle diameter etc. [14]) to achieve best performance.

The following benchmark tests were done with an intense IR laser (800 nm,  $I \approx 10 \times 10^{14} \text{ W cm}^{-3}$ , rep. rate 3 kHz) and a REMI at MPIK. Due to the high intensity, the laser ionizes water by strong field ionization (Ref. [32]). In this way, ionization takes place, even if the photon energy (1.55 eV) is below the single ionization energy threshold of water 12.6 eV [33].

For the test runs in figure 3.6, a 30  $\mu\text{m}$  nozzle, at a distance  $L = 3.2 \text{ mm}$  to the skimmer, was used. Even though the runs have different statistics, one can clearly see the influence of temperature on clustering.

The most dominant peak at 23 880 ns is the water ion peak  $\text{H}_2\text{O}^+$ . Starting at this point, the other peaks can be assigned using equation 7.3. The spikes for small TOFs arise from  $\text{H}^+$  ions, which underwent different fragmentation pathways in strong-field ionization and therefore possess different energies. The exact mechanism will not be discussed at this point (see Ref. [32]).

The upper left spectrum in figure 3.6 has two sharp peaks at around 30 ps. They correspond to  $\text{N}_2^+$  and  $\text{O}_2^+$ , coming from air, which entered during the refilling of the water reservoir. These peaks vanish after some time, when the air is dissipated, like in the other spectra. As the  $\text{O}^{2+}$  and the  $\text{O}^+$  peak do not vanish



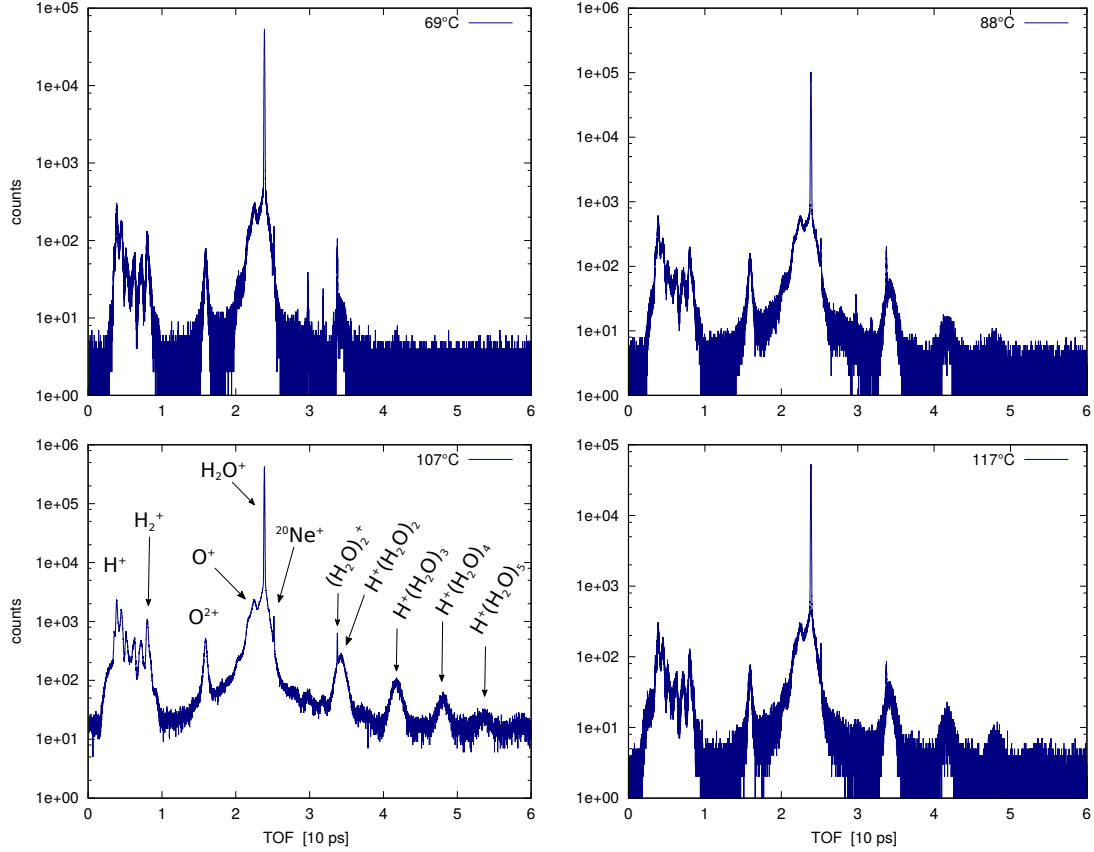


**Figure 3.6:** Time of flight spectra for a water jet at different reservoir temperatures. ( $d = 30 \mu\text{m}$ , distance skimmer to nozzle  $L = 3.2 \text{ mm}$ )

and appear pronounced, one can conclude them to stem from the target. Both ions were produced in a fragmentation process, therefore they exhibit large peak widths.

Besides the water monomer peak, there are two other sharp peaks at TOFs for  $^{20}Ne^+$  and  $(H_2O)_2^+$ , which thus also originate from the supersonic expansion. Neon is found due to previous noble gas test runs and is not considered in this section. Larger water oligomers  $(H_2O)_n^+$  are not observed as their binding is weaker than their protonated counterpart  $H^+(H_2O)_n$  [34]. These ionic clusters are called Zundel-like or Eigen-like, because their smallest structure is the Zundel ion  $H^+(H_2O)_2$  and the Eigen ion  $H_3O^+(H_2O)_3$ , respectively. The difference between these two formations is their structure. The first is proton centered and the latter centered around a Hydronium ion (Ref. [34]).

Water oligomers differ just in a single proton mass from the more stable Eigen-

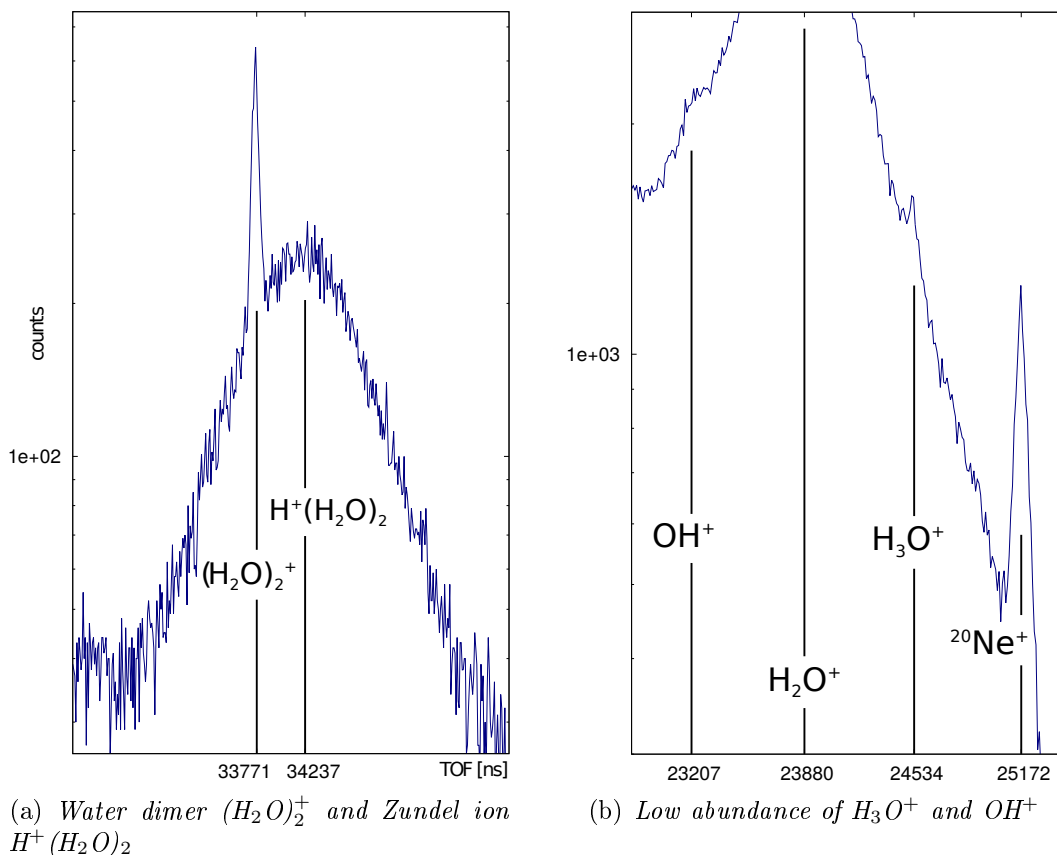
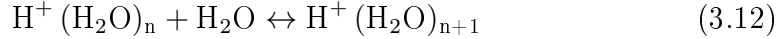
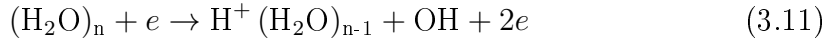


**Figure 3.7:** Detailed view on the water spectra. Marked positions are calculated by using the  $\text{H}_2\text{O}^+$  time of flight.

type ions and occur at similar time of flights (see figure 3.7(a)). If present, their weaker signal simply vanishes in the broad neighboring peak. Usually, we assume that an extended peak width is an indication of ions to stem from residual gas. In the case of the protonated water clusters however, the additional momentum comes from the protonation itself (eq. 3.11, [35]) and the following fragmentation (agglomeration) processes (eq. 3.12, [34]).

Equation 3.11 shows the impact of an electron colliding with a water cluster, becoming a metastable ion and following dissociation into stable products. In our case, this process is not triggered by an electron, but by absorbing infrared photons.



The extended width of the cluster peaks is also caused by evaporation of molecules from larger clusters. This effect was also observed by Hansen et al. in a electron spray ion source experiment on protonated water clusters [36]. The evaporation (reaction right to left in eq. 3.12) is driven by infrared photons [37]. At the lowest temperature of 69 °C in figure 3.6, one could barely see trimers and no larger clusters. With increasing temperature (and vapor pressure) however, cluster growth is enhanced. This is consistent with the temperature dependence derived in section 2.1.1, and shown in table 2.4.

Temp.	Dimer yield
69 °C	0.15 %
88 °C	0.19 %
107 °C	0.18 %
117 °C	0.17 %

The water dimer yield seems to be not directly connected to the growth of the protonated water clusters, as there is a maximal yield. In relation to the  $\text{H}_2\text{O}^+$  peak, we found a maximal dimer yield of 0.19 %, at 88 °C using an 30 µm nozzle (compare table 3.1). In an experiment on water dimers under similar condition by Jahnke et al., a “dimer fraction of less than 1 %” [5] was stated.

**Table 3.1:** *Integrated peaks:*  
 $(\text{H}_2\text{O})_2^+ / \text{H}_2\text{O}^+$

### 3.3.2 Neon Seeding

In section 2.1.2 the positive effect of seeding gases on clustering was introduced. In order to take the most advantage of this technique, we systematically investigated the influence of backing pressure, temperature and rare gas species. In section 3.4 the results of different combinations of these parameters are listed in a table. Trends and dependencies can easily be deduced.

We focused on maximizing the water dimer yield relative to the water monomer yield. Moreover, small mixed-clusters of rare gas atoms and water molecules were of special interest, as there is an experiment already scheduled.

### 3 Construction and Characterization of a Water Cluster Source

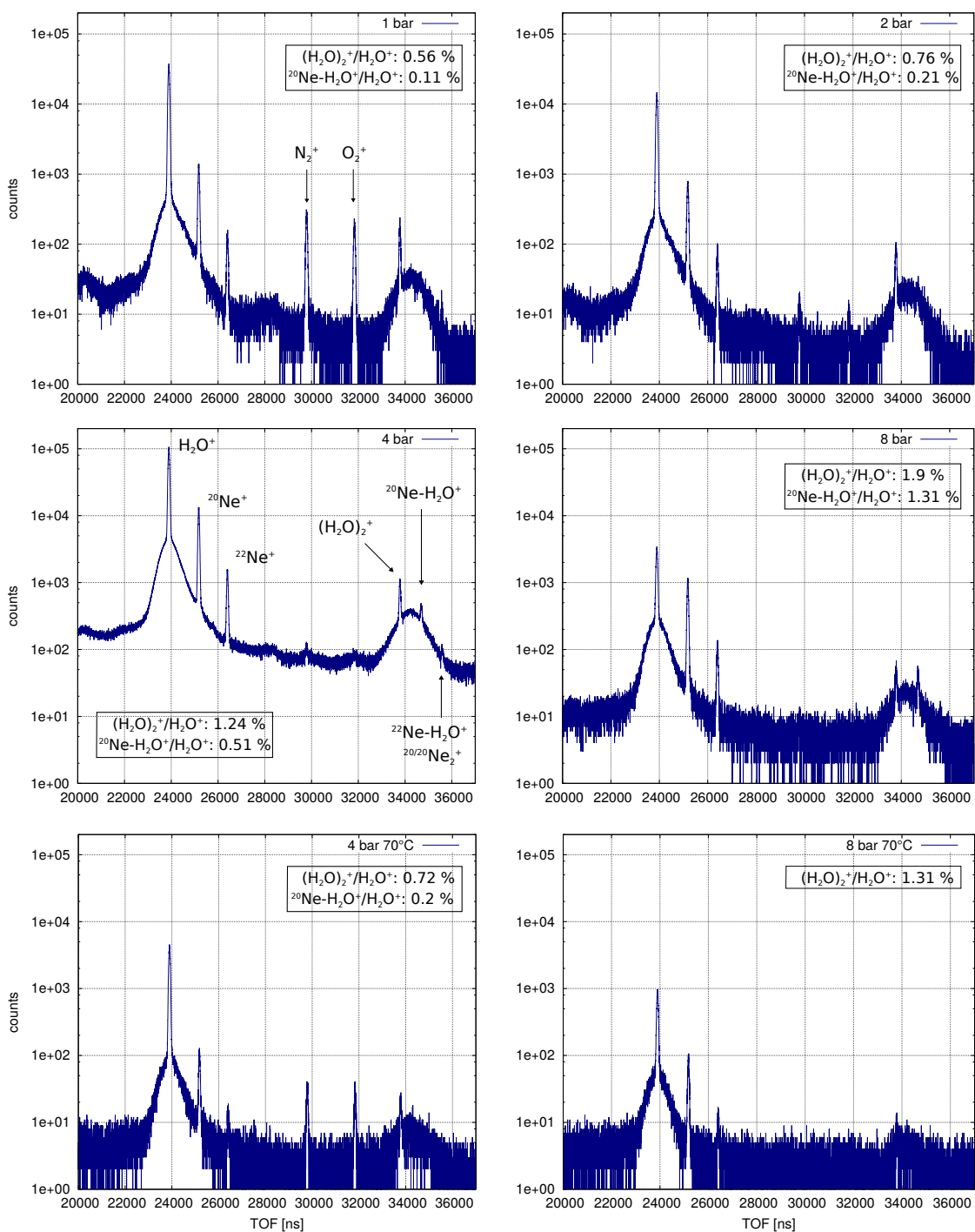


**Figure 3.8:** Water spectra without heating in the two upper rows and with heating in the last row. Neon seeding at different backing pressures.

Figure 3.8 shows four TOF spectra for different Neon backing pressures. In all cases no heating was applied. This would be not possible for water only, since the vapor pressure is not high enough for supersonic expansion to set in. In fact, the water source was not exactly at room temperature, but at 44 °C, which is owed to a nearby vacuum gauge. To prevent confusion, it should be said, that the two additional unlabeled peaks in the 1 bar spectrum, originate from air, which penetrated the system during refilling.

By simply comparing the orders of magnitude, one can infer the huge increase of the dimer yield, compared to section 3.3.1 with pure water. The yield increases even further with rising backing pressure. At 8 bar backing pressure we found a water dimer to monomer ratio of 1.9 %. This is an order of magnitude larger than the best result we obtained without seeding.

As indicated in the 4 bar spectrum, we also produced Neon-water clusters Ne-H<sub>2</sub>O in a fraction of 0.51 % of the water monomer. The peak just emerges for larger backing pressures (qualitatively in figure 3.8 and quantitatively in section 3.4) In addition to the pressure dependence, we also checked the influence of temperature. The water reservoir was heated up to 70 °C and spectra were taken for two different backing pressures (see figure bottom row in figure 3.8). One could see just by comparison of the spectra, that the fraction of water monomers, relative to the Neon monomers, is rising with increasing temperature. This is a reasonable observation, since the partial pressure of water vapor goes up with temperature. Another important finding is the temperature effect on the water dimer yield. The fraction of (H<sub>2</sub>O)<sub>2</sub> at 8 bar goes down by 30 % if the temperature is increased from 44 °C to 70 °C. For a backing pressure of 4 bar the water dimer yield even decreases by about 42 %.

The same trend with temperature is found for the Ne-H<sub>2</sub>O abundance.

The results suggest to use low temperatures and high backing pressures to maximize the water dimer yield. A spectrum over the entire TOF range can be found in the Appendix A.2.

### 3.3.3 Helium Seeding

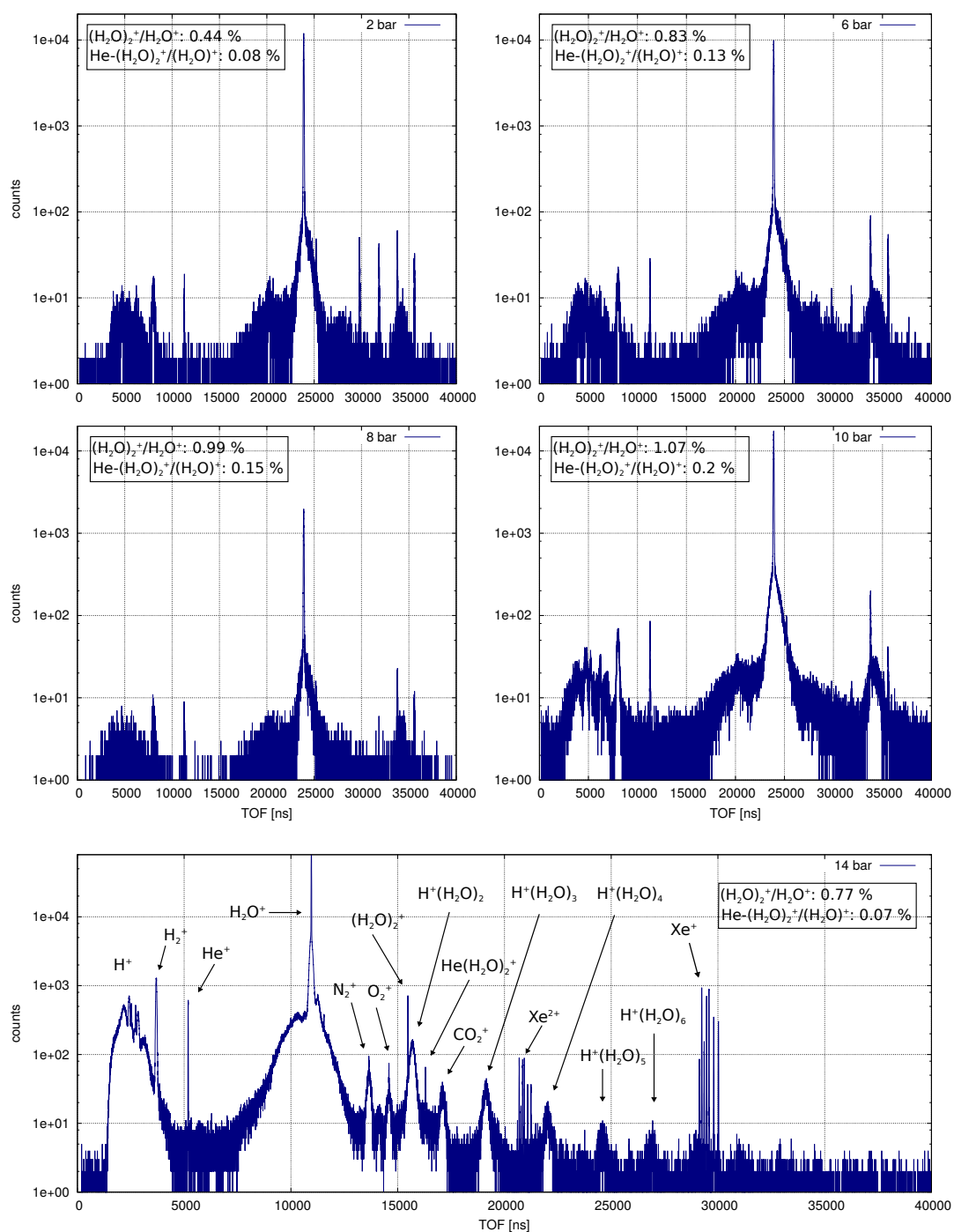


Figure 3.9: Water spectra for different pressures with Helium as carrier gas.

Helium was also investigated as a carrier gas. It is the lightest element of the noble gases and stresses the pumping system less than the other noble gases. Therefore, larger backing pressures can be employed. In figure 3.9, five measurements at room temperature for different backing pressures are depicted.

A comparison with Neon seeding for same backing pressures shows, that the water dimer yield  $(\text{H}_2\text{O})_2$  for Helium seeding is lowered. This can be explained with the larger mass difference of He to  $(\text{H}_2\text{O})_2$  than in the case of Neon. The maximum water dimer yield of 1.07 % is found for 10 bar backing pressure. For larger backing pressures (14 bar), the dimer yield decreases again (0.77 %). This effect is explained in section 2.1.2 “Carrier Gas”). With increasing backing pressure the cooling rate increases, but it is getting less probable for two water molecules to collide and form a dimer. Eventually, at large backing pressures, the reduced collision effect dominates the cooling effect and the dimer yield decreases.

There is a narrow peak at time of flights for  $\frac{m}{q} = 40$  particles. This is probably He- $(\text{H}_2\text{O})_2$ , as there are no other reasonable compounds with this mass to charge ratio. The abundance of He- $(\text{H}_2\text{O})_2$  also peaks for 10 bar Helium backing pressure.

#### 3.3.4 Argon Seeding

Another carrier gas which was investigated is Argon. It is twice as heavy as Neon, so one anticipates a different effect on clustering. The most abundant Argon atom  $^{40}\text{Ar}$  has a very similar mass to the water dimer  $u = 38$ . Therefore, collisions are most effective, in terms of kinetic energy transfer. This consideration goes along with our investigations, as the highest water dimer yields were obtained with Argon seeding (compare section 3.4).

In figure 3.10 we employed three different backing pressures without any heating. In contrast to the previous Neon spectra, doubly charged Argon ions are found. They emerge due to the lower ionization potential of the singly charged ion ( $I_p(\text{Ne}^+) = 41 \text{ eV}$ ,  $I_p(\text{Ar}^+) = 27.6 \text{ eV}$ ). The lower ionization potentials of Argon are also the reason why the Argon monomer peak is the most dominant in the spectrum.

For larger backing pressures, the fraction of water monomers compared to the  $^{40}\text{Ar}^+$  ions decreases. While for 1 bar there is about one order of magnitude difference, the discrepancy goes up to almost 2 orders of magnitude for 6 bar backing pressure.

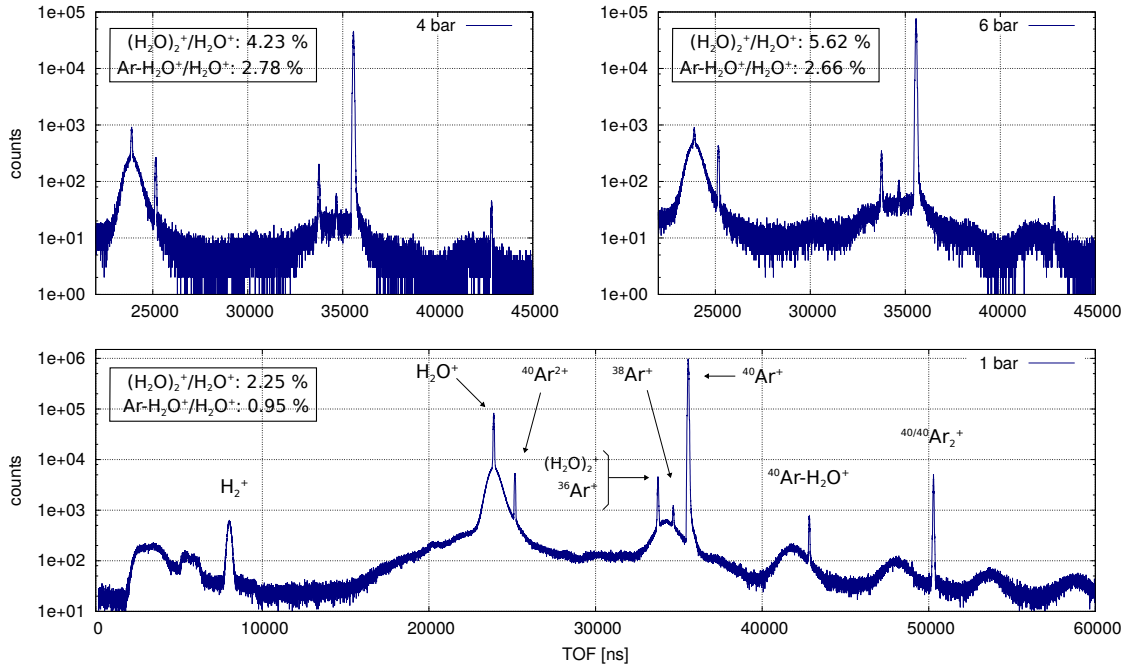


**Figure 3.10:** Argon seeded water spectra, taken at different temperatures and pressures.

Evaporation from the water surface is hindered, due to the increased Argon backing pressure. Therefore all water compounds decrease with larger carrier gas pressures.

Isotope	Abundance
$^{36}\text{Ar}$	0.337 %
$^{38}\text{Ar}$	0.063 %
$^{40}\text{Ar}$	99.6 %

**Table 3.2:** Natural Argon abundance [38]

Even though the  $^{40}\text{Ar}$  atom is by far the most dominant Isotope of Argon, we have to consider the less abundant species. Unfortunately the  $^{36}\text{Ar}^+$  and the water dimer  $(\text{H}_2\text{O})_2^+$  have the same mass to charge ratio and cannot be distinguished in the TOF spectrum. For determining the water dimer yield, one has to take the isotopes abundance into account (compare table 3.2) and subtract the  $^{36}\text{Ar}^+$  contribution to the peak. The corrected water dimer yields can be found in section 3.4.

The conclusion is again, that for higher backing pressures the formation of water dimers is enhanced. The only limitation to go to even higher pressures, is the performance of our pumping system. High pressures and heavy gases cause massive stress on the pumps.

Because of the technical restrictions, we cannot exploit the full clustering enhancement of a seeding gas. We would expect, that for rising backing pressures,



the decreasing water evaporation rate, would eventually lead to a maximum of the water dimer yield. This simply occurs as it is getting less probable for water molecules to collide and form a cluster. (see section “Carrier Gas” 2.1.2)

A first indication of the described process to set in, might be the lowering gains of the dimer yield with increasing backing pressure. There is also the Ar H<sub>2</sub>O cluster, whose yield starts to decrease somewhere between 4 and 6 bar (see section 3.4).

#### 3.3.5 Xenon Seeding

Seeding with Xenon turned out to be the most challenging. The large Xenon atom gets easily ionized, so the laser intensity has to be reduced, in order to protect the MCPs from damage. On the contrary one has to make sure, to still ionize water. Furthermore, the backing pressure has to be reduced drastically, first to preserve the pumps, but also to decrease the Xenon fraction.

The TOF spectrum (figure 3.11) shows many peaks at the positions of Xe<sup>+</sup>, Xe<sup>2+</sup> and Xe<sub>2</sub><sup>+</sup>. These are attributed to the seven stable isotopes and the two long lived isotopes of Xenon. For Xenon dimers there are even more peaks than nine, since isotopes can pair up in different combinations.

With the chosen set of parameters (0.3 bar backing pressure, no heating, 30 μm nozzle diameter), there were no Xe-H<sub>2</sub>O clusters. Probably one has to go to higher backing pressures to produce these compounds. The numerous isotopes are also a reason for weak signals of the water Xenon dimers.

Despite the small backing pressure, water dimers formed in a considerable fraction of 4.25 %. For experiments which employ solely water dimers, a Xenon seeding cannot be recommended. The massive Xe monomer peak saturates detectors and the forcibly low backing pressures clash with supersonic expansion.

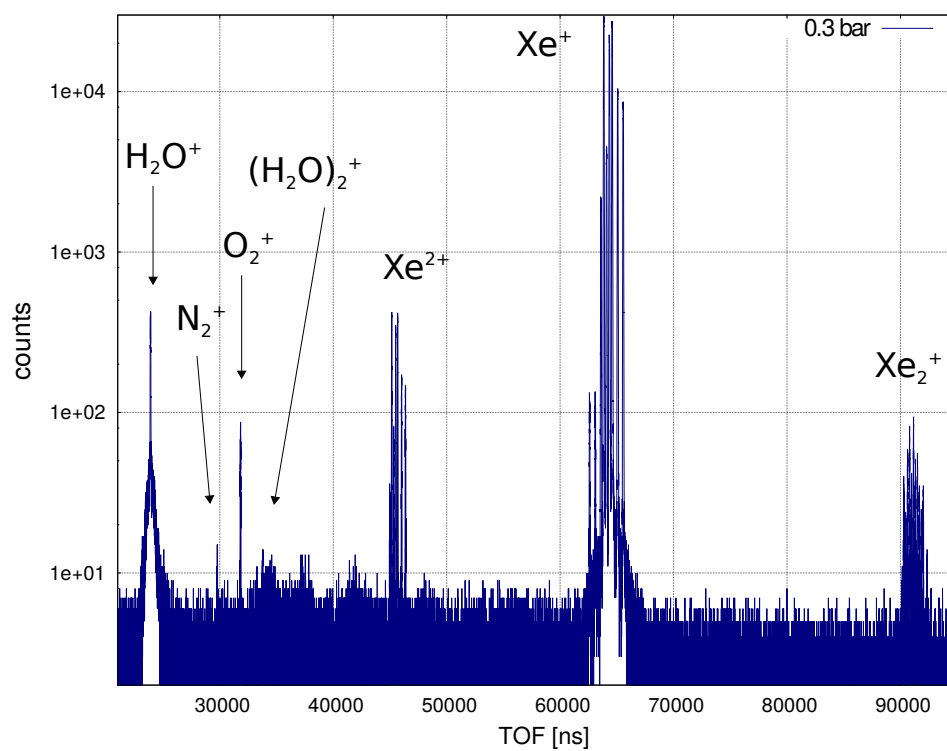


Figure 3.11: Xenon seeded water spectra, taken at room temperatures.

### 3.4 Seeding Results Overview

A list of the results on cluster yields, for different pressures, temperatures and carrier gases.

Seeding Gas		Yield (relative to H <sub>2</sub> O <sup>+</sup> )														
		Backing Pressure [bar]														
		1	2	4		6		8		10	14	0.3		0.66	1.05	1.6
		44 °C	44 °C	44 °C	70 °C	44 °C	70 °C	44 °C	70 °C	44 °C	44 °C	44 °C	70 °C	88 °C	107 °C	117 °C
He	(H <sub>2</sub> O) <sub>2</sub>		0.44 %			0.83 %		0.99 %		1.07 %	0.77 %					
	He (H <sub>2</sub> O) <sub>2</sub>		0.08 %			0.13 %		0.15 %		0.2 %	0.07 %					
Ne	(H <sub>2</sub> O) <sub>2</sub>	0.56 %	0.76 %	1.24 %	0.72 %			1.9 %	1.32 %							
	Ne H <sub>2</sub> O	0.11 %	0.21 %	0.51 %	0.2 %			1.31 %								
Ar	(H <sub>2</sub> O) <sub>2</sub>	2.25 %		4.23 %		5.62 %										
	Ar H <sub>2</sub> O	0.95 %		2.78 %		2.66 %										
Xe	(H <sub>2</sub> O) <sub>2</sub>															4.25 %
Pure Water	(H <sub>2</sub> O) <sub>2</sub>												0.15 %	0.19 %	0.18 %	0.17 %

## 4 Photon-Atom Interaction

In atoms, electrons are bound to the nucleus, consisting of protons and neutrons. The electrons only occupy distinct states centered on the nucleus, described by a set of quantum numbers. The principal quantum number  $n$ , denotes the electron shells around the nucleus, which corresponds to a range of binding energy. Within a shell, electrons are distinguished by their orbital angular momentum  $\ell = 0, 1, 2, \dots$ , also denoted with  $s, p, d, \dots$ . One is also speaking of subshells, as the electrons have certain spatial probability densities, corresponding to their angular momentum. All electrons within a shell  $n$ , form a spherical density distribution, reinforcing to use the term “shell”. The angular momentum  $\ell$  can have specific orientations relative to a chosen quantization axis:  $m_\ell = 0, \pm 1, \pm 2, \dots$  for  $|m_\ell| \leq \ell$ .

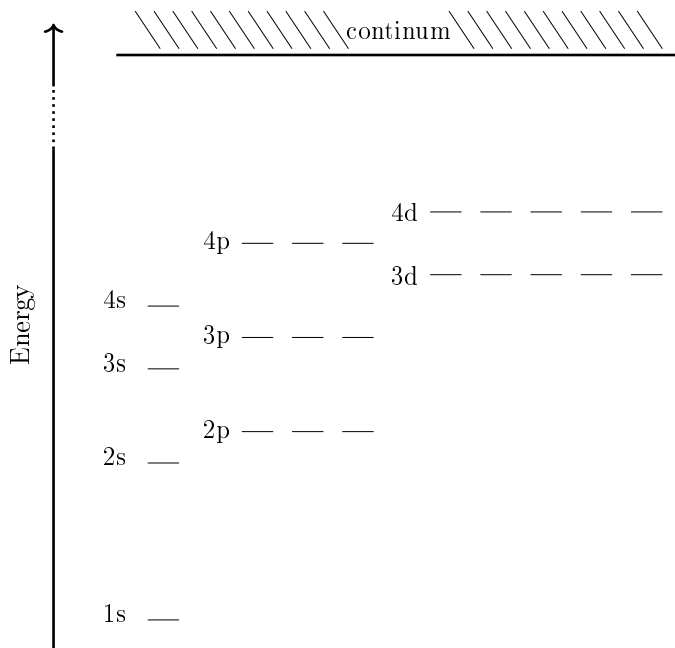


**Figure 4.1:** *Basic energy level scheme in an atom.*

Another angular momentum like quantum number is the spin. It is an intrinsic

property of particles and also has quantized values. Electrons are spin-1/2 particles, while photons have spin 1. This is important for photon-induced transitions, as angular momenta can couple to each other. Further quantum numbers will not be considered, as they are not playing a decisive role in this context.

## 4.1 First-Order Dipole Transitions

For a first calculation of the interaction between atoms and photons, one commonly uses the electric dipole approximation. This is done via time-dependent perturbation theory in first order. Here, the temporal change of the electric field in the electromagnetic wave (or the photon) is considered.

This section and the following are compiled from “Atome, Moleküle und optische Physik Teil 1” [39] chapter 4.2 and 5.3.

The force on an electron in an oscillatory electric field is:  $\mathbf{F}_e = -e_0\mathbf{E}(\mathbf{r}, t)$ . The perturbation energy follows as:

$$\hat{U}(\mathbf{r}, t) = \mathbf{r} \cdot e_0\mathbf{E}(\mathbf{r}, t) = -\mathbf{D} \cdot \mathbf{E}(\mathbf{r}, t), \quad (4.1)$$

where  $\mathbf{r}$  is the distance of the electron to the nucleus and  $\mathbf{D}$  the electric dipole-moment. The electric field  $\mathbf{E}$  can be written in terms of the polarization vector  $\mathbf{e}$  and the field amplitude  $E_0$ :

$$\mathbf{E}(\mathbf{r}, t) = \frac{i}{2}E_0 \left( \mathbf{e} e^{i(\mathbf{kr}-\omega t)} - \mathbf{e}^* e^{-i(\mathbf{kr}-\omega t)} \right). \quad (4.2)$$

Typically, the atom is a lot smaller than the wavelength of the photon  $r_{\text{atom}} \ll \lambda$ , so we can make an expansion in  $\mathbf{kr} \ll 1$ . In first, order we obtain for the exponential:

$$\hat{U}(\mathbf{r}, t) = \frac{i}{2}E_0e_0\mathbf{r} \left( \mathbf{e} e^{i\omega t} - \mathbf{e}^* e^{-i\omega t} \right), \quad (4.3)$$

$$\hat{U}(\mathbf{r}, t) = \frac{i}{2}T_0 \left( \hat{\mathbf{T}} e^{i\omega t} - \hat{\mathbf{T}}^* e^{-i\omega t} \right). \quad (4.4)$$

$\hat{U}(\mathbf{r}, t)$  is the time dependent perturbation of the electron in an E-field. Quantities are merged into a transition amplitude  $T_0 = E_0e_0$  and a transition operator  $\hat{\mathbf{T}} = \mathbf{r}\mathbf{e}$ . The time dependent Hamiltonian  $\hat{H}(t)$  is a combination of the stationary Hamiltonian  $\hat{H}_0$  and the perturbation:

$$\hat{H}(t) = \hat{H}_0 + \hat{U}(\mathbf{r}, t). \quad (4.5)$$

In order to find the transition probability, the time-dependent Schrödinger equation needs to be solved:

$$\left[ \hat{H}_0 + \hat{U}(\mathbf{r}, t) \right] |\Psi(\mathbf{r}, t)\rangle = i\hbar \frac{\partial}{\partial t} |\Psi(\mathbf{r}, t)\rangle . \quad (4.6)$$

For an ansatz, we make use of solutions of the stationary Schrödinger equation in 0<sup>th</sup> order, with a “trivial” time dependence:

$$\Psi_j^{(0)}(\mathbf{r}, t) = \psi(\mathbf{r}) e^{-i\omega_j t} , \quad (4.7)$$

where  $\hbar\omega_j$  is the energy of the corresponding state  $|j\rangle$ . If all  $|j\rangle$  form a complete basis, an exact solution can be given with a summation over the entire set. Additionally, we need to introduce time-dependent coefficients  $c_j(t)$ , also called probability amplitudes. Thus, time dependence prevails, when the absolute square is taken. The probability to find the final state  $|j\rangle$  after time  $t$  is:  $w_j(t) = |c_j(t)|^2$ .

The ansatz for equation 4.6 follows:

$$\Psi(\mathbf{r}, t) = \sum_{j=0}^{\infty} c_j(t) e^{-i\omega_j t} \psi_j(\mathbf{r}) = \sum_{j=0}^{\infty} c_j(t) e^{-i\omega_j t} |j\rangle \quad (4.8)$$

and inserted:

$$\sum_{j=0}^{\infty} c_j(t) e^{-i\omega_j t} \left[ \hat{H}_0 + \hat{U}(\mathbf{r}, t) \right] |j\rangle = i\hbar \sum_{j=0}^{\infty} \frac{\partial c_j(t) e^{-i\omega_j t}}{\partial t} |j\rangle . \quad (4.9)$$

Quantities which stay unaffected by a particular operator, were moved in front of it for clarification. In the following, we simplify the equation. On the left side,  $\hat{H}_0 |j\rangle = E_j$  is used and the differentiation is done on the right:

$$\sum_{j=0}^{\infty} c_j(t) e^{-i\omega_j t} \left[ E_0 + \hat{U}(\mathbf{r}, t) \right] |j\rangle = i \sum_{j=0}^{\infty} \left[ c_j(t) (-i\hbar\omega_j) e^{-i\omega_j t} + \hbar e^{-i\omega_j t} \frac{\partial c_j(t)}{\partial t} \right] |j\rangle \quad (4.10)$$

$$\sum_{j=0}^{\infty} c_j(t) e^{-i\omega_j t} \hat{U}(\mathbf{r}, t) |j\rangle = i\hbar \sum_{j=0}^{\infty} e^{-i\omega_j t} \frac{\partial c_j(t)}{\partial t} |j\rangle \quad (4.11)$$

In equation 4.11, two terms cancel out, as  $i(-i\hbar\omega_j) = E_j$ .

A multiplication with  $\langle b| e^{i\omega_b t}$  from the left and  $\langle b|j\rangle = \delta_{bj}$  give a system of linear

differential equations:

$$\frac{dc_b(t)}{dt} = -\frac{i}{\hbar} \sum_{j=0}^{\infty} c_j(t) \langle b | \hat{U}(\mathbf{r}, t) | j \rangle e^{i(\omega_b - \omega_j)t}. \quad (4.12)$$

Equation 4.12 is still exactly valid. In practice however, one only can consider a finite amount of orders, where the assumption of a small perturbation  $\hat{H}_0 \gg \hat{U}(\mathbf{r}, t)$  can be used. Under this assumption, the initial state amplitude  $c_a$  remains constant over time, whereas the other amplitudes  $|c_j(t)| \ll 1$ .

To start off with the system of equations 4.12, the 0<sup>th</sup> order is inserted:  $c_a^{(0)}(t) = 1$  and  $c_j^{(0)}(t) = 0 \quad \forall j \neq a$ .

$$|\Psi(\mathbf{r}, t)\rangle \approx |a\rangle e^{-i\omega_a t} \quad \rightarrow \quad \frac{dc_b(t)}{dt} = -\frac{i}{\hbar} \hat{U}_{ba} e^{i\omega_{ba} t} \quad (4.13)$$

$$c_b(t) = -\frac{i}{\hbar} \int_0^t \hat{U}_{ba}(t') e^{i\omega_{ba} t'} dt' \quad (4.14)$$

Where the abbreviation  $\omega_{ba} = \omega_b - \omega_a$  and for the matrix element  $\hat{U}_{ba} = \langle b | U(\mathbf{r}, t) | a \rangle$  is used. Inserting equation 4.4 with the analogous  $T_{ba}$  leads to:

$$c_b(t) = \frac{T_0}{2\hbar} \int \left( \hat{T}_{ba} e^{i(\omega_{ba} - \omega)t'} - \hat{T}_{ba}^* e^{i(\omega_{ba} + \omega)t'} \right) dt', \quad (4.15)$$

$$c_b(t) = \frac{T_0}{2\hbar} \left( \frac{\hat{T}_{ba} e^{i(\omega_{ba} - \omega)t}}{i(\omega_{ba} - \omega)} - \frac{\hat{T}_{ba}^* e^{i(\omega_{ba} + \omega)t}}{i(\omega_{ba} + \omega)} \right). \quad (4.16)$$

This is the transition amplitude in first-order time-dependent perturbation theory. It comprises some important information for processes we are interested in. The oscillatory exponential functions give only notably contributions for  $\omega_{ba} \pm \omega = 0$ . Otherwise, they will vanish in the limit of large times. Furthermore, at this energy constellation, the denominators increase contributions drastically.

The first term describes the absorption of a photon  $\hbar\omega$ , where the energy difference of final state  $b$  and initial state  $a$  is positive. The second term is attributed to stimulated emission, where  $\omega_{ba} < \omega$ .

In summary, the frequency (or energy, wavelength) of the incoming photon must match the energy difference in the atom, to drive the transition efficiently.

Another result we could gain, is the intensity dependence of the transition probability:

$$w_{ba}^{(1)}(t) = |c_b(t)|^2 \propto |T_0|^2 \propto |E_0|^2 \propto I. \quad (4.17)$$

A single photon process scales linearly with intensity.

## 4.2 Two- and Multi-Photon Excitation

In the previous section 4.1, first-order perturbation theory was introduced. The evaluation showed, that for an efficient transition, the frequency  $\omega$  of the incoming photon, needs to match the corresponding energy difference  $\hbar\omega_{ba}$  between states  $a$  and  $b$ , in the atom. Thereby, the required energy is carried by a single photon. In the following consideration, second-order perturbation theory is applied, leading to two-photon absorption.

To obtain the second order, we insert the result for the first order 4.16 into the differential equation 4.12.

$$c_b(t) = \frac{-iT_0^2}{4\hbar^2} \int dt \sum_{\gamma} \left( \frac{\hat{T}_{b\gamma} \hat{T}_{\gamma a} e^{i(\omega_{ba}-2\omega)t}}{\omega_{\gamma a} - \omega} + \frac{\hat{T}_{b\gamma}^* \hat{T}_{\gamma a} e^{i\omega_{ba}t}}{\omega_{\gamma a} - \omega} + Em \right) \quad (4.18)$$

Emission terms are abbreviated with  $Em$ . They are analogous to the shown absorption terms, but with differing signs. The exponent  $\omega_{ba} - 2\omega$  shows clearly the photon absorption. In first order, for a single photon (compare eq 4.16), there was just the single wavelength  $\omega$ . Now the transition energy of  $\hbar\omega_{ba}$  is gained by absorbing two photons, each with half the frequency, compared to the single photon case. The summation has to be done over all intermediate states  $|\gamma\rangle$ . In practice, it is often sufficient to consider the major contributions, to get a decent result.

An interesting relation for the presented data, is the intensity dependence of the transition probability  $\omega_{abs}^{(2)}$ . From equation 4.18 one finds:

$$\omega_{abs}^{(2)} \propto T_0^4 \propto I^2 \quad (4.19)$$

In a similar way one can show, that the  $n^{th}$  order corresponds to an  $n$  photon



process, resulting in a  $n^{\text{th}}$  power intensity dependence:  $\omega_{abs}^{(n)} \propto I^n$ .

This relation shows, that for low intensities ( $I < 1$ ) the single photon absorption is dominating by far. Higher order processes however get more and more important with increasing intensity and can eventually dominate lower order processes (for  $I \geq 1$ ).

# 5 Interatomic Coulombic Decay (ICD)

## 5.1 ICD in General

Interatomic or Intermolecular Coulombic Decay is a very efficient relaxation process for atoms and molecules in weakly bound systems (Cederbaum *et al.* [3]). The term “Interatomic Coulombic Decay” gives already an idea what kind of physics is involved. “Interatomic” is the key word, as it distinguishes from other well-known relaxation and decay mechanisms like Auger decay, radiative decay or autoionization. These processes take place in a single atom or molecule. However for ICD to happen, the environment of the excited atom is crucial. The excess energy is released via a neighboring atom, which subsequently undergoes ionization. The emitted electron is called ICD electron. The second term “Coulombic decay”, refers to the decay being field mediated. Similar to Auger decay, two electrons are emitted in total. While Auger decay takes place in a single atom or molecule, in ICD the charge is distributed and both constituents end up singly charged. Due to the Coulomb force they strongly repel each other and fly apart. This so called “Coulomb Explosion” can be an indicator for ICD.

A first direct evidence for ICD was brought in 2003, in Van-der-Waals bound Neon dimers [4]. A step by step illustration of the mechanism is shown schematically in figure 5.1. The two energy level pictographs next to each other illustrate the two Neon atoms of the dimer. For a first approximation and because of the weak bond, levels are not shifted, i.e. the constituents can be considered as if they were unbound.

In the first step, a photon of sufficient energy produces an inner-valence vacancy in one Neon atom. In the depicted case, a 2s electron is brought into the continuum, which requires a minimum energy of 48.46 eV<sup>1</sup>. During the next step, a 2p electron fills the 2s vacancy in the Ne<sup>+</sup> ion, releasing the energy of 26.9 eV<sup>1</sup>. This energy however is not sufficient to emit a second electron within the same ion, since ionization potentials are higher ( $I_p(\text{Ne}^+) = 41 \text{ eV}^1$ ) compared to a neutral atom.

---

<sup>1</sup>NIST Atomic Spectra Database [40]

Here, the neighboring, neutral Neon atom comes into play. It employs an ionization potential of  $21.5\text{eV}^1$ , which is low enough for a  $2p$  electron to get emitted. This electron is called ICD electron, since it was set free due to the inter-atomic interaction mediated by a virtual photon. Finally, both atoms of the dimer are singly charged, both exhibiting a  $2p$  vacancy. Consequently, the strong Coulomb repulsion tears the dimer apart. This is referred to as a Coulomb explosion.

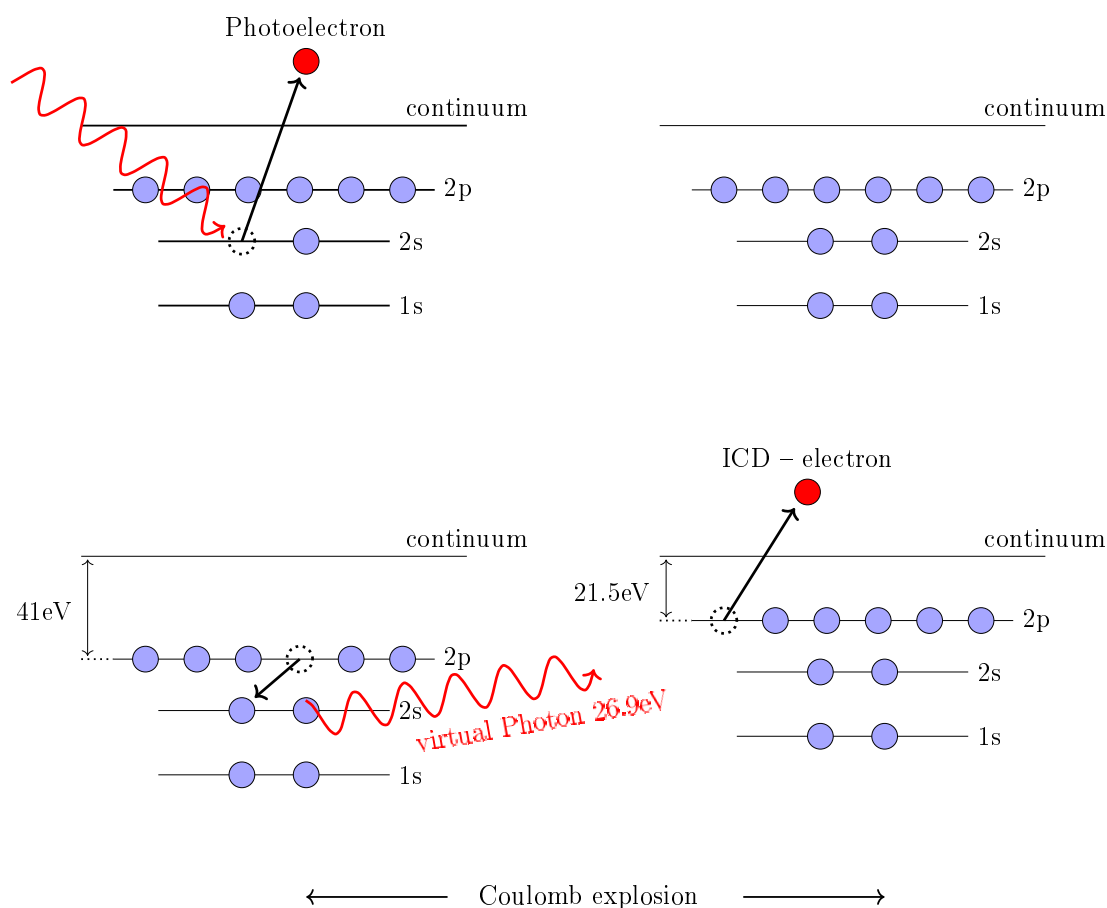


**Figure 5.1:** *ICD in a Neon-Dimer: Absorbing the photon leaves a inner-valence vacancy. Subsequently, a  $2p$  electron fills the  $2s$  vacancy. The released energy is mediated to the neighboring atom via a virtual photon.  $26.9\text{eV}$  are sufficient to ionize the neutral atom and an ICD electron is emitted. Finally, the two ions Coulomb explode.*

## 5.2 Resonance-Enhanced ICD

In the previous case of ICD, the photon energy was not precisely specified, as it should be just sufficient for an inner-valence ionization. In this case however, the 2s-2p resonance in  $\text{Ne}^+$  is used to trigger ICD. In figure 5.2, the process is illustrated schematically, again in a Neon dimer.

A first photon ionizes one Ne atom. The ejected electron is a valence electron from the 2p state. In the following step, the same atom (now ion) absorbs a second photon. For this absorption to be most efficient, the photon energy should match the transition from 2s to 2p (26.9 eV) in the  $\text{Ne}^+$  ion. In the third step, the  $\text{Ne}^+(2s^{-1})$  ion de-excites and the released energy is used to eject a valence electron of the neutral, neighboring Neon atom. Similar to the conventional ICD, the released energy is not sufficient to eject an electron in the ion, but to ionize the neutral neighbor atom.

The radiative decay lifetime of  $\text{Ne}^+(2s^{-1}) \rightarrow \text{Ne}^+(2p^{-1})$  is  $\tau_{\text{rad}} \approx 0.14$  ns Ref. [41] and therefore takes place on a much larger timescale than ICD  $\tau_{\text{ICD}} \approx 150$  fs (Schnorr *et al.* Ref. [42]). Thus, radiative decay is suppressed under these conditions.

The final configuration is again the 2p outer-valence vacancy of both Neon atoms. The following Coulomb explosion fragments the molecule.

The chosen photon energy is too small to directly ionize an inner valence electron, like described in section 5.1. Therefore the probability for ICD to happen drops, if one detunes the photon energy from resonance. This can be used as a clear indicator for the resonance-enhanced ICD.

Another decisive difference to the process described in section 5.1, is the total number of involved photons. While in the first case ICD is triggered by a single photon, two photons are needed in the presented resonance-enhanced case. This distinction will matter, if one investigates the intensity dependence.

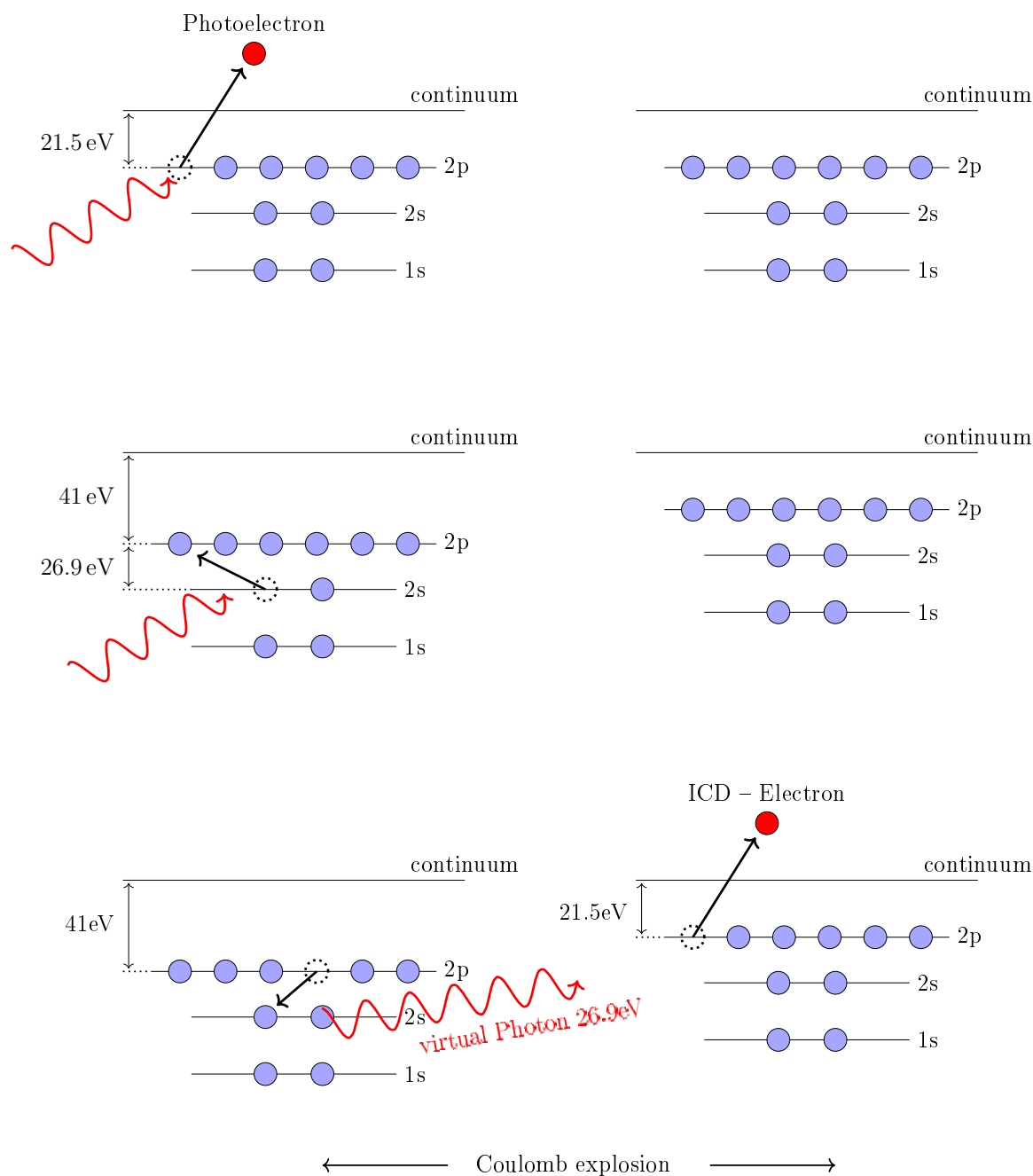


**Figure 5.2:** Resonance enhanced ICD in Neon-Dimers: There are two photons absorbed in total. The first leads to an emission of a 2p valence electron. The second photon has the matching energy of 26.9 eV to drive the 2s  $\rightarrow$  2p transition in the Ne<sup>+</sup>(2p<sup>-1</sup>) ion. The third row shows how the 2s vacancy is filled by a 2p electron of the same ion and the released energy leads to an emission of an ICD electron in the neighboring atom. Finally, both Ne atoms are singly charged and Coulomb explode.

There is a competing mechanism in the Neon dimer (figure 5.3) [41] for the considered photon energies. It is also possible for the dimer to absorb two photons, each ionizing one of the two constituents. The final configuration would be the same as in the resonant case. The dimer is ionized twice and the two  $\text{Ne}^+(2p^{-1})$  ions Coulomb explode. However, there are two signatures to distinguish between the resonance-enhanced ICD and the competing mechanism. The ICD electron has always the same kinetic energy, because the de-excitation of the neighboring ion always releases the same amount of energy. This is at least valid for a short delay between first and second absorption, as then nuclear dynamics can be neglected. This is different for the competing mechanism, where the photoelectron can have different kinetic energies, depending on the photon energy.

A second indication is the photon energy dependent Coulomb explosion yield. While the resonance-enhanced ICD has an increased yield on the resonance, the yield of the competing mechanism stays constant over the small photon energy range, as the cross-section does not change too much.

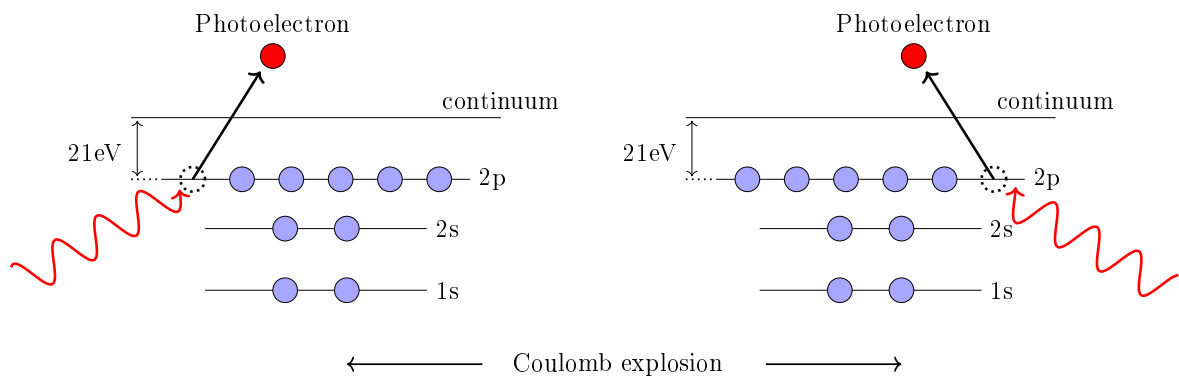


**Figure 5.3:** *Competing mechanism to resonance-enhanced ICD: Each atom of the dimer absorbs a photon and subsequently emits a photoelectron, resulting in  $(\text{Ne}^+(2p^{-1}))_2$ . Due to the charge repulsion, a Coulomb explosion takes place.*

# 6 Experimental Setup for the Neon Measurement

## 6.1 Overview: Heidelberg Reaction Microscope at FLASH2

For the presented experiment, we were using a Free-Electron Laser (FEL). In contrast to conventional lasers, one needs an entire facility to create FEL pulses (see sec. 6.2). In our case, the experiment was carried out at FLASH2 (Free-Electron Laser in Hamburg), the extension of FLASH1.

The interface between the FEL facility and the user experiment is an evacuated beamline ( $\approx 10^{-8} - 10^{-7}$  mbar). Here, the REMI setup (chapter 6.3) is mounted. The FEL needs to be in vacuum at all times, since high intensities and photon energies would lead to immediate absorption in air. In our detection scheme, we even go to much lower pressures to reduce the background.

Between the last FLASH flange and the main chamber, the pressure has to be lowered by about four orders of magnitude. This is done with three differential pumping stages, installed in a beamline before the REMI. Two neighboring stages are connected with small tubes ( $\varnothing \approx 1$  cm), providing a low conductance, due to the relatively small cross-sectional area. In this way, larger pressure differences can be sustained with a relatively short beamline. The beamline comprises several apertures and slits to clip the unfocused FEL and reduce stray light.

The FEL and the gas target jet intersect in the main chamber (see figure 6.1), where the detection of fragments takes place. Beamline and jet are therefore orientated perpendicularly. The gas jet is produced in the so-called “jet chamber”. For large backing pressures and large nozzles, the pressure here can be relatively high  $\approx 10^{-3}$  mbar. In order to reach as low pressures as in the main chamber, differential pumping is used again. In contrast to the beamline arm, gas is injected into the system, so turbo molecular pumps are stressed in particular.

On the opposing side of the jet chamber is the so-called “Jet dump”. The main part of the gas just crosses the main chamber without any interaction. To avoid

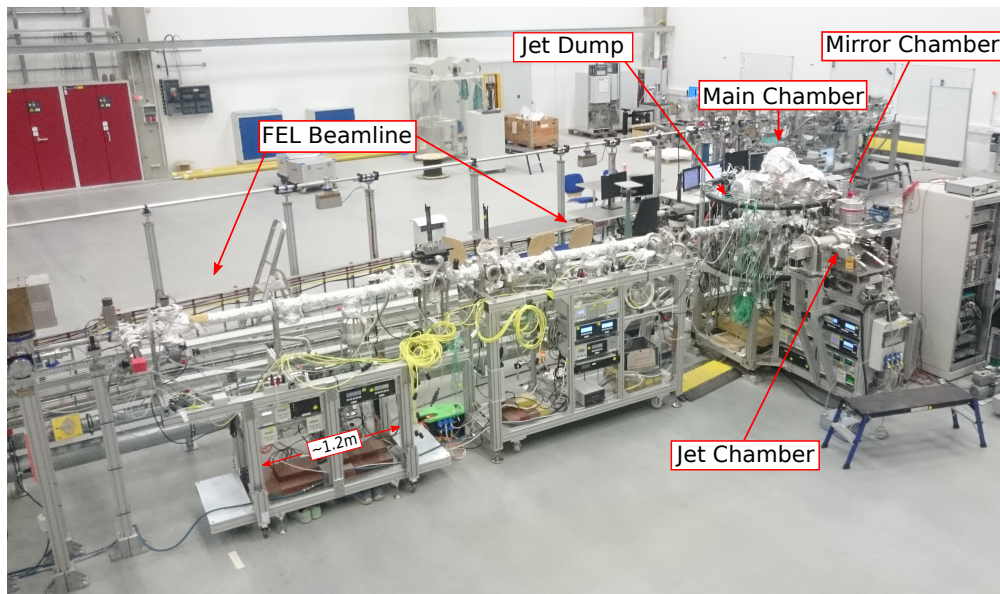


**Figure 6.1:** *Experimental Setup at FLASH2*

spoiling the vacuum, the jet ( $\phi=1-2$  mm) passes through a small tube and gets directly dumped into a turbo molecular pump.

The multilayer mirrors, which focus and back reflect the FEL, are housed in the so-called “mirror chamber”. It contains the piezo-driven delay stage of the split mirror and two goniometers, which rotate the mirror horizontally and vertically. The equipment in the mirror chamber accumulates a lot of surface, which leads to increased outgassing. Therefore, these parts are sourced out from the main chamber.

## 6.2 Free-Electron Laser - FLASH

The following explanations of FELs are compiled from [43, 44].

Free-electron lasers resemble conventional lasers in some properties, as coherence and low divergence. This is also the reason why one speaks of a “Laser” (**L**ight **a**mplification by **s**timulated **e**mission of **r**adiation), even though there is no stimulated emission involved. The main difference is the production of photons. FELs are based on synchrotron radiation, i.e. light emission of accelerated charged particles.

A linear accelerator brings electrons to relativistic velocities. Then, they are guided in bunches into a undulator ( figure 6.2). This is an alternating arrangement of



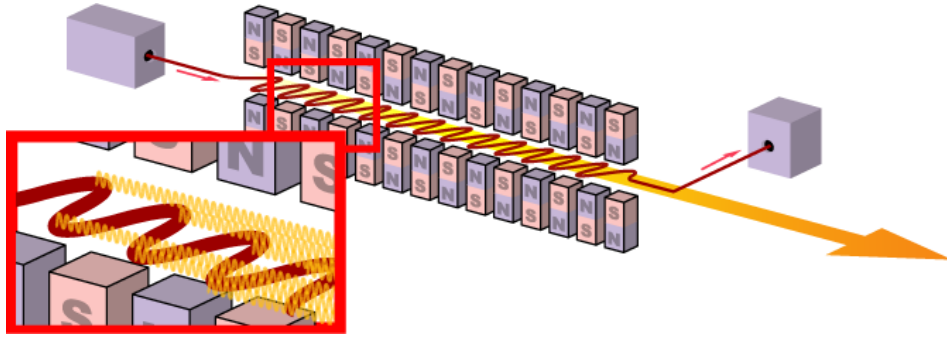


**Figure 6.2:** *FEL principle: Electrons are accelerated to relativistic energies and pass the undulator. The alternating  $B$ -field, leads to an oscillating motion of the electrons. Synchrotron radiation is emitted and generates coherent light due to the microbunching effect. Finally, the electrons are deflected, but the photon beam prevails. (fig. from [45])*

opposing, strong magnets. The electrons perform a wiggling motion and emit synchrotron radiation, mainly at the turning points where the acceleration is largest. Photons are emitted in a narrow cone in forward direction, due to the relativistic electron velocity.

The photon's wavelength  $\lambda$  has a quadratic dependence on the Lorentz factor  $\gamma^{-1} = \sqrt{1 - \frac{v^2}{c^2}}$ , with  $v$  the electron velocity. Due to relativistic length contraction, the undulator period  $\lambda_u$  of the magnets is reduced to  $\lambda_u^* = \lambda_u/\gamma$ , in the rest frame of the electrons. In this frame, the electrons oscillatory frequency is  $\nu^* = c/\lambda_u^* = c\gamma/\lambda_u$ . Looking against the beam in the laboratory frame, an observer will see a Doppler-shifted photon frequency  $\nu = \gamma(1 + \beta)\nu^*$ , with  $\beta = \frac{v}{c}$ .

$$\lambda = \frac{\lambda_u}{\gamma^2} \frac{1}{1 + \beta} \approx \frac{\lambda_u}{2\gamma^2} \quad \text{for } v \approx c \quad (6.1)$$

Equation 6.1 shows, the larger the electrons velocity, the higher is the photons energy (the lower is  $\lambda$ ). Aiming to produce intense pulses at small wavelengths, FEL facilities around the world use large accelerators.

During the passage through the undulator, the electron bunch undergoes a process called microbunching. The electrons move in the generated electromagnetic wave and arrange in its electric field. Depending on the position in the field, electrons are de- or accelerated. Finally the bunch splits up into micro bunches, separated by half the wavelength of the electromagnetic wave. Within such a “microbunch”, the electrons move as a collective and act like a single particle with the charge  $N \cdot e$ . With growing intensity the effect gets larger and finally the FEL's intensity scales

quadratically with the number of electrons within a microbunch  $I \propto N^2$ . This “microbunching” process is a decisive difference to ordinary synchrotron radiation, where the electrons are uncorrelated and emit their radiation independently. The autonomous movement results in a linear scaling of the intensity with electron number  $N$ .

In the case of FLASH, the process of microbunching is initiated by spontaneous emission of undulator radiation, called “self-amplified spontaneous emission” (SASE). This radiation is amplified in the first section of the undulator and serves as a seeding beam in the rest of the undulator.

The stochastic nature of the process leads to “spectrally broad and noisy pulses with poor temporal coherence” [44]. SASE also leads to changes of these properties and intensity from pulse to pulse.

### 6.3 Reaction Microscope

A Reaction Microscope, commonly abbreviated REMI, is the tool of choice for time-resolved, kinematically complete measurements. Therefore, experiments on molecule reactions and dynamics can be analyzed in detail. It allows to detect charged fragments, namely ions and electrons. A time of flight (TOF) spectrum can be recorded, which is used to determine mass and charge state of the particles. In addition to the time information, spatial information is measured. The combination of these information makes it possible to reconstruct the initial momenta of all involved fragments in coincidence. In the context of REMI usage, one sometimes refers to COLTRIMS (Cold Target Recoil Ion Momentum Spectroscopy [46]), to describe the applied technique.

Our REMI setup is schematically shown in figure 6.3. Here, the unfocused FEL is propagating from the left and passes through the spectrometer. On the opposite side, the FEL beam gets back reflected and focused into the interaction region. A split mirror can be used to create two replica-pulses, which can be delayed with respect to each other. This allows to perform pump-probe experiments. Perpendicular to the FEL beam, a continuous gas jet crosses. It is chopped and skimmed such that its radial extent is about or less than 1 mm. In the overlap region of the gas jet and the FEL, the majority of fragments is created. A homogeneous electric field along the vertical direction, accelerates positive ions to the top and

negatively charged electrons to the bottom detector. The electric field is created by a spectrometer, which is a stack of equally spaced metal rings, connected via a chain of resistors. Applying a voltage between the top and bottom ring creates the desired homogeneous electric field.

At the ends of the spectrometer are time and position resolving detectors (figure 6.4). Each is a combination of microchannel plates (MCP) and delay lines.

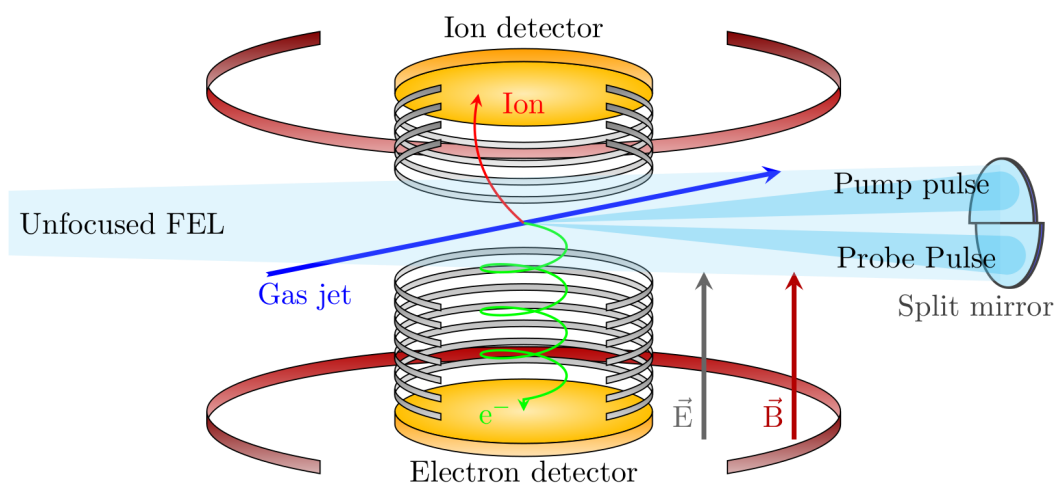


**Figure 6.3:** *Our Reaction Microscope: The FEL beam passes through the main chamber and is back reflected and focused into the target region, where the gas jet crosses. The charged fragments are accelerated in an electric field towards the detectors. The field is generated by ring electrodes, indicated in silver. The two red rings symbolize a pair of Helmholtz coils. In their magnetic field, electrons move on spirals and cannot fly off the detector. (figure from [44])*

One has to make sure, that the reaction products do not fly off the detector, i.e. hit the spectrometer rings somewhere before. This can happen because Coulomb explosions may lead to relatively large radial momenta. To prevent particles from flying off the detector, either the acceleration voltage can be ramped up, or a homogeneous vertical magnetic field is applied. The Lorentz force makes the light electrons move on spiral trajectories inside the spectrometer, while the heavy ions are barely affected. The field is generated by a pair of Helmholtz coils outside the vacuum, shown red in figure 6.3.

The entire region within the spectrometer, including the detectors, need to be in ultra high vacuum (UHV). The high intensity and energetic photons of the FEL, ionize any kind of residual gas. This complicates measuring, as the detectors have

dead times and a limited multi-hit capability. If the demanded pressures of about  $10^{-11}$  mbar should be reached, some efforts have to be made. One uses vacuum chambers of annealed steel for low outgassing rates and differential pumping with a three level pump system. The gradient from high to low pressures starts with the pre-pump, via a compressor pump to tailored turbo molecular pumps. Moreover, the inside walls of the main chamber are NEG (non-evaporable getter) coated. This is a special Titanium-Zirconium alloy which adsorbs residual gas molecules [47]. This kind of pumping is referred to as passive pumping. To activate this coating, one has to heat up the material and with it the entire chamber to about 250 °C. The pros of this technique is the performance and the space-saving assembly. The inevitable bake-out however, is a massive stress for many parts of the experiment. Flange connections and weld seams are a likely source of leakage, during this process.

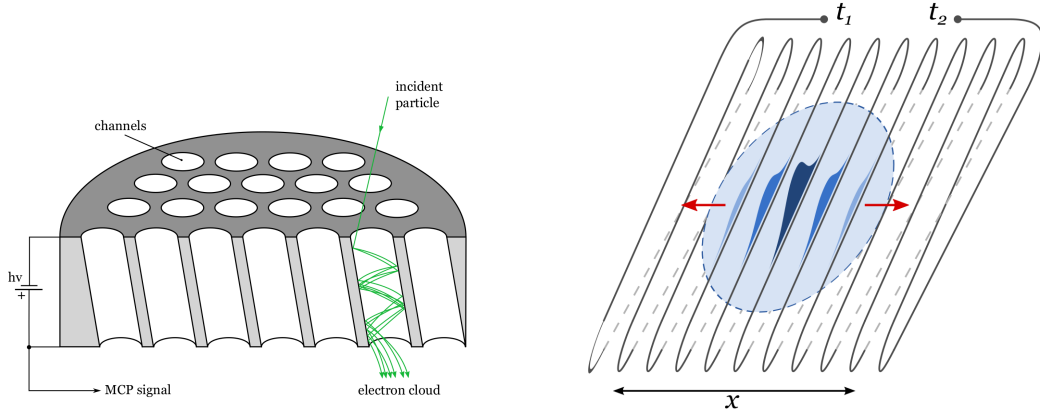
### The Detector

The following information on delay lines and MCPs is mainly taken from [44, 48]. Charged particles first impinge onto the MCP and initiate an electron cloud, bursting out on the other side. As described in the name “microchannel plate”, the 1 mm thick disc has many micrometer-sized capillaries (figure 6.4(a)). Each of these channels is an individual electron multiplier. A high voltage of about 1 kV is applied between front and back side, in order to accelerate secondary electrons. These electrons hit the channel wall again and even more electrons are emitted. This avalanche can amplify the original signal by a factor of  $10^4$ . The inner surface of each capillary is coated with a semiconductor material, exhibiting a low workfunction. The workfunction is the minimum energy which is required to remove an electron of the material. This facilitates the production of secondary electrons and therefore increases amplification. The resulting voltage drop is used as the timing signal for particles time of flight. The other timing signal for the TOF, is an external FEL trigger.

$$TOF = t_{MCP} - t_{trigger} \quad (6.2)$$

The electron cloud leaves a local positive charge in the MCP, which weakens the electric field intensity in the channel. Its amplification ability is hindered until the charge is neutralized by the so-called strip current. Due to the high resistance of an MCP (commonly lead glass), the strip current is small and takes some time for

the neutralization. This period is called dead time, because the channel is inactive until the strip current has vanished. Particles impinging into the channel within this time cannot initiate an electron avalanche, i.e. they are not detected.



(a) Microchannel plate: Gives the time information and amplifies the signal. Accelerates secondary electrons to set off an electron avalanche.

(b) Delay line: Gives spatial information. The MCP electron cloud kicks off a voltage pulse, propagating to the wire endings. The spot of impact is deducted from the run-time differences.

**Figure 6.4:** *Detector components: Fragments hit the MCP and create an electron cloud, which impinges on the delay line wires. (figure taken from [49])*

“Saturation” of the detector sets in, if the rate of impinging particles reaches a critical value, where the amplification drops drastically. This is a MCP specific threshold and typically found when the output current, quantified by the emitted electron cloud, reaches 5% to 6% of the strip current. An exemplary amplification curve of a MCP can be found in the appendix A.3.

The spatially sensitive part is the delay line or anode. It is mounted just behind the MCP, so the electron cloud directly impinges onto the delay line wire. In this manner, the signal is as sharp as possible. Practically, the delay line is one long copper wire, wrapped in non-touching loops (figure 6.4(b)). It is held on a positive potential, thus the name anode, so the electron cloud causes a voltage drop. The drop propagates to both ends of the wire, where the signal is recorded. Since the wire length is constant, both run times  $t_1$  and  $t_2$  add up to a constant total runtime. In this way, pulses of the same event can be matched, even though other signals may be found within the same time window. The multi-hit capability is based on this principle. Contrariwise, one can determine the impact position

from the runtime difference. Using a second delay line wire, which is orientated perpendicular to the first, enables to detect particles in two dimensions. Similar to the MCP, there are limitations to the multi-hit capability. Only about 2 to 3 events within the propagation time of the signal can be measured (about 8 ns in this case [44]).

## 7 Data Analysis - Resonance-Enhanced ICD

The goal of the experiment at FLASH in May 2016, was to investigate wavelength and intensity dependence of the resonance-enhanced ICD. FLASH2 allows this via a tunable undulator gap. Wavelength adjustments are made within seconds.

The variation in intensity comes naturally from the FEL. There are fluctuations both from shot to shot and over time ranges of minutes (see “SASE” in section 6.2).

An overview of the ion abundances, can be found in the time of flight spectrum (figure 7.1). The FEL ionizes atoms and molecules, which are accelerated in the electric field towards the MCP. The time it takes depends on the particle’s mass  $m$  and its charge state  $q$ , but also on technical conditions like the acceleration length  $d$  and the applied voltage  $U$ . The distance  $d$  is covered by a particle with acceleration  $a$  in time  $t$ , according to equation 7.1. In the second part of the equation the inertial force  $F$  is equated with the electric force on a charged particle:

$$d = \frac{1}{2}at^2 \rightarrow t = \sqrt{\frac{2d}{a}} \quad \text{and} \quad F = m \cdot a = \frac{qU}{d} \quad (7.1)$$

Solve for  $a$  and insert to get the TOF equation:

$$t = d \cdot \sqrt{\frac{2m}{qU}} \propto \sqrt{\frac{m}{q}} \quad (7.2)$$

In practice, it is often complicated to state the exact acceleration voltage and length. Thus, one takes a known peak and calculates the mass to charge ratio  $\frac{m}{q}$  or the TOF, relative to the unknown peak. Atomic masses and charge states come in integers, which makes an identification much easier. Voltages and lengths drop out:

$$t_1 = \sqrt{\frac{m_1}{q_1} \frac{q_2}{m_2}} \cdot t_2 \quad (7.3)$$

Broad peaks, like  $\text{N}_2^+$  or  $\text{H}_2\text{O}^+$ , belong to the residual gas. They are thermalized and therefore have a relatively broad momentum distribution. Additionally, they are produced along the entire FEL path (compare figure 7.8(a)), so they have differing flight distances and TOFs.

The sharp peaks belong to particles of the jet. Due to the supersonic expansion and the successive skimming and cutting of the gas jet, the translational velocity distribution gets very narrow. In the restframe of jet particles, typical “temperatures range from tens of millikelvin to a few kelvin” [44].

Two FEL pulses are separated by about 5000 ns. Heavy particles may take longer to reach the detector than this time span and appear in the “next” TOF spectrum at short times. To get the right time of flight, one has to add 5000 ns to the displayed time. In figure 7.1, this is the case for the Neon trimer. Changing the acceleration voltage shifts the peaks and stretches the axis. Here, all important fragments arrive within the first pulse spectrum.

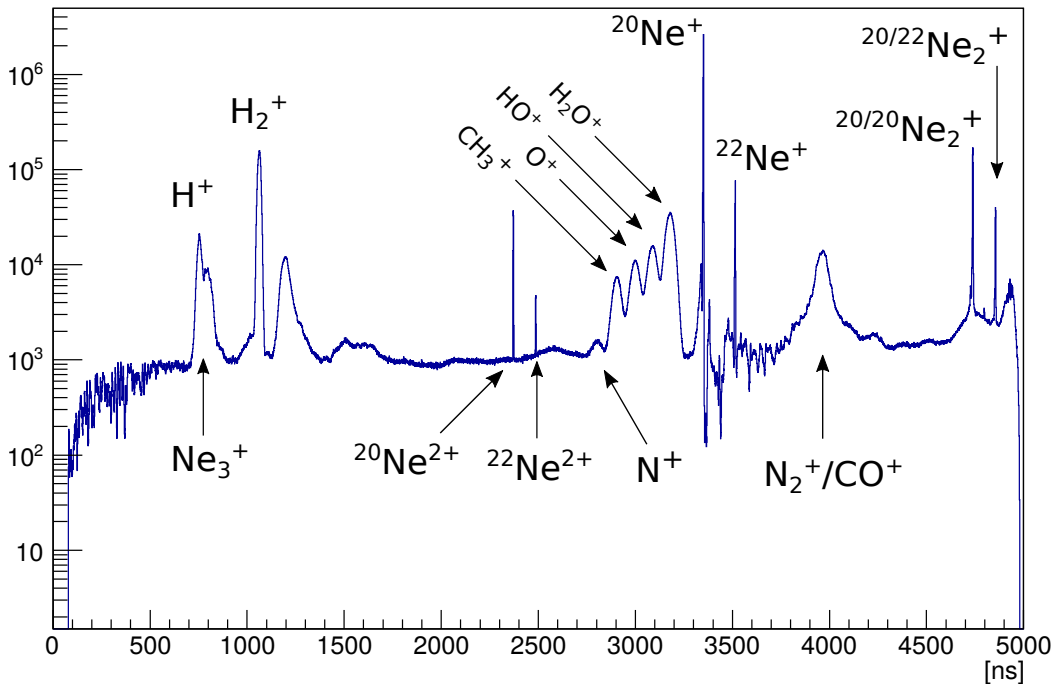


**Figure 7.1:** Time of flight spectrum of Neon at  $46.1 \text{ nm} \hat{=} 26.9 \text{ eV}$

The Neon gas jet was produced with room temperature gas and a backing pressure of 40 bar, which lead to a dimer to monomer ratio of about 11 %. These dimer yield-optimized conditions were systematically investigated in [50].



## 7.1 Isolate Coulomb Explosions

The signature for ICD are Coulomb-exploded Neon dimers, i.e.  $\text{Ne}^+$  ions with large momenta. If both ions of an event are detected, they can be matched. The matching done by applying conditions on the position and the time of flight. This combination gives an unambiguous coincidence based on matching, fully resolved momenta.

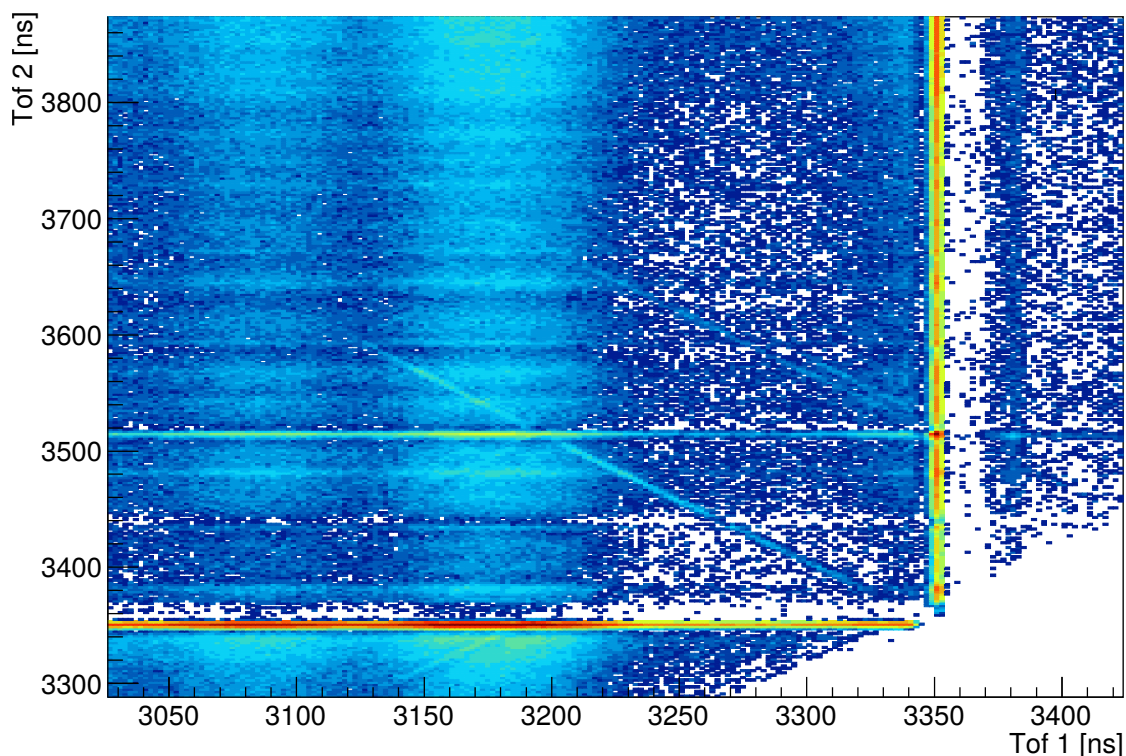


**Figure 7.2:** A PiPiCo-Plot: Diagonal lines are the signature for coulomb exploding dimers. A larger TOF of one constituent leads to a smaller TOF of the other.

Coulomb exploding ions show up on a diagonal line in the PiPiCo plot (“**p**hoto-**i**on **p**hoto-**i**on **C**oincidence”) (figure 7.2). In this 2D histogram, the first column shows the fastest ion plotted against all other ions arriving at later times. In the second column, the second fastest ion is plotted against all remaining ions arriving at later times and so on. In short, each ion time of flight is plotted against all other, larger ion time of flights. The color code gives information on how often a TOF-pair is found. It ranges from low to high counts with the color gradient going from blue to red.

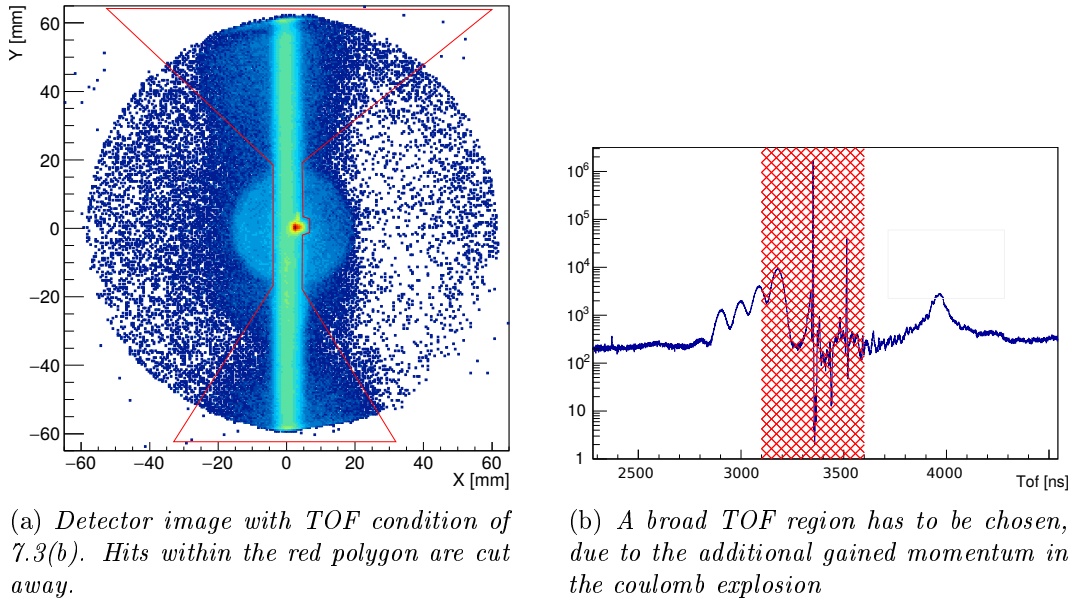


**Figure 7.3:** *Spatial (a) and temporal (b) condition to select  $^{20}\text{Ne}^+$ -ions of Coulomb explosions.*

In Coulomb explosions of dimers, the ions are emitted back to back, due to momentum conservation. The electron momentum can be neglected in good approximation. If the explosion axis has an  $z$ -direction contribution, one ion has momentum in  $+z$ -direction i.e. a shorter TOF, while the other has momentum in  $-z$ -direction, i.e. a longer TOF. This TOF discrepancy gets maximal if the explosion axis is  $z$ -aligned, but all other angles in between are also possible. We therefore obtain a diagonal line in the PiPiCo-Plot. There are also lines at larger time of flights which correspond to exploding dimers composed of isotopes ( $^{22}\text{Ne}$ - $^{20}\text{Ne}$ ,  $^{22}\text{Ne}$ - $^{22}\text{Ne}$ ). The coincidence line is a good measure for the extent of the TOF region, where Coulomb exploding  $\text{Ne}^+$  ions are found. In order to calculate momenta and coincidences, we use this information to set a temporal condition in the conventional TOF spectrum (figure 7.3(b)).

The impact of the temporal condition can be seen in figure 7.3(a). In the XY-plot, the sphere of Coulomb explodes is projected onto the XY-plane and shows up as a circle centered around the jet spot. There are still a lot of counts from residual gas. The main contribution has water, which is ionized along the FEL path. This is because, water ions hit the detector at same time of flights than slow  $\text{Ne}^+$  ions do.

To prevent false coincidences, we additionally set a spatial condition. The om-

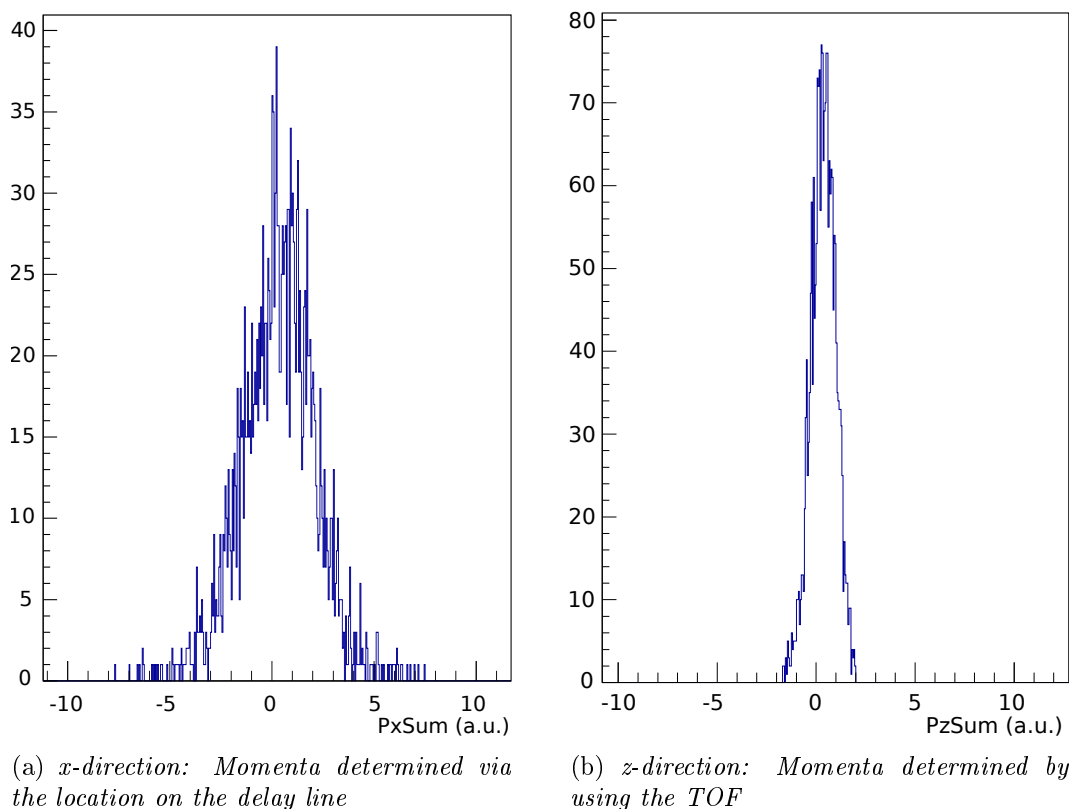


**Figure 7.4:** Momentum sum distributions for coincident  $\text{Ne}^+$  ions

nipresent residual gas, especially along the FEL path and the saturated  $^{20}\text{Ne}^+$  ions are removed. In the end, we are considering just particles lying outside the red sandglass-shaped polygon. Furthermore, one can obtain real coincidences by applying momentum conservation. The sum of both momenta should add up to zero in each direction, if the ions originate from the same, back to back exploding, dimer. The momentum of the emitted ICD electron has not be taken into account. The exerted recoil affects rather the entire molecule than a single  $\text{Ne}^+$  ion, as the separation starts with the emission of the electron itself.

The momentum sum distribution width is ruled by the measurements precision. Aside from that, the distribution widths are different for *z*- and *xy*-direction. The momentum  $p_z$  is calculated via the time of flight, while  $p_x$  and  $p_y$  are calculated via the spatial information of the delay line, lacking in resolution. Two exemplary momentum sums are displayed in figure 7.4.

## 7.2 Kinetic Energy Release

A more detailed view on the process is given in figure 7.5, where the calculated potential energy curves are plotted (Ref. [41]). The lower panel shows the ground state of the neutral  $\text{Ne}_2$ . The equilibrium inter-atomic nuclear distance is  $3.1 \text{ \AA}$ . In the middle panel one can see the outer valence (OV) ionic states, exhibiting a  $2p$  vacancy. Shortly after this first ionization, the  $\text{Ne}^+(2p)^{-1}\text{Ne}$  ion finds itself still at the equilibrium distance, where the OV states are practically degenerate.

The absorption of the second photon is plotted in pink. A negligible delay between the two photons is assumed, so the absorption of the second photon is positioned at the equilibrium distance as well. Another support for this assumption are the flat potential energy curves i.e. low core dynamics. The second photon is absorbed resonantly, as its energy  $\hbar\omega$  matches exactly the energy difference between the  $\text{Ne}^+(2p)^{-1}\text{Ne}$  state and the  $\text{Ne}^+(2s)^{-1}\text{Ne}$  state.

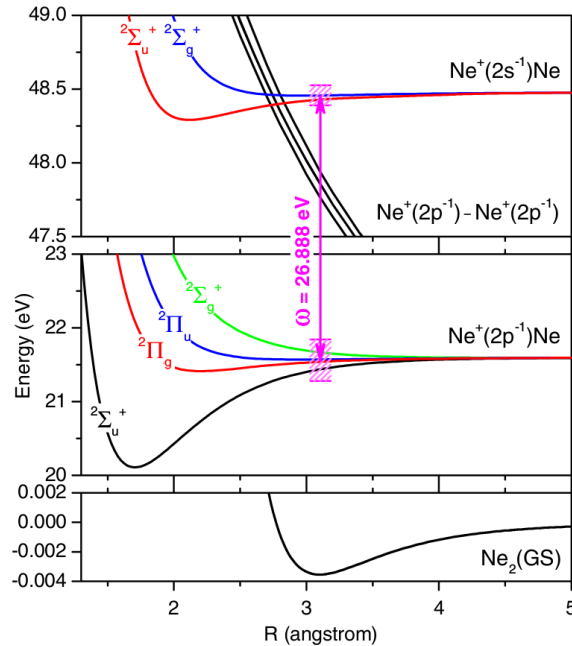


**Figure 7.5:** Potential energy curves for the relevant ionic Ne dimer states [41].

The two states in the top panel are called inner valence (IV) ionic states, due to their  $2s$  vacancy. The energy of these states

is almost identical and both lie within the FELs energy width (hatched pink area). Thus the FEL addresses both, all the OV ionic states and all the IV ionic states. Therefore, dipole selection rules do not constrain the considered transition.

Once the Neon dimer is in the  $\text{Ne}^+(2s)^{-1}\text{Ne}$  state, ICD is a possible de-excitation mechanism. Thereby, an ICD electron is emitted and the dimer transits to the dissociating  $\text{Ne}^+(2p)^{-1}\text{Ne}^+(2p)^{-1}$  state. The ICD electron obtains exactly the gap energy between the two states. There is no local minimum, so the constituents go to large distances  $R$  to minimize their energy. This process is so powerful that one speaks of a Coulomb explosion. In the limit of a large separation, the two

$\text{Ne}^+(2p)^{-1}$  ions can be considered as unbound and free.

The minimum energy they are approaching is their single ionization energy of 21.56 eV [40]. The difference energy of the  $\text{Ne}^+(2s)^{-1}\text{Ne}$  state at the  $\text{Ne}_2$  equilibrium distance (48.48 eV [51]) and the two single Neon OV ions, gives the released energy shared by the ICD electron and the fragments.

$$\begin{aligned} E_{\text{excess}} &= 48.48 \text{ eV} - 2 \cdot 21.56 \text{ eV} \\ &= 5.36 \text{ eV} \end{aligned}$$

In our experiment, no electrons were measured, but Jahnke et al. determined the ICD electron in 2004 to be in the range of 0 eV–2 eV. The peak value is found at about 0.25 eV [52]. Thus, the kinetic energy release (KER) of the  $\text{Ne}^+(2p)^{-1}\text{Ne}^+(2p)^{-1}$  Coulomb explosion peaks at about 5.11 eV. The resulting KER-distribution obtained in our experiment can be seen in figure 7.6 and peaks at 4.7 eV, with maximum energy at 5.4 eV. The good accordance with the anticipated maximum value of 5.11 eV is managed with a deliberately chosen energy scaling parameter.

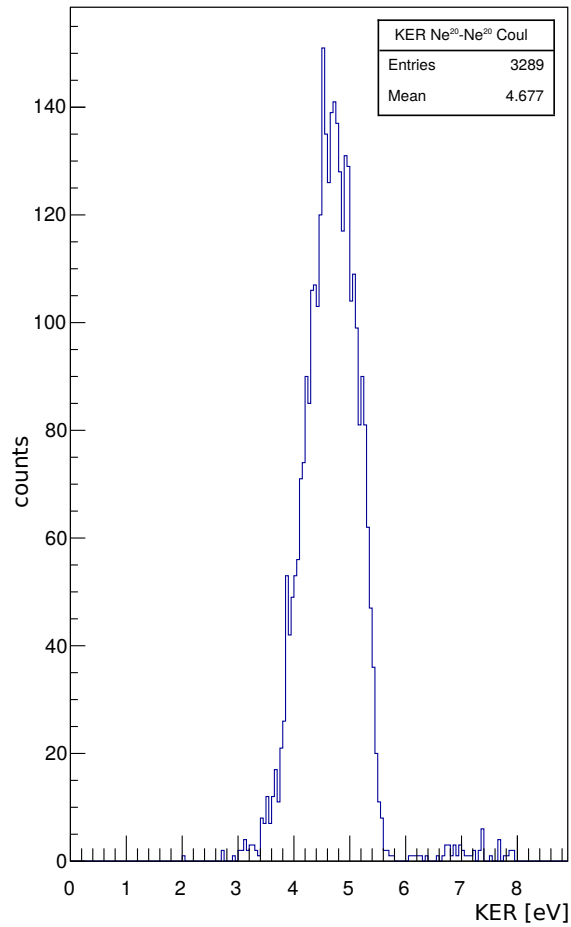


**Figure 7.6:** KER of the exploding  $\text{Ne}^+(2p)^{-1}\text{Ne}^+(2p)^{-1}$  ions.

### 7.3 Scanning the Resonance

According to Dubrouil *et al.* Ref. [53] and Demekhin *et al.* Ref. [41], there is a resonant enhancement of the Coulomb explosion rate, if the photon energy is tuned to the  $\text{Ne}^+(2p^{-1}) \rightarrow \text{Ne}^+(2s^{-1})$  transition at 26.9 eV. Compared to Dubrouil *et al.*, the data taken with a REMI should be clearer and more pronounced. Coincidences are not just made via matching times of flights, but due to the additional spatial resolution, we obtain coincidences based on momentum conservation.

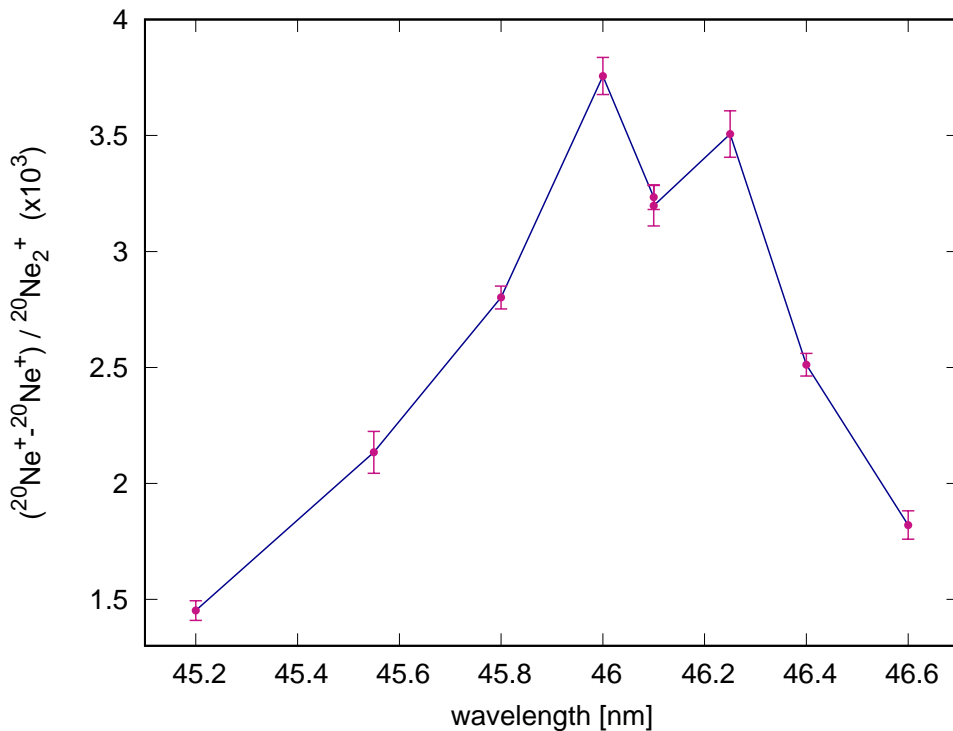


**Figure 7.7:** Coulomb explosion yield, normalized to singly ionized dimers.

Each data point in figure 7.7 shows the averaged yield of several hours measuring time. Intensity fluctuations during a run are not taken into account. The gained absolute number of coulomb explosions, as described in section 7.1, depends still on the the measuring time (or total number of photons) of the considered data set. To account for that, one normalizes with another ion yield. In figure 7.7, the dominant Ne dimer  $^{20/20}\text{Ne}_2^+$  is chosen. The peak is not saturated and has decent statistics.

The error calculation is done using the sampling error  $\propto \frac{1}{\sqrt{n}}$  for the Coulomb explosion and dimer counts. The error of the ratio follows with the usual propagation of uncertainty.

To improve statistics, the dimer  $^{20}\text{Ne} - ^{22}\text{Ne}$  consisting of two different isotopes, can be considered as well. The existence of the dimer isotope is apparent in the PiPiCo figure in 7.2.

The resonant enhancement is centered at around 46.1 nm, exhibiting a hanging tip. The peak width of about 0.3 nm  $\hat{=}$  0.2 eV is attributed to the bandwidth of the FEL. The peak position is in good accordance with the theoretical value of 46.09 nm  $\hat{=}$  26.9 eV. The pronounced effect shows an enhancement of the Coulomb explosion yield by a factor of  $\approx 2.5$ .

The employed multilayer mirror has a photon energy dependent reflectivity, which can be seen in the appendix figure A.4. Within the scanned region, there is no significant change of reflectivity.

The analysis is still in progress, especially the data of the “Online Photoionization Spectrometer” (OPIS) at FLASH. The OPIS can provide single-shot wavelength information, which rules out the shot-to-shot induced bandwidth. Therefore, the resonance curve will be based on much more data points and the bandwidth is governed by a single pulse.

## 7.4 Intensity Dependence

### 7.4.1 Intensity Calibration

The FLASH facility provides a rough intensity signal, which is averaged over many pulses. The intensity of the FEL though, can change from pulse to pulse. For observing an intensity dependence in a reaction, one therefore needs information on a single shot basis.

For this experiment, this is achieved with a voltage signal from the back reflecting mirror. Due to the high pulse energy of the FEL, photoelectrons are emitted from the mirror. The subsequent voltage drop depends on the FEL intensity and is recorded for every pulse. The experimental realization is a voltage measurement between the mirror mount and ground.

The signal however, is not linearly proportional to the actual intensity and needs to be calibrated. One needs to calibrate with a signal, which is linear with intensity. This can be for example, the water ion  $\text{H}_2\text{O}^+$  yield. Water is a residual gas in

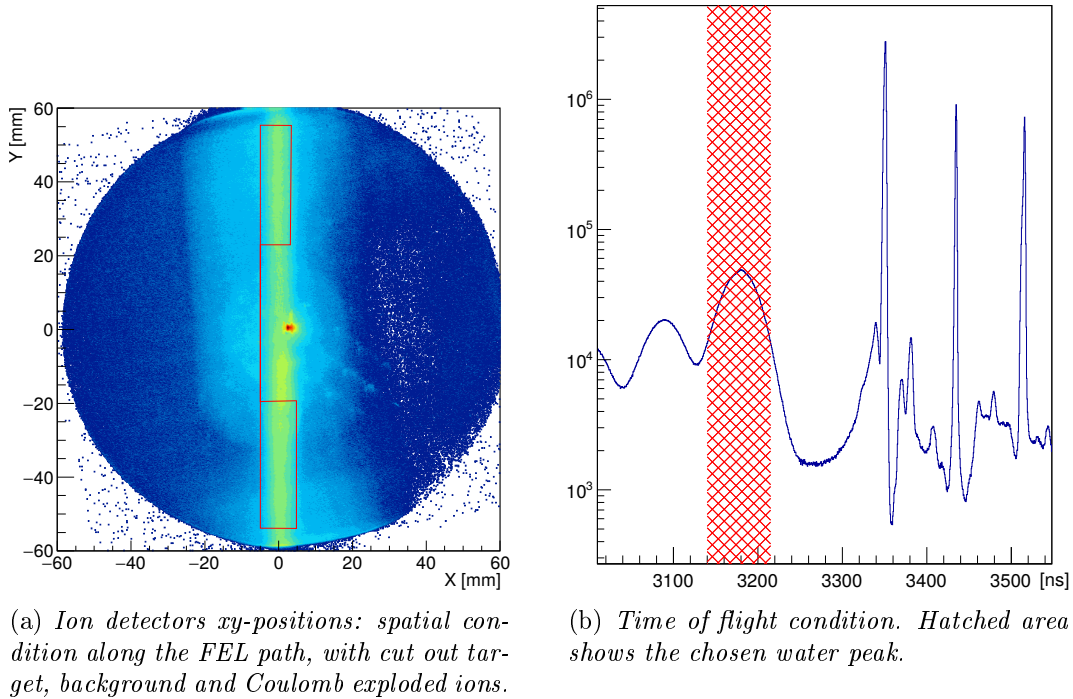
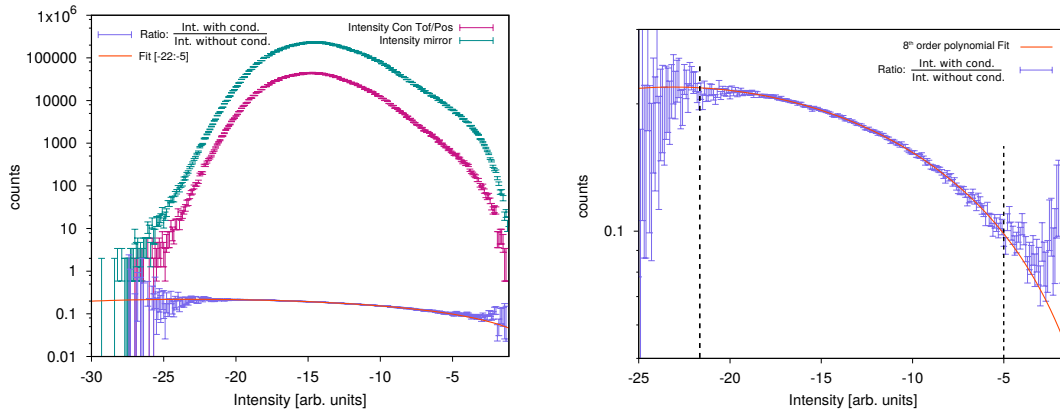


**Figure 7.8:** *Spatial and temporal conditions on residual water molecules, for calibrating the intensity signal.*

the main chamber and is ionized along the entire path of the FEL. Ions hit the MCP at different positions, with a moderate count rate and therefore prevent dead time problems and saturation effects. The spatial condition (figure 7.8(a)) is set on the path of the FEL. Here, the beam is not focused and lower intensities where residual water gets ionized. There is a spared region around the target spot to omit Neon ions from Coulomb explosions. As shown later, these ions obey a different intensity dependence and would spoil the calibration. On top of the spatial condition, a TOF restriction is set to address  $\text{H}_2\text{O}^+$  (figure 7.8).

The two conditions are applied to the intensity-distribution histogram, which gets normalized with the unrestricted intensity distribution. The normalization accounts for the fact, that high and low intensities occur less often than medium intensities. If this normalized distribution (figure 7.9(b)) was already linear, no calibration would be needed. In our case however, we make use of the fact that the water signal is actually linear and take the ordinate as the calibrated intensity axis. Basically, the inverse function is taken for the calibrated axis. The region where the ratio is monotonously increasing with intensity is unambiguous, i.e. can





(a) In green, the unrestricted intensity distribution and in red with the conditions shown in figure 7.8. The ratio of the two data sets is plotted in blue.

(b) A closeup of the calibration curve. The fit is done where the data is monotonous and the statistics sufficient.

**Figure 7.9:** The blue curve shows the normalized water ion yield. Its non-linear intensity dependence is shown in 7.9(b). For linearization, the fit function values are used as the new intensity axis in successive plots.

be used for calibration (from -22 to -5 in figure 7.9(b)). Otherwise two different intensities would lead to the same calibrated intensity and spoil the distribution. Even though the curvature is not too complex, an eighth order polynomial is used for the fit. Lower order functions were proven to be too inaccurate. The fit function values are scaled up to the order of 10, just to deal with more convenient numbers.

For an absolute calibration, cross-sections at the considered wavelengths have to be considered. Moreover, the target density and the interaction volume come into play.

## 7.4.2 Intensity Dependence of ICD

Once the intensity is calibrated on a linear process (section 7.4.1), all other processes can be analyzed for their intensity dependence. Here, the main attention will be given to ICD related Neon ion yields. Figure 7.10 shows the coincident Ne ions plotted against the pulse intensity. Ordinate values are smaller than one, because they are normalized with the total calibrated intensity distribution. The absolute values in the plot report about the gathered statistics. Assuming the cross sections  $\sigma$  to be constant in the considered intensity range, the yields (absorption

probabilities) should scale with integer powers of the intensity (see section 4.2):

$$\text{Yield} \propto w_{ab}^{(n)} \propto |c_b^{(n)}(t)|^2 \propto I^n. \quad (7.4)$$

One typically uses log-log plots to show this dependence. In these plots, the intensity dependence becomes a straight line and the number of involved photons  $n$  is found as the slope.

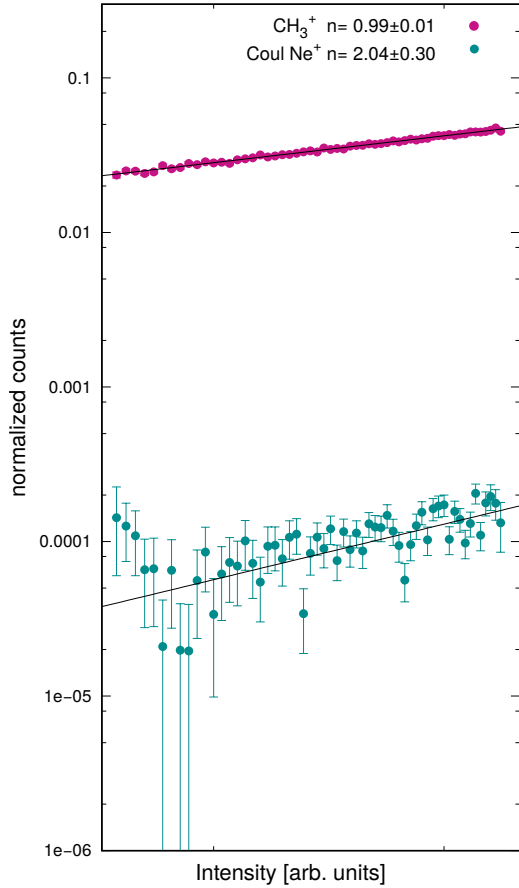


**Figure 7.10:** Ion yield vs intensity in a log-log plot. The slope  $n$  is a fit result. Calibration in red and in green the coincident  $\text{Ne}^+$ .

intensity dependence and cannot be distinguished in this plot. In combination with the resonant enhancement however, depicted in section 7.3, the ICD mechanism can be confirmed.

In order to fit the data, one uses the function:

$$f(x) = a \cdot x^n \quad (7.5)$$

$$\log f(x) = n \log x + \log a \quad (7.6)$$

The parameter  $a$  contains all constants and the cross section.

The fit on  $\text{CH}_3^+$  ions is used to test if the intensity calibration is correct. It is scaling linearly  $n_{\text{calib}} = 0.99 \pm 0.01$ , as demanded from the procedure and has an ionization energy of 9.8 eV Ref. [54]. Due to good statistics, the error cannot be seen in the plot.

For the process of interest, there is about three orders of magnitude less statistics. In about 7 h data acquisition there were 1184 coincidences detected. Nevertheless, sufficient data was gathered to obtain decent fit results. The slope of  $n_{\text{ICD}} = 2.04 \pm 0.30$  suggests a two photon process. In section 5.2, the two main channels leading to Coulomb explosion were introduced. Both in ICD and the 2p ionization in each atom, involves two photons. Therefore they have the same

## 8 Summary

In the course of this work, experiments on dimers ( $\text{Ne}_2, (\text{H}_2\text{O})_2$ ) at the free-electron laser FLASH, were prepared and analyzed, by using a reaction microscope equipped with a supersonic gas jet. The part on the water cluster source describes the procedure of designing and dimensioning of the source, to fulfill all performance demands. Special attention was given to the optimization of cluster yields, especially on the maximization of dimer yields.

The experiment on resonance-enhanced ICD in Neon dimers was carried out with a reaction microscope. Spatial and time sensitive detectors allowed us to investigate the molecular reactions in detail. The resulting coincidences are based on momentum conservation and fragments originating from the same molecule are matched unambiguously.

### 8.1 Results of the Water Cluster Jet

The cluster source was designed and built from scratch and its long term usability could be shown. Filling and heating procedures were established to ensure a safe and efficient use.

Time of flight spectra of the water gas jet were taken by using an intense infrared laser. Intact, singly ionized water dimers could be produced and quantified. A series of measurements revealed an optimal temperature of  $88^\circ\text{C}$  for pure water, which gave a dimer yield relative to monomers of about 0.2%. Compared to the measurements which employ carrier gases, the  $(\text{H}_2\text{O})_2$  yields for pure water were about an order of magnitude smaller. There are two reasons for this large difference in dimer yields. First, the backing pressure with pure water is built up by the water vapor pressure only. In order to reach sufficient backing pressures for supersonic expansion to set in, the water reservoir has to be heated. However, with respect to the water dimer yield, temperature and pressure are competing quantities. While pressure leads to an increased clustering rate, temperature has

a negative impact in the  $(\text{H}_2\text{O})_2$  yield. The second reason for the low cluster rate in pure water vapor jets, is the missing carrier gas cooling. The effect of a carrier gas was investigated in detail for four different noble gases (Helium, Neon, Argon and Xenon).

For Helium, the measurements covered the largest pressure range (2 bar to 14 bar). This allowed to observe the effect of decreasing cluster rates for large carrier gas pressures. The water dimer yield increases from 2 bar to 10 bar, where the maximum yield of 1.07% relative to the water monomer is found. This is explained by the increased Helium abundance, and the following increased cooling rate. For large pressures ( $> 14$  bar) however, the dimer yield decreases, as it is less probable for water molecules to collide and form clusters.

With Neon, a maximum dimer yield of 1.9% at 8 bar backing pressure was achieved. Unfortunately the maximum dimer yield, like in the Helium measurement, could not be found. Pumping rates are limiting the backing pressure. Furthermore, the effect of temperature was analyzed. Increasing the temperature from 44°C to 70°C leads to a dimer yield decrease of 30% at 8 bar backing pressure and 42% at 4 bar backing pressure.

Additionally the formation of mixed clusters Ne- $\text{H}_2\text{O}$  was found was observed. It is following the same temperature and pressure dependences like the water dimer and has a maximum yield of 1.31% at 8 bar backing pressure.

Using Argon as carrier gas has lead to the largest water dimer yields (5.62% at 6 bar). This is probably due to their similar masses of  $^{38}\text{Ar}$  and  $m((\text{H}_2\text{O})_2) = 40u$  and the enhanced collision energy transfer.

Seeding with Xenon turned out to be most challenging for the tested gases. Due to its low ionization potential, the Xenon signal dominates and easily saturates detectors. Additionally, one has to use low backing pressures (0.3 bar), to keep pumps in operation. Nevertheless, we obtained dimer yields of 4.25%.

## 8.2 Results of the Neon Experiment

The aim of the experiment was to show the resonant enhancement of Interatomic Coulombic Decay. This was shown in  $\text{Ne}_2$ , by employing a two-photon process. The experiment was carried out at DESY with the Free-Electron Laser in Hamburg (FLASH2). The adjustable undulator gaps allowed to tune photon wavelengths. With this feature, we could scan the energy region around the  $\text{Ne}^+(2s)^{-1} \rightarrow \text{Ne}^+(2p)^{-1}$  transition at 26.9 eV (46.1 nm). While the first photon

singly ionizes the dimer, by emitting a 2p electron, the second photon drives the mentioned transition. The 2s inner-valence vacancy is the prerequisite for ICD to take place. The relaxation involves a 2p electron, filling the 2s vacancy within the same atom and the following emission of a 2p electron in the neighboring Neon atom. According to Ref. [41], the relaxation via ICD is enhanced, if the the second photon is absorbed resonantly.

In our experiment, we could clearly show the energy dependence of the ICD rate. Within the scanned photon wavelengths from 45.2 nm–46.6 nm, we found an enhancement of the signal by a factor of about 2.5.

Additionally, the intensity dependence of the considered process was analyzed. For that, a detailed description of the intensity calibration was given. The natural intensity fluctuations of the FEL were recorded shot by shot and used for the analysis. As expected, the ICD rate showed a quadratic intensity dependence, as we are dealing with a two photon process.

### 8.3 Outlook

The designed water cluster source will be used in two experiments, scheduled in October and November 2016 at FLASH2. First, the proton transfer through a hydrogen bond in water dimers will be investigated. A special focus will be put on the time scale of the process. For this, an XUV-XUV pump-probe scheme will be used.

In the second experiment, the newly designed cluster source will provide mixed water-rare-gas clusters (Ne-H<sub>2</sub>O, Xe-H<sub>2</sub>O). The aim of the experiment is, to intentionally switch on and off ICD. The rare gas atom acts as an absorption center in the vicinity of a weakly bound water environment. Once a photon is absorbed, the following de-excitation of the rare gas atom can lead to the emission of an ICD electron in the water molecule.

As already mentioned, the analysis of the Neon dimer measurement is not finished at this point. The coarse information on the photon wavelength will be improved with a precise tool based on photoelectron TOF measurements, provided by FLASH2. The Online Photoionization Spectrometer (OPIS), allows to increase the resolution of the scanned resonance and might bring new insight in the exact shape. Furthermore, the single-shot wavelength information can be used to study all kind of photon energy dependent processes in detail.

# A Appendix

## A.1 Supplement Characteristic Values for Scaling Laws

Element	a (Å)	T <sub>ch</sub> (10 <sup>3</sup> K)	Element	a (Å)	T <sub>ch</sub> (10 <sup>3</sup> K)
Ar	3.39	0.927	Ga	2.70	32.5
Kr	3.52	1.285	In	2.96	28.6
Na	3.40	13.0	Ge	2.83	45.4
K	4.22	10.9	Pb	3.12	23.7
Cs	4.90	9.5	Fe	2.27	48.5
Cu	2.27	40.6	Ni	2.22	40.6
Ag	2.57	34.2	Zn	2.48	15.7
Au	2.59	44.2	Cd	2.78	13.5
Al	2.55	37.5	Hg	2.86	7.77

**Figure A.1:** Values used for gas and metal vapors [22]

## A.2 TOF Spectra

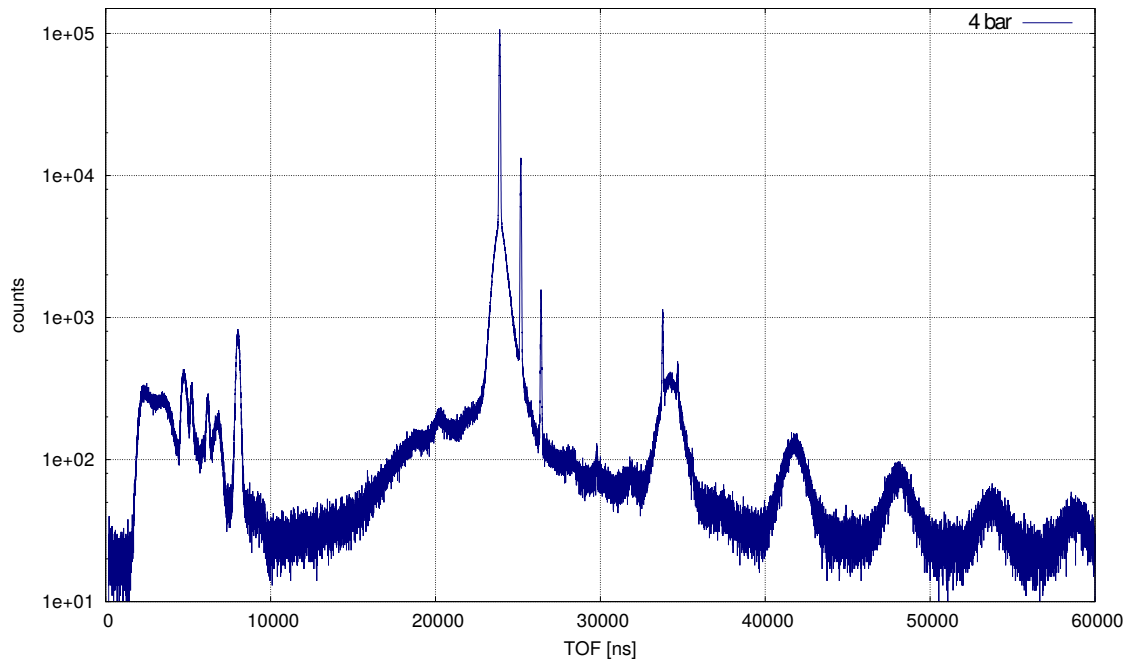


**Figure A.2:** *Neon seeded water jet without heating.*

### A.3 MCP Gain-Curve

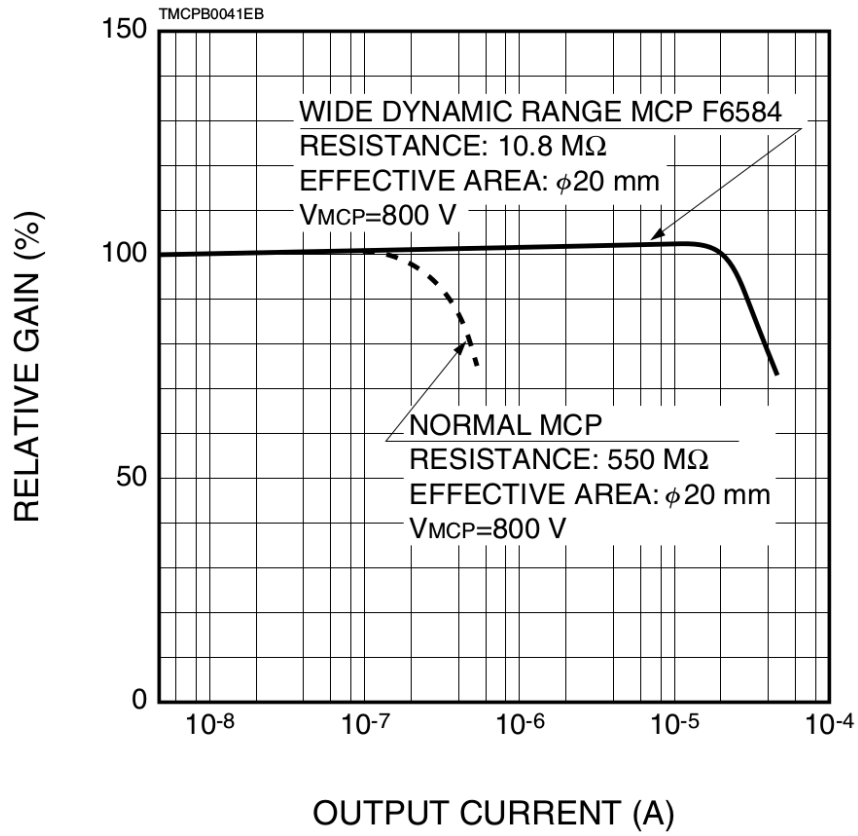


Figure A.3: MCP saturation characteristics (analog mode) [48].



## A.4 Mirror Reflectivity

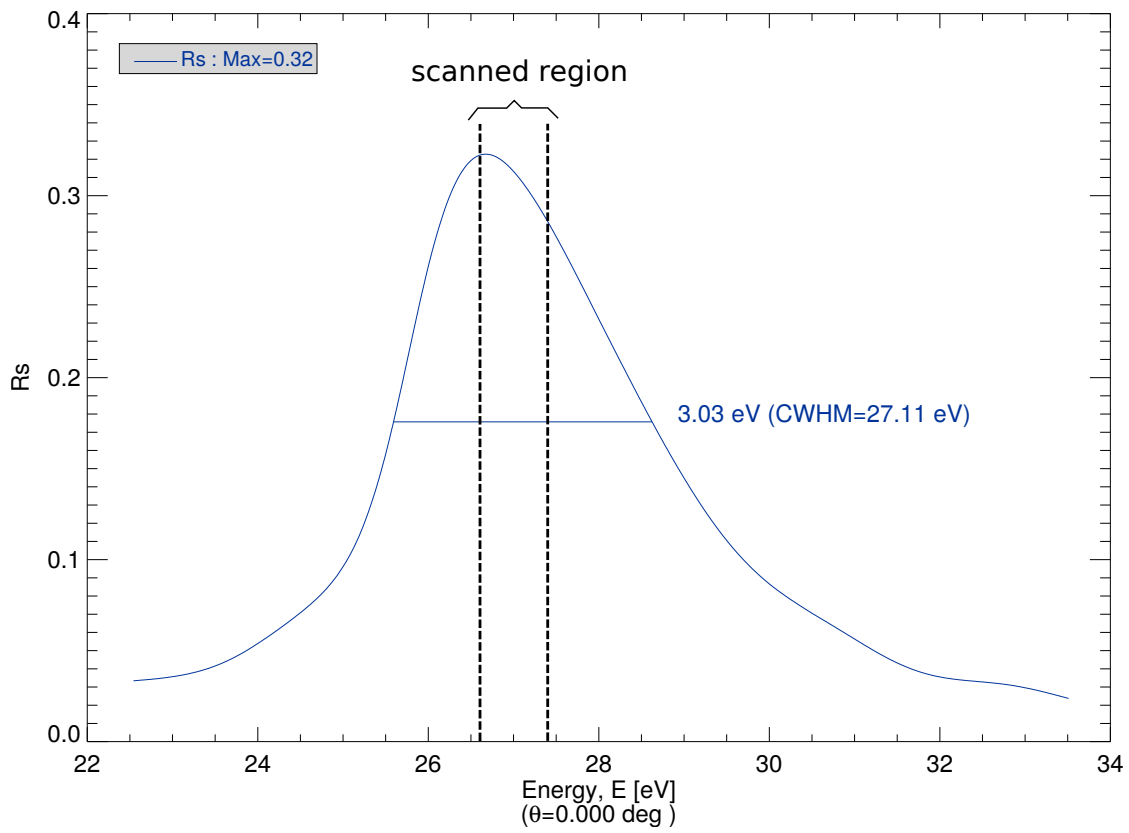
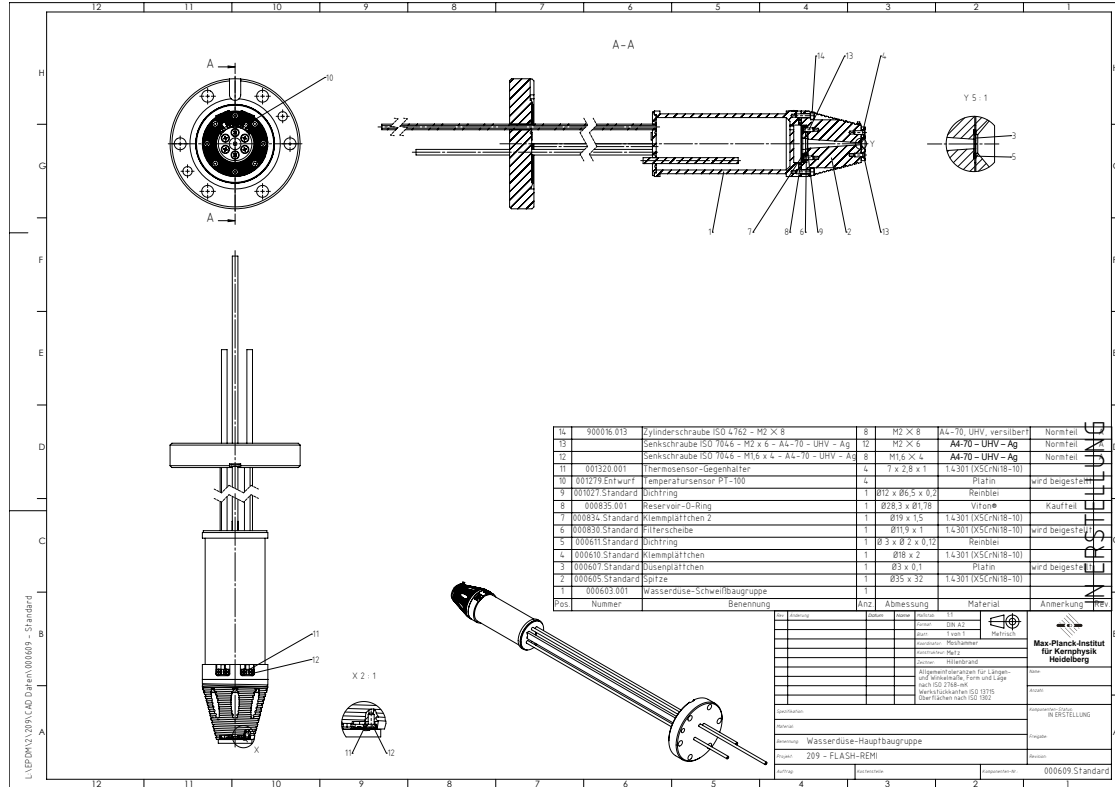
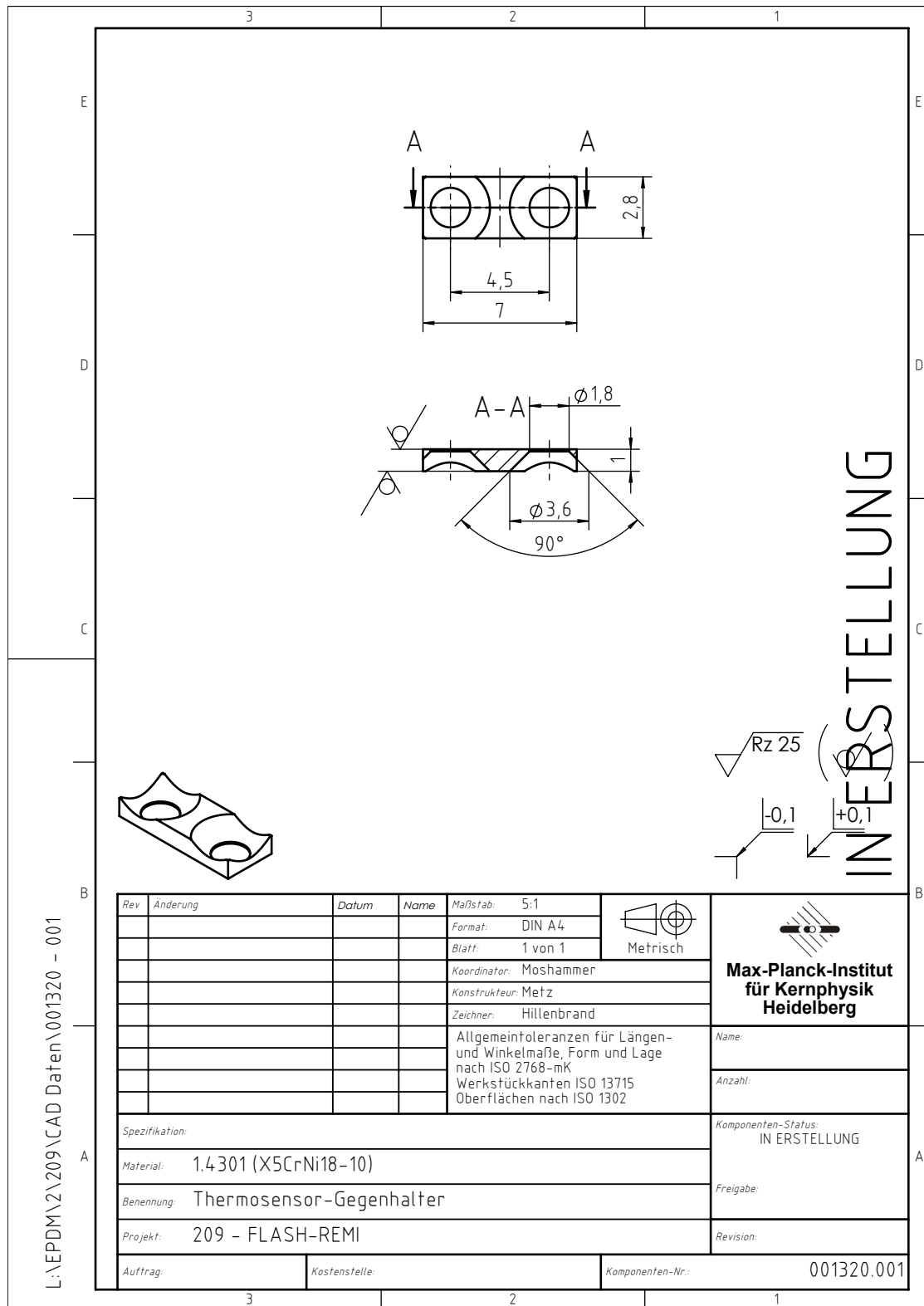


Figure A.4: Photon energy dependence of the mirrors reflectivity

# A.5 Design Drawings of the Water Cluster Jet



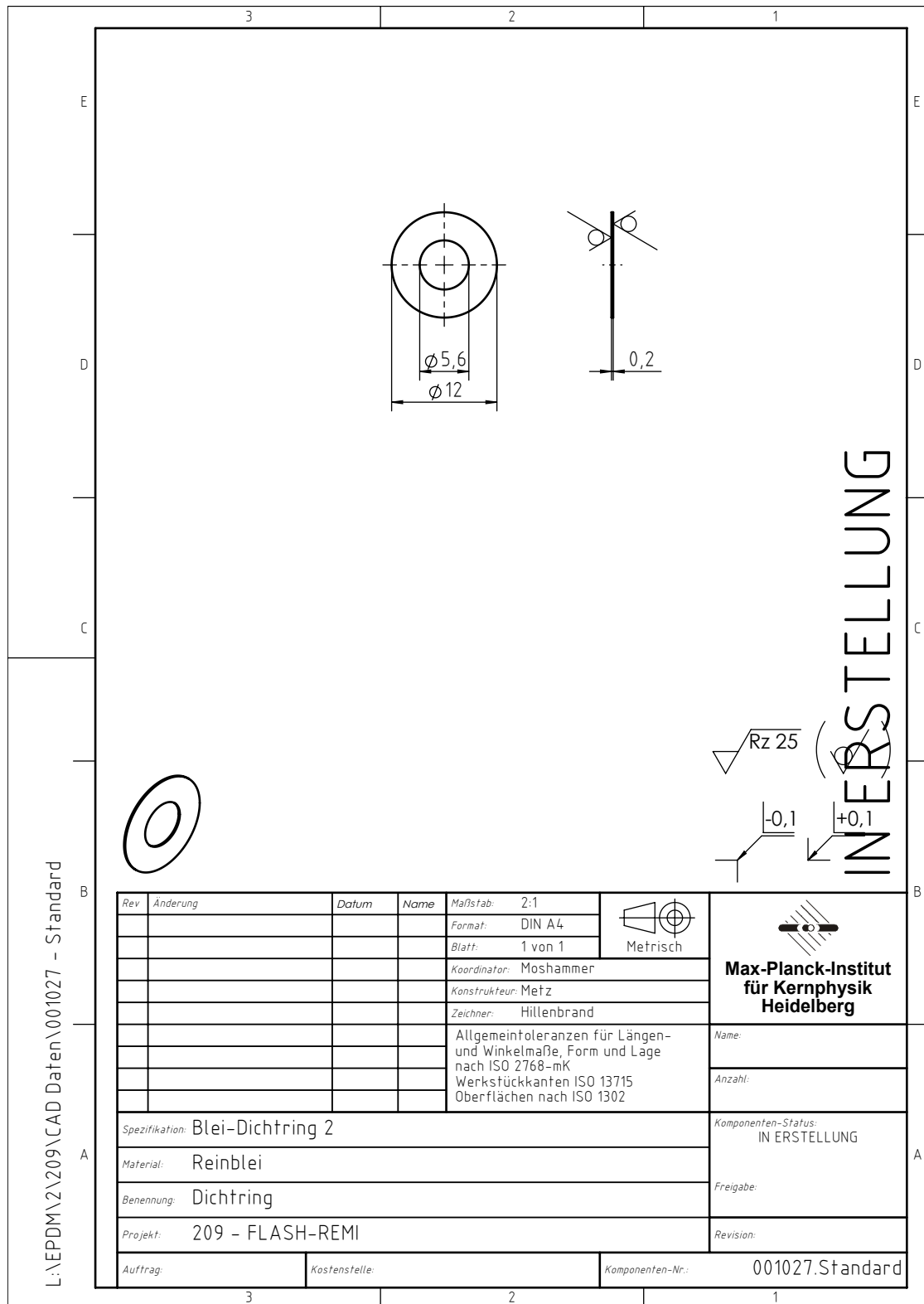
A Appendix



L:\EPDM\2\209\CAD Daten\001320 - 001

Rev	Änderung	Datum	Name	Maßstab:		
				5:1		<b>Max-Planck-Institut für Kernphysik Heidelberg</b>
				Format:	DIN A4	
				Blatt:	1 von 1	
				Koordinator:	Moshammer	
				Konstrukteur:	Metz	
				Zeichner:	Hillenbrand	
				Allgemeintoleranzen für Längen- und Winkelmaße, Form und Lage nach ISO 2768-mK		Name:
				Werkstückkanten ISO 13715		Anzahl:
				Oberflächen nach ISO 1302		Komponenten-Status: IN ERSTELLUNG
	Spezifikation:					Freigabe:
	Material: 1.4301 (X5CrNi18-10)					Revision:
	Benennung: Thermosensor-Gegenhalter					
	Projekt: 209 - FLASH-REMI					
	Auftrag:		Kostenstelle:		Komponenten-Nr.:	001320.001

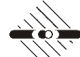
A Appendix

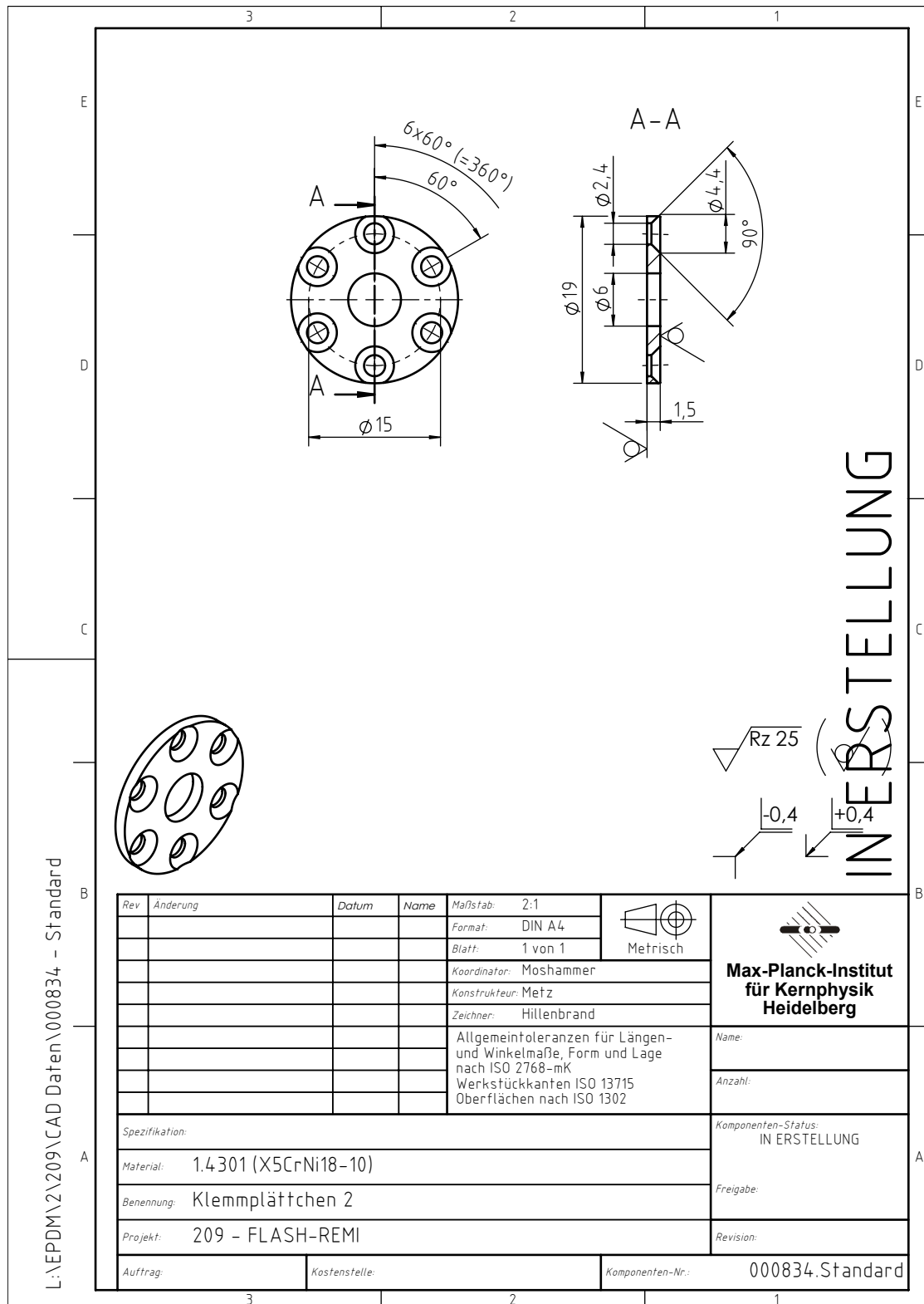


L:\EPDM\2\209\CAD Daten\001027 - Standard

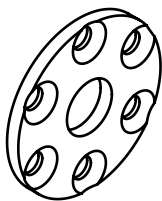


$Rz 25$   
 $-0,1$   $+0,1$   
**INERSTELLUNG**

Rev	Änderung	Datum	Name	Maßstab: 2:1	Metrisch	 <b>Max-Planck-Institut für Kernphysik Heidelberg</b>	
				Format: DIN A4			
				Blatt: 1 von 1		Anzahl:	
				Koordinator: Moshhammer		Komponenten-Status: IN ERSTELLUNG	
				Konstrukteur: Metz			
				Zeichner: Hillenbrand		Freigabe:	
				Allgemeintoleranzen für Längen- und Winkelmaße, Form und Lage nach ISO 2768-mK		Revision:	
				Werkstückkanten ISO 13715			
				Oberflächen nach ISO 1302			
Spezifikation: Blei-Dichtring 2							
Material: Reinblei							
Benennung: Dichtring							
Projekt: 209 - FLASH-REMI							
Auftrag:		Kostenstelle:		Komponenten-Nr.: 001027.Standard			



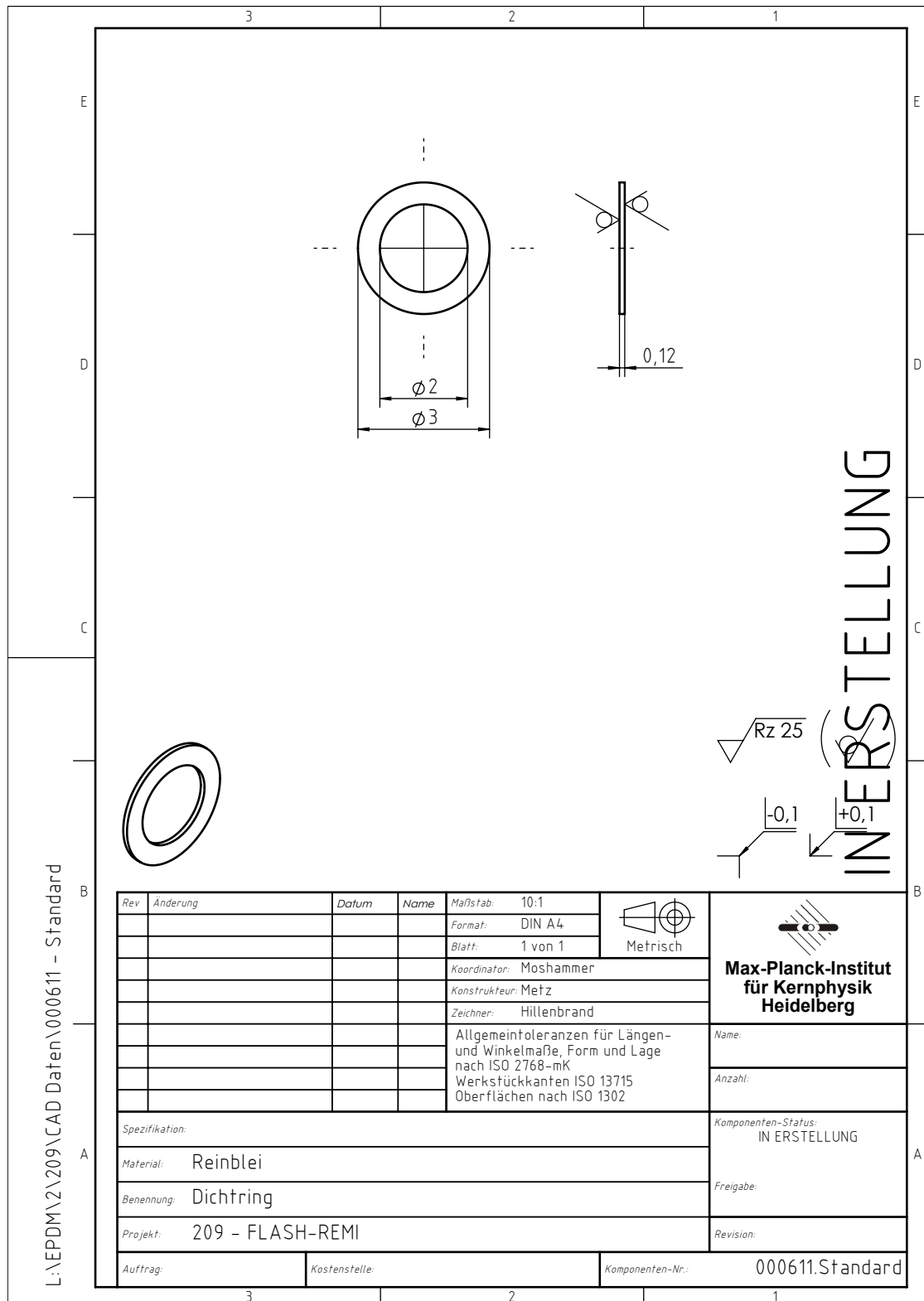
L:\EPDM\2\209\CAD Daten\000834 - Standard

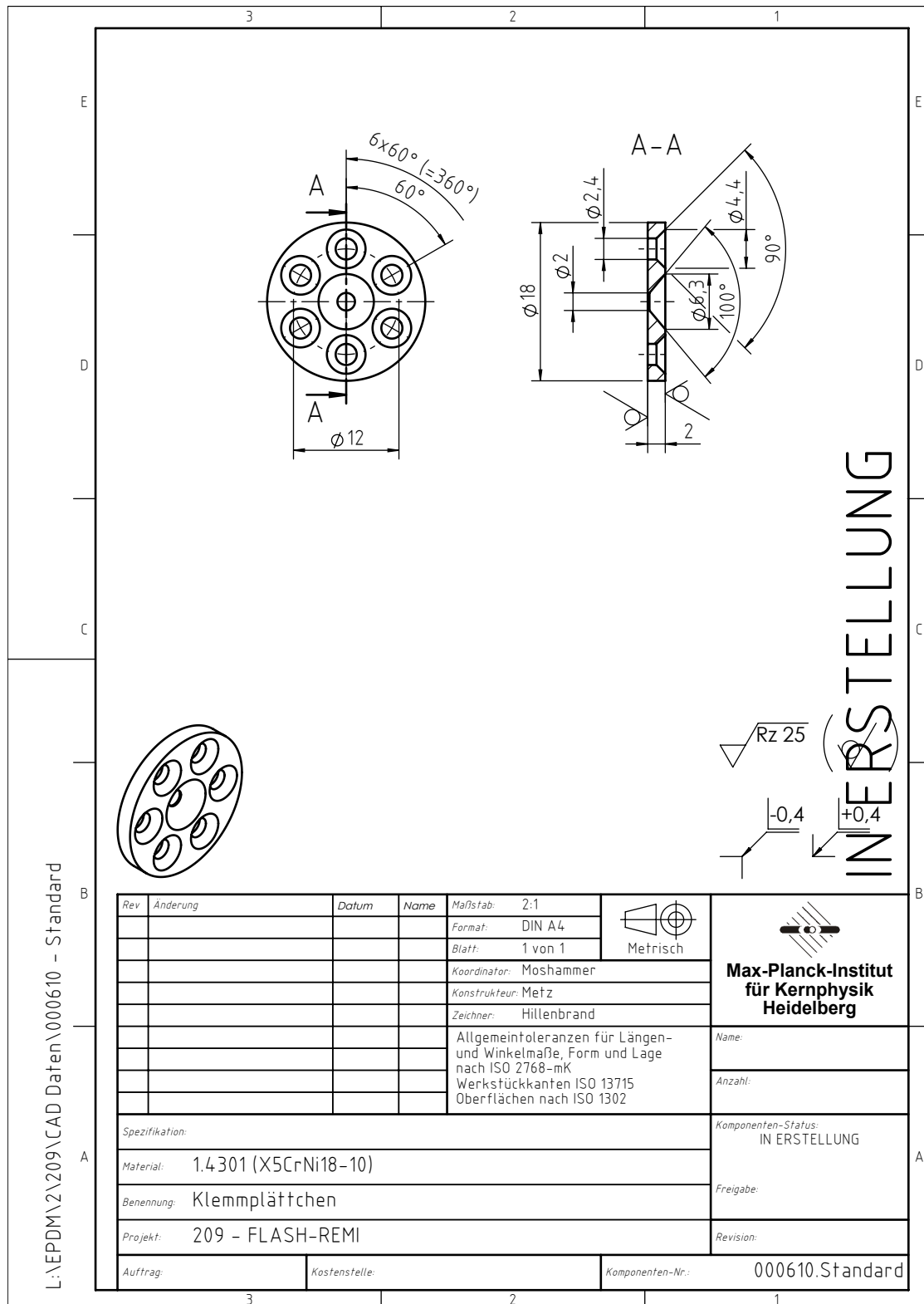


Rev	Änderung	Datum	Name	Maßstab:	2:1
				Format:	DIN A4
				Blatt:	1 von 1
				Koordinator:	Moshhammer
				Konstrukteur:	Metz
				Zeichner:	Hillenbrand
				Allgemeintoleranzen für Längen- und Winkelmaße, Form und Lage nach ISO 2768-mK	
				Werkstückkanten ISO 13715	
				Oberflächen nach ISO 1302	

$Rz 25$   
 $-0,4$   $+0,4$

<b>Max-Planck-Institut für Kernphysik Heidelberg</b>	
Name:	
Anzahl:	
Komponenten-Status:	IN ERSTELLUNG
Freigabe:	
Revision:	
Auftrag:	Kostenstelle:
Komponenten-Nr.: 000834.Standard	

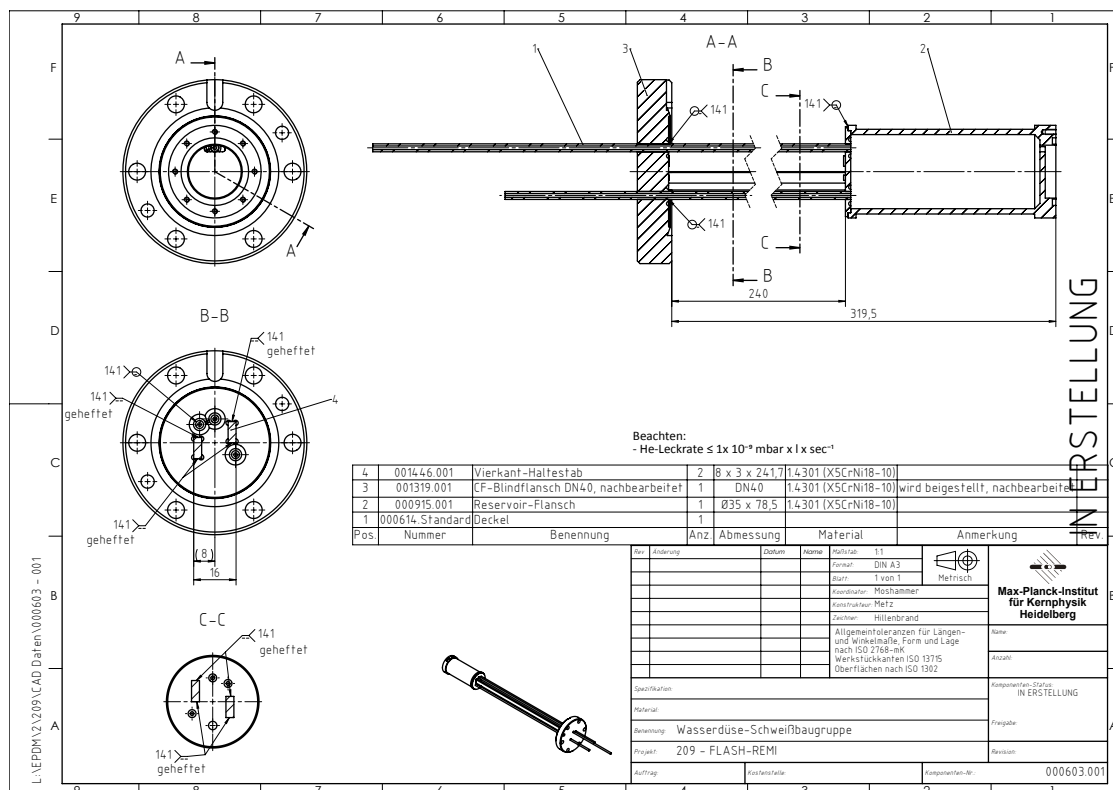
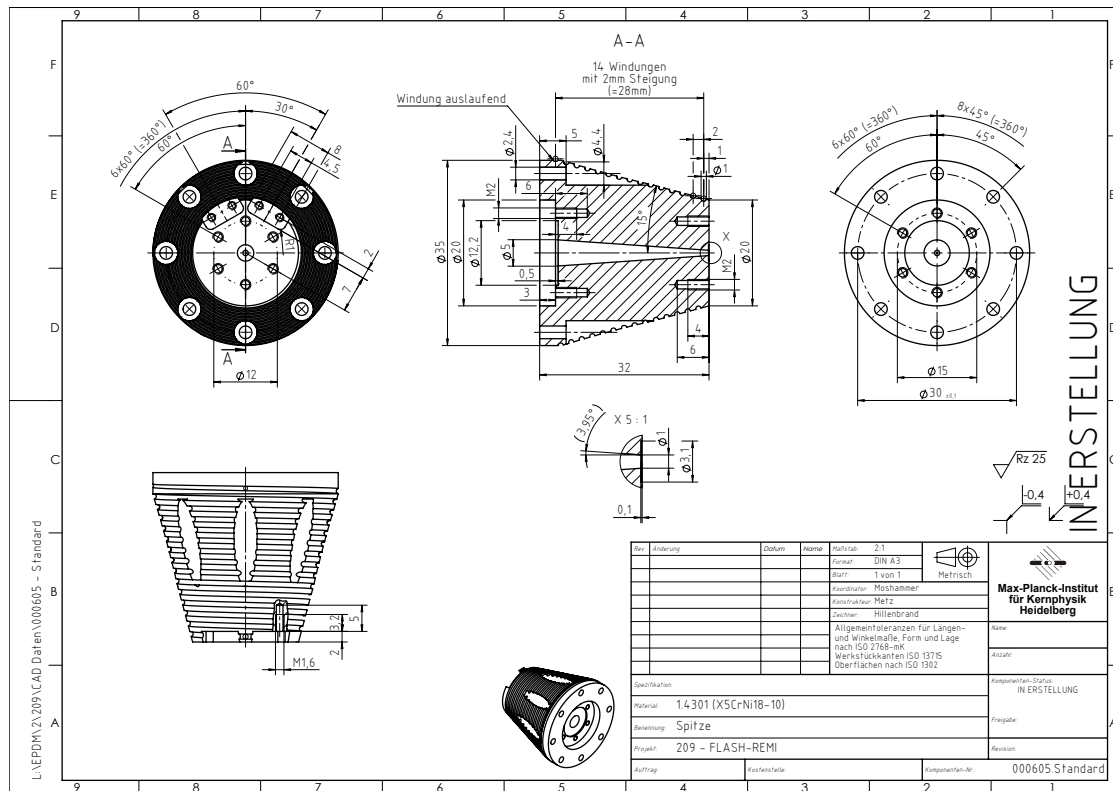




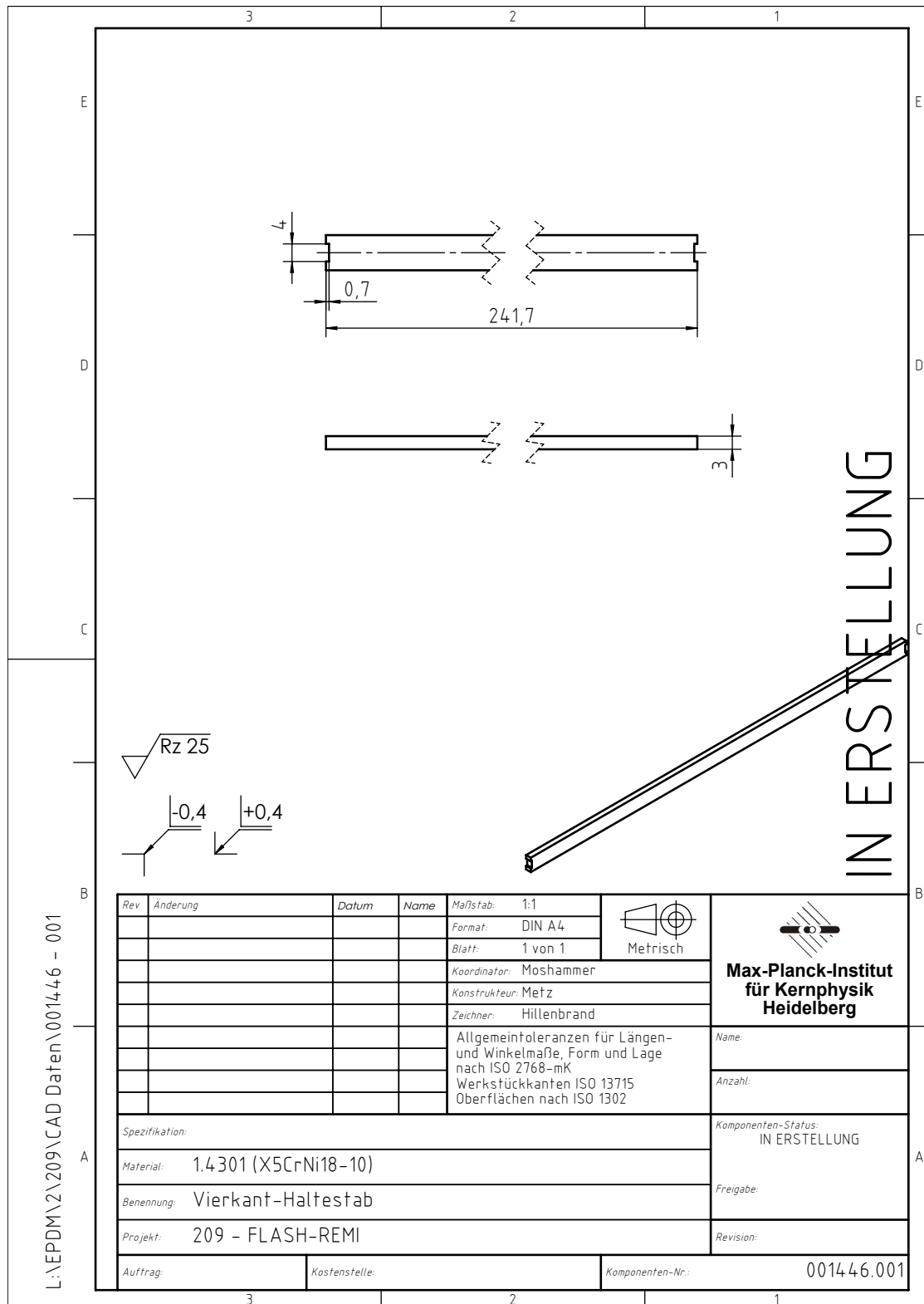
L:\EPDM\2\209\CAD Daten\000610 - Standard

Rev	Änderung	Datum	Name	Maßstab:	2:1	Metrisch		
				Format:	DIN A4			
				Blatt:	1 von 1			
				Koordinator:	Moshhammer			
				Konstrukteur:	Metz			
				Zeichner:	Hillenbrand			
				Allgemeintoleranzen für Längen- und Winkelmaße, Form und Lage nach ISO 2768-mK			Name:	
				Werkstückkanten ISO 13715			Anzahl:	
				Oberflächen nach ISO 1302			Komponenten-Status:	IN ERSTELLUNG
				Spezifikation:			Freigabe:	
				Material: 1.4301 (X5CrNi18-10)			Revision:	
				Benennung: Klemmplättchen				
				Projekt: 209 - FLASH-REMI				
				Auftrag:	Kostenstelle:	Komponenten-Nr.:	000610.Standard	


# A Appendix

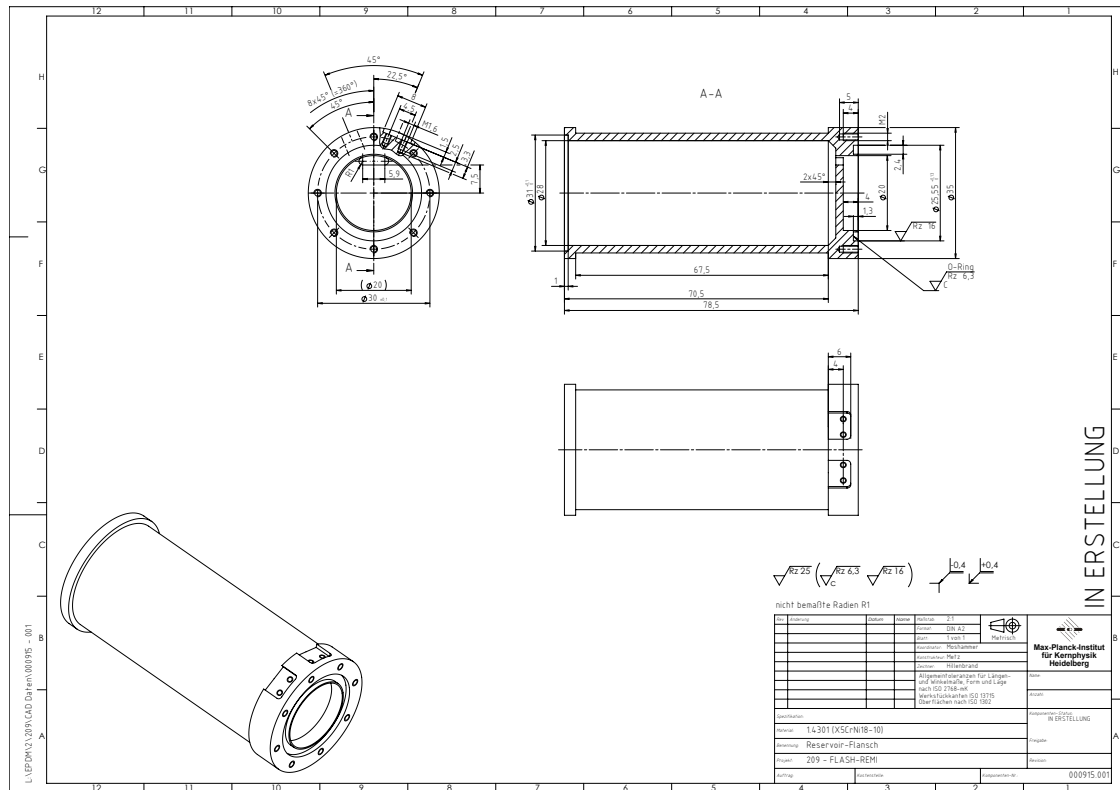
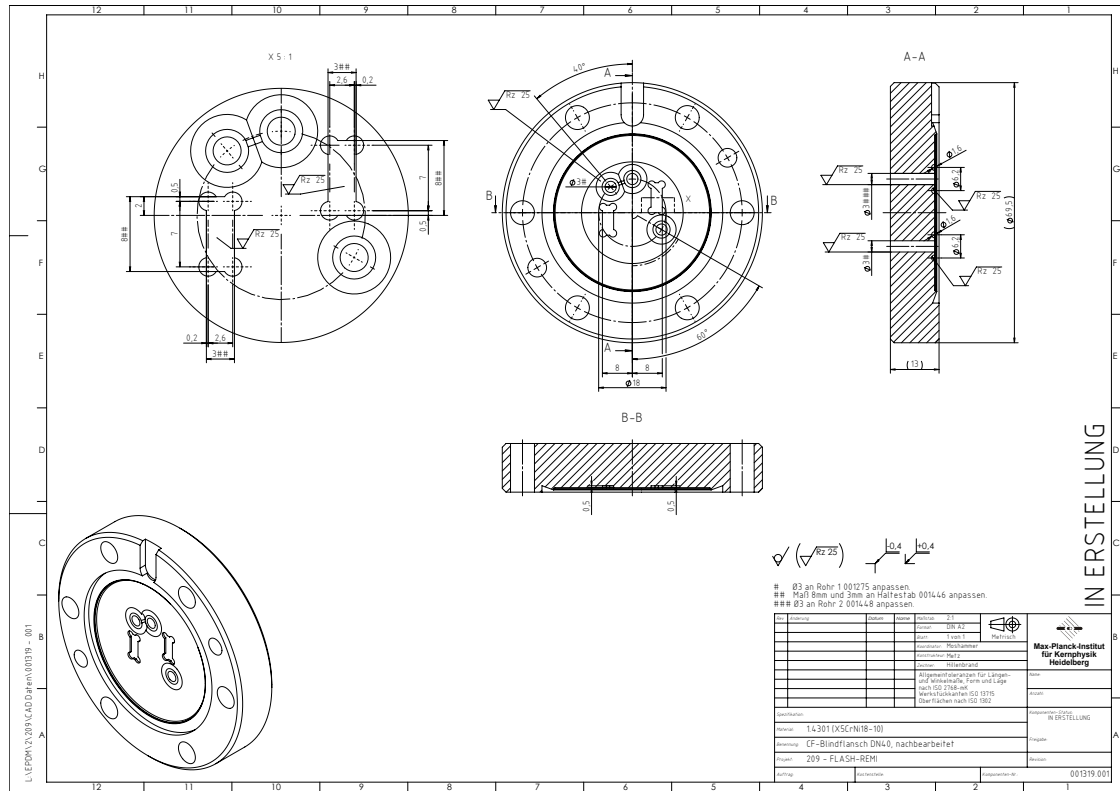




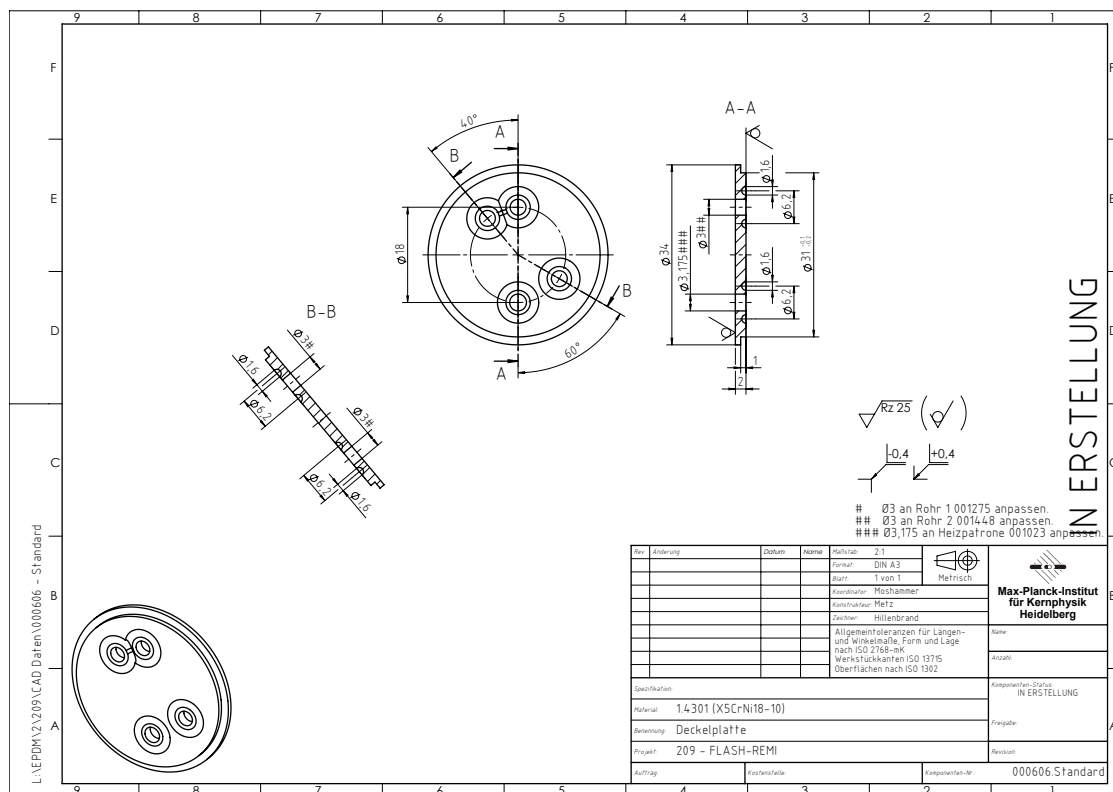
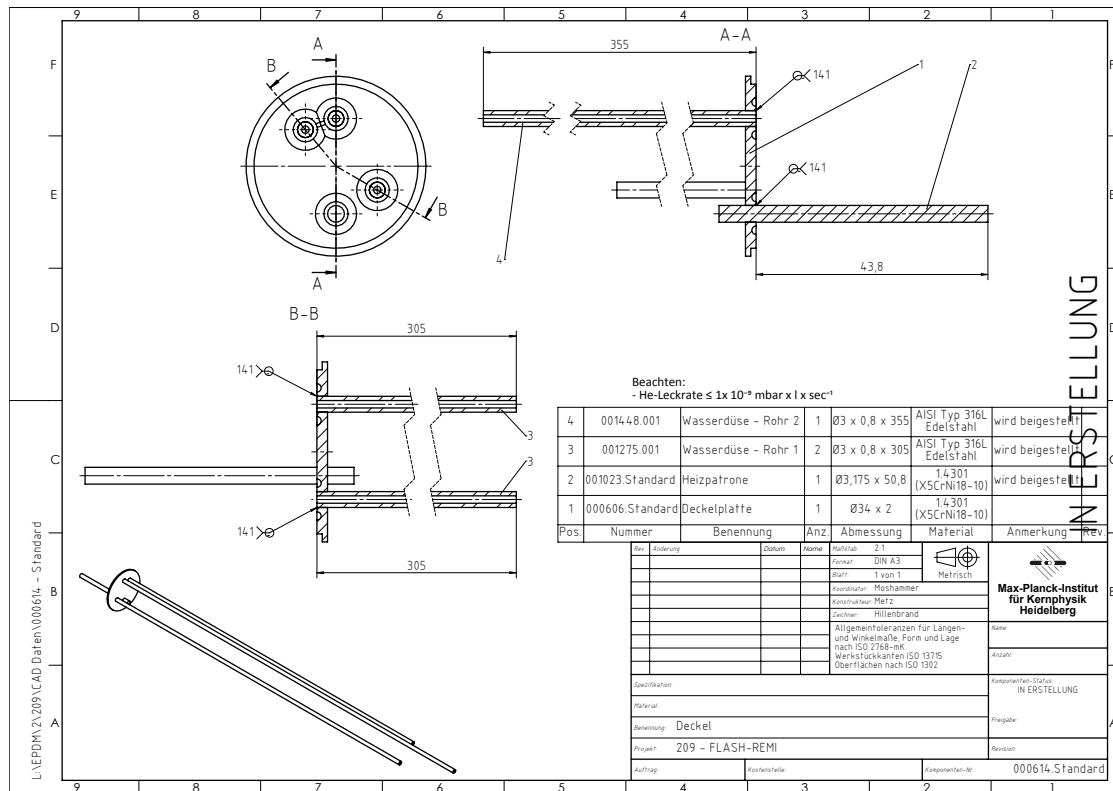


L:\EPDM\2\209\CAD Daten\001446 - 001

Rev	Änderung	Datum	Name	Maßstab:	1:1	Metrisch	 <b>Max-Planck-Institut für Kernphysik Heidelberg</b>
				Format:	DIN A4		
				Blatt:	1 von 1		
				Koordinator:	Moshhammer		
				Konstrukteur:	Metz		
				Zeichner:	Hillenbrand		
				Allgemeintoleranzen für Längen- und Winkelmaße, Form und Lage nach ISO 2768-mK Werkstückkanten ISO 13715 Oberflächen nach ISO 1302			Name:
							Anzahl:
							Komponenten-Status: IN ERSTELLUNG
							Freigabe:
							Revision:
				Auftrag:	Kostenstelle:	Komponenten-Nr.:	001446.001



# A Appendix



# Bibliography

- [1] Richard P. Feynman. There's plenty of room at the bottom. *Engineering and Science*, 23:5 pp22-36, February 1960.
- [2] Ahmed H. Zewail. *Laser Femtochemistry*. American Association for the Advancement of Science, Washington, 1988.
- [3] L. S. Cederbaum, J. Zobeley, and F. Tarantelli. Giant intermolecular decay and fragmentation of clusters. *Phys. Rev. Lett.*, 79:4778–4781, Dec 1997.
- [4] S. Marburger, O. Kugeler, U. Hergenhahn, and T. Möller. Experimental evidence for interatomic coulombic decay in ne clusters. *Phys. Rev. Lett.*, 90:203401, May 2003.
- [5] T. Jahnke, H. Sann, T. Havermeier, K. Kreidi, C. Stuck, M. Meckel, M. Schöffler, N. Neumann, R. Wallauer, S. Voss, A. Czasch, O. Jagutzki, A. Malakzadeh, F. Afaneh, Th. Weber, H. Schmidt-Böcking, and R. Dörner. Ultrafast energy transfer between water molecules. *Nature Physics*, 6(2):139 – 142, 2010.
- [6] V. Averbukh, Ph.V. Demekhin, P. Koloenc, S. Scheit, S.D. Stoychev, A.I. Kuleff, Y.-C. Chiang, K. Gokhberg, S. Kopelke, N. Sisourat, and L.S. Cederbaum. Interatomic electronic decay processes in singly and multiply ionized clusters. *Journal of Electron Spectroscopy and Related Phenomena*, 183(1-3):36–47, 2011. Electron Spectroscopy Kai Siegbahn Memorial Volume.
- [7] Badia Boudaiffa, Pierre Cloutier, Darel Hunting, Michael A. Huels, and Léon Sanche. Resonant formation of DNA strand breaks by low-energy (3 to 20eV) electrons. *Science*, 287(5458):1658–1660, 2000.
- [8] K. Schnorr, G. Schmid, S. Augustin, A. Rudenko, D. Rolles, M. Kübel, C. Jendrzewski, M.F. Kling, B. Erk, R. Boll, C.D. Schröter, T. Pfeifer, and R. Moshhammer. On the dynamics of proton transfer through a hydrogen bond. *FLASH Proposal*, Apr 2015.

- [9] Gavin P. Salam and Matteo Cacciari. Jet clustering in particle physics, via a dynamic nearest neighbour graph implemented with cgal. *LPTHE, Université Pierre et Marie Curie*, March 2006.
- [10] Jürgen Blum and Gerhard Wurm. The growth mechanisms of macroscopic bodies in protoplanetary disks. *Annual Review of Astronomy and Astrophysics*, 46(1):21–56, 2008.
- [11] D. D. Frantz. A computational study of 13-atom Ne-Ar cluster heat capacities. *The of Chemical Physics*, 107, 1992.
- [12] Siegfried Hunklinger. *Festkörperphysik*. Studium. De Gruyter, München, 4. aufl. edition, 2014.
- [13] Alexandre Martins Dias. Neon dimer binding: an ab initio calculation, Dec 2005.
- [14] Hans Pauly. *Atom, molecule, and cluster beams II*. Springer series on atomic, optical, and plasma physics; Physics and astronomy online library. Springer, Berlin ; Heidelberg ; New York [u.a.], 2000.
- [15] O. Echt, K. Sattler, and E. Recknagel. Magic numbers for sphere packings: Experimental verification in free xenon clusters. *Phys. Rev. Lett.*, 47:1121–1124, Oct 1981.
- [16] Manoj K. Harbola. Magic numbers for metallic clusters and the principle of maximum hardness. *Proceedings of the National Academy of Sciences of the United States of America*, 89(3):1036–1039, 1992.
- [17] Ahmed Abdela. *Gas Phase Generation and Deposition of Size-Selected Metal Clusters*. PhD thesis, University of Birmingham, 2013.
- [18] A.L. Mackay. A dense non-crystallographic packing of equal spheres. *Acta Crystallographica*, 15, 916, 1962.
- [19] W.D. Knight, Walt A. De Heer, Winston A. Saunders, K. Clemenger, M.Y. Chou, and Marvin L. Cohen. Alkali metal clusters and the jellium model. *Chemical Physics Letters*, 134:1–5, Feb 1987.
- [20] W. D. Knight, Keith Clemenger, Walt A. de Heer, Winston A. Saunders, M. Y. Chou, and Marvin L. Cohen. Electronic shell structure and abundances of sodium clusters. *Phys. Rev. Lett.*, 52:2141–2143, Jun 1984.

- [21] IUPAC. Iupac golden book. <http://goldbook.iupac.org/S06036.html>, 2016. [Online; accessed 14-October-2016].
- [22] Hans Pauly. *Atom, molecule, and cluster beams I*. Springer series on atomic, optical, and plasma physics ; Physics and astronomy online library. Springer, Berlin ; Heidelberg ; New York [u.a.], 2000.
- [23] Giacinto Scoles, editor. *Atomic and molecular beam methods*. Oxford Univ. Pr., New York, 1988.
- [24] G. Tejeda, B. Maté, J. M. Fernández-Sánchez, and S. Montero. Temperature and density mapping of supersonic jet expansions using linear raman spectroscopy. *Phys. Rev. Lett.*, 76:34–37, Jan 1996.
- [25] O. F. Hagen. Condensation in free jets: Comparison of rare gases and metals. *Zeitschrift für Physik D Atoms, Molecules and Clusters*, 4(3):291–299, 1987.
- [26] C. Bobbert, S. Schütte, C. Steinbach, and U. Buck. Fragmentation and reliable size distributions of large ammonia and water clusters. *The European Physical Journal D - Atomic, Molecular, Optical and Plasma Physics*, 19(2):183–192, 2002.
- [27] NIST. Water: Antoine equation parameters. <http://webbook.nist.gov/cgi/cbook.cgi?ID=C7732185&Mask=4&Type=ANTOINE&Plot=on#ref-2>, 2016. [Online; accessed 24-September-2016].
- [28] Bridgeman and Aldrich. Condensation in free jets: Comparison of rare gases and metals. *J. Heat Transfer*, 86(2):279–286, 1964.
- [29] C.-T. Liu and W.T. Jr. Lindsay. Vapor pressure of D<sub>2</sub>O from 106 to 300 °C. *J. Chem. Eng. Data*, 15(4):510–513, 1970.
- [30] NIST. Basic atomic spectroscopic data. <http://physics.nist.gov/PhysRefData/Handbook/Tables/neontable1.htm>, 2016. [Online; accessed 3-September-2016].
- [31] Melanie Mucke. *Employing electron-electron coincidence techniques to investigate the autoionisation of clusters*. PhD thesis, Technischen Universität Berlin, 2011.

- [32] Lutz Fechner. *High-Resolution Experiments on Strong-Field Ionization of Atoms and Molecules*. Springer Theses, Recognizing Outstanding Ph.D. Research. Springer, Cham, 2016.
- [33] NIST. Water: Ionization energy determinations. <http://webbook.nist.gov/cgi/inchi?ID=C7732185&Mask=20>, 2016. [Online; accessed 21-September-2016].
- [34] Kono H. Lemke and Terry M. Seward. Solvation processes in steam: Ab initio calculations of ion solvent structures and clustering equilibria. *Geochimica et Cosmochimica Acta*, 72(14):3293 – 3310, 2008.
- [35] V. Hermann, Bruce D. Kay, and A.W. Castleman. Evidence for the existence of structures in gas-phase homomolecular clusters of water. *Chemical Physics*, 72(1):185 – 200, 1982.
- [36] K. Hansen, P. U. Andersson, and E. Uggerud. Activation energies for evaporation from protonated and deprotonated water clusters from mass spectra. *The Journal of Chemical Physics*, 131(12), 2009.
- [37] Jyh-Chiang Jiang, Yi-Sheng Wang, Hai-Chou Chang, Sheng H. Lin, Yuan T. Lee, Gereon Niedner-Schatteburg, and Huan-Cheng Chang. Infrared spectra of  $H^+(H_2O)_{5-8}$  clusters, evidence for symmetric proton hydration. *Journal of the American Chemical Society*, 122(7):1398–1410, 2000.
- [38] NIST. Basic atomic spectroscopic data. <http://physics.nist.gov/PhysRefData/Handbook/Tables/argontable1.htm>, 2016. [Online; accessed 8-October-2016].
- [39] Claus-Peter Schulz Ingolf Volker Hertel. *Atome, Moleküle und optische Physik Teil 1*. Springer Spektrum, 2008.
- [40] NIST. Nist atomic spectra database levels data. <http://physics.nist.gov/cgi-bin/ASD/energy1.pl>, 2016. [Online; accessed 27-September-2016].
- [41] Philipp V. Demekhin, Spas D. Stoychev, Alexander I. Kuleff, and Lorenz S. Cederbaum. Exploring interatomic coulombic decay by free electron lasers. *Phys. Rev. Lett.*, 107:273002, Dec 2011.
- [42] K. Schnorr, A. Senftleben, M. Kurka, A. Rudenko, L. Foucar, G. Schmid, A. Broska, T. Pfeifer, K. Meyer, D. Anielski, R. Boll, D. Rolles, M. Kübel,

- M. F. Kling, Y. H. Jiang, S. Mondal, T. Tachibana, K. Ueda, T. Marchenko, M. Simon, G. Brenner, R. Treusch, S. Scheit, V. Averbukh, J. Ullrich, C.-D. Schröter, and R. Moshhammer. Time-resolved measurement of interatomic coulombic decay in  $Ne_2$ . *Phys. Rev. Lett.*, 111:093402, Aug 2013.
- [43] Peter Schmöser, Martin Dohlus, and Jörg Rossbach. *Ultraviolet and soft X-ray free-electron lasers*. Springer tracts in modern physics. Springer, Berlin ; Heidelberg, 2008.
- [44] K. Schnorr. *XUV Pump-Probe Experiments on Electron Rearrangement and Interatomic Coulombic Decay in Diatomic Molecules*. PhD thesis, Ruperto-Carola-University of Heidelberg, 2014.
- [45] Horst Frank. Schemaskizze des Freie-Elektronen-Lasers XFEL. [https://de.wikipedia.org/wiki/Freie-Elektronen-Laser#/media/File:FEL\\_principle.png](https://de.wikipedia.org/wiki/Freie-Elektronen-Laser#/media/File:FEL_principle.png), 2016. [Online; accessed 18-August-2016].
- [46] Joachim Ullrich. *Ten Years of COLTRIMS and Reaction Microscopes*. Max-Planck-Institut für Kernphysik, April 2004.
- [47] C. Benvenuti, J.M. Cazeneuve, P. Chiggiato, F. Cicoira, A. Escudeiro Santana, V. Johaneck, V. Ruzinov, and J. Fraxedas. A novel route to extreme vacua: the non-evaporable getter thin film coatings. *Vacuum*, 53(1):219 – 225, 1999.
- [48] Hamamatsu Photonics K.K. Technical information, Sep 2006.
- [49] T. Pflüger. *Electron Impact Ionization Studies of Small Rare Gas Clusters*. PhD thesis, Ruperto-Carola-University of Heidelberg, 2012.
- [50] Defu Luo. *Untersuchung der Erzeugung von Neon Clustern mit einem Reaktionsmikroskop*. PhD thesis, Ruperto-Carola-University of Heidelberg, 2015.
- [51] N. Moiseyev, R. Santra, J. Zobeley, and L. S. Cederbaum. Fingerprints of the nodal structure of autoionizing vibrational wave functions in clusters: Interatomic coulombic decay in Ne dimer. *The Journal of Chemical Physics*, 114(17):7351–7360, 2001.
- [52] T. Jahnke, A. Czasch, M. S. Schöffler, S. Schössler, A. Knapp, M. Käs, J. Titze, C. Wimmer, K. Kreidi, R. E. Grisenti, A. Staudte, O. Jagutzki,



- U. Hergenhahn, H. Schmidt-Böcking, and R. Dörner. Experimental observation of interatomic coulombic decay in neon dimers. *Phys. Rev. Lett.*, 93:163401, Oct 2004.
- [53] A Dubrouil, M Reduzzi, M Devetta, C Feng, J Hummert, P Finetti, O Plekan, C Grazioli, M Di Fraia, V Lyamayev, A La Forge, R Katzy, F Stienkemeier, Y Ovcharenko, M Coreno, N Berrah, K Motomura, S Mondal, K Ueda, K C Prince, C Callegari, A I Kuleff, Ph V Demekhin, and G Sansone. Two-photon resonant excitation of interatomic coulombic decay in neon dimers. *Journal of Physics B: Atomic, Molecular and Optical Physics*, 48(20):204005, 2015.
- [54] K-C Lau and C Y Ng. *Accurate ab initio predictions of ionization energies of hydrocarbon radicals: CH<sub>2</sub>, CH<sub>3</sub>, C<sub>2</sub>H, C<sub>2</sub>H<sub>3</sub>, C<sub>2</sub>H<sub>5</sub>, C<sub>3</sub>H<sub>3</sub>, and C<sub>3</sub>H<sub>5</sub>*. Amer Inst Physics, United States, 2005.

**Danksagung:**

Es gibt viele Leute denen ich danken möchte für die schöne Zeit als Masterstudent. Bei den Messkampagnen in Hamburg schwimmt Freizeit und Arbeit, was für eine sehr angenehme Atmosphäre sorgt. Im Speziellen möchte ich noch dankend nennen:

- Georg als ersten Ansprechpartner in allen Situationen, der mir mit Pragmatismus und Ausdauer stets zur Seite stand. Außerdem versteht man sich auf schwäbisch doch ein bisschen besser.
  - Kirsten, für ihren Überblick und Durchblick, von dem ich viel lernen konnte. Danke auch für die lustigen Momente in jeder Situationslage.
  - Sven, für den Beistand beim Ringen mit den Computermännlein und seinen unterhaltenden Wortwitz.
  - Robert, für seine Erfahrung und physikalische Intuition die oft weiter geholfen hat, aber auch seine humorvolle und direkte Art.
  - Bernd, der bei allen technischen Problemen eine Lösung parat hält und mit dem man offen über alles reden kann.
  - Hannes, für den mit mir geteilten Erfindungsreichtum und seine entspannte Art. Danke auch für die IT-Kompetenz die mir oft weiter geholfen hat.
  - Claus-Dieter für sein immenses Detailwissen das er gerne teilt, aber auch die anregenden Gespräche jeglicher Art.
  - Florian für seinen gewissenhaften Einsatz und Deutungsreichtum am Experiment.
  - Viktor, der bei der Planung der Düse geholfen hat und die ersten Testmessungen mit mir durchgeführt hat.
- ... und schließlich meinen Eltern, für ihre moralische Unterstützung und auch sonst für alles.

Erklärung:

Ich versichere, dass ich diese Arbeit selbstständig verfasst habe und keine anderen als die angegebenen Quellen und Hilfsmittel benutzt habe.

Heidelberg, den (Datum) .....